HOCHSCHULE
FÜR ANGEWANDTE
WISSENSCHAFTEN-FH
MÜNCHEN

Hochschule München
Fachbereich 06
Physikalische Technik
Studienrichtung Technische Physik

Diplomarbeit

Characterisation of beam profile and frequency stability of an injection-seeded Nd:YAG laser for a Doppler wind lidar system

von

Benjamin Witschas

Durchgeführt am Deutschen Zentrum für Luft- und Raumfahrt DLR im Rahmen eines Projektes der Europäischen Raumfahrtagentur ESA

Referent:	Prof. Dr. Rolf Heilmann, FH München
Korreferent:	Prof. Dr. Johannes Roths, FH München
Betreuer:	Dr. Oliver Reitebuch, DLR Oberpfaffenhofen
Tag der Einreichung:	15. Dezember 2007

München 2007

Contents

Abstract

In the frame of the Atmospheric Dynamics Mission ADM-Aeolus of the European Space Agency (ESA) an airborne demonstrator, called A2D, was developed in a cooperation of DLR and EADS-Astrium. ADM-Aeolus is the first satellite mission worldwide to measure wind from space with a lidar. The objective of the A2D, which is composed of a laser transmitter, a telescope, and a receiver, is to validate the space lidar principle during ground and flight campaigns before launch.

Main objective of this thesis was to characterise the injection-seeded and frequency-tripled Nd:YAG laser transmitter of the A2D concerning its frequency stability, beam divergence, and spectral properties.

New frequency stabilisation methods as ramp-fire and ramp-delay-fire were analysed with the result that the requirements of the seeded laser operation was achieved even within the vibrational environment of an aircraft. During two test flights on the DLR Falcon 20 aircraft, the pulse-to-pulse frequency variation of the laser transmitter was determined to be smaller than 0,6 MHz, and is thus within the requirement of 1,3 MHz.

Another ambitious task was the determination of the laser beam divergence. Two different methods (knife-edge and lens-camera method) were performed in the field and in the laboratory. After optimization of the laser output beam expander, the divergence was measured to be smaller than 100 μrad for the 6-σ-diameter, which is the required value.

An increase in laser energy per pulse from 60 $\frac{mJ}{pulse}$ to 70 $\frac{mJ}{pulse}$ was achieved after characterising the frequency spectrum of the seedlaser and shifting it to the maximum of the gain spectrum of the master oscillator laser. Hence, the laser energy is even higher than the required value of 60 $\frac{mJ}{pulse}$.

Within this thesis the A2D laser transmitter performance was significantly improved and thoroughly characterised. It was shown that the optimized A2D laser meets the requirements for frequency stability, beam divergence and laser pulse energy even during flight conditions on the DLR Falcon 20 aircraft.

Chapter 1

Introduction

Over the past two decades, the tools to observe, understand, and model the Earth System have improved substantially through developments in observational technology. These developments include remote sensing from space, improvements in numerical simulation and high performance computing, and new methods for assimilation of time dependent atmospheric, oceanic, and chemical data in a hierarchical set of dynamically evolving models of the Earth System. This has deepened the understanding of the complex interactions between the various components of the Earth System [ESA 1998]. Despite these developments, there are still major deficiencies in our ability to describe the current state of the Earth System and its components. There is a strong demand for improvements in wind measurements throughout the atmosphere, however, our information on the three-dimensional wind field over the oceans, the tropics, and the southern hemisphere is currently incomplete due to insufficient measurement data. These measurements are crucial for improving numerical weather prediction and understanding atmospheric dynamics and climate processes. Global wind measurements can also improve the prediction of long-term climate changes [Baker et al. 1995].

To fill in the gap in the global observing system, the **European Space Agency** (ESA) has selected the **Atmospheric Dynamics Mission** (ADM) as an Earth Explorer core mission to provide global wind profile observations [ESA 1999]. This is achieved using

a spaceborne direct detection Doppler wind **lidar** (light detection and ranging) instrument, called **ALADIN** (atmospheric laser Doppler instrument), which will be the first European lidar in space and the first worldwide wind lidar in space [Stoffelen et al. 2005]. In order to validate the performance of this lidar system and to obtain a dataset of atmospheric measurements, a prototype for an airborne platform has been developed.

The ALADIN airborne demonstrator, called A2D, was developed to validate the principle of the satellite based Doppler lidar. The A2D, designed to fly on the Falcon 20 research aircraft from DLR (Deutsches Zentrum für Luft- und Raumfahrt), operates as a direct detection Doppler wind lidar at 355 nm wavelength retrieving aerosol and molecular backscatter signals in parallel. A Fabry-Perot interferometer is used to measure the Doppler shift of the spectrally broadened molecular signal while a Fizeau interferometer is used to measure the narrowband aerosol return. The main task of the A2D is to measure the **line of sight** (LOS) component of the wind vector in the atmosphere (0-15 km) with a range resolution of 300 m to 1,2 km. The projection of the line of sight onto the **horizontal line of sight** (HLOS) should be measured with an accuracy of 1 to 2 $\frac{\mathrm{m}}{\mathrm{s}}$, depending on range [Reitebuch et al. 2003, Paffrath 2006].

The key component of the A2D is the laser transmitter, which must comply with constraints for airborne applications such as compactness, ruggedness, and low power consumption. Pulse energy, pulse length, repetition rate, spatial and spectral beam properties are essential laser parameters which determine the instrumental performance of the lidar system.
One challenging goal in the development of the laser transmitter is to achieve a frequency stability which should be in the order of several MHz **root mean square** (rms) at medium output energies of about 60 $\frac{\mathrm{mJ}}{\mathrm{pulse}}$ at 355 nm. This is necessary for accurate wind measurements using the Doppler effect. In order to reach the performance requirements of the A2D, the laser transmitter is designed as a single mode, 60 mJ, 50 Hz pulse repetition rate, diode-pumped, and frequency tripled Nd:YAG laser in a master

oscillator power amplifier configuration [Schröder et al. 2007]. Stable single-frequency operation and tuning is achieved through injection seeding in combination with a newly developed ramp and fire cavity control technique.
A second challenging goal is to create a transmitted laser beam with a divergence angle smaller than the field of view of the receiver. Otherwise backscatter signal from the transmitted laser beam will not be collected from the telescope-receiver configuration.

The main objective of this thesis is to verify the frequency stability and beam divergence, which are crucial laser transmitter paramters influencing the lidar performance. To verify the frequency stability, frequency measurements with a heterodyne unit were performed during two test flights with the Falcon 20 aircraft (chapter 4). Also, the long term frequency stability and the frequency-temperature dependency were verified with heterodyne unit and wavelength meter measurements during ground operation. Additionally, the laser pulse spectral behaviour was characterised with an optical spectrum analyzer (chapter 4).
To determine the accurate divergence angle of the laser beam, field measurements using the knife-edge method and laboratory measurements with a UV-camera in combination with a converging lens were performed (chapter 5).
The following chapters describe the basic principle of a Doppler wind lidar (DWL, chapter 2) and the setup of the ALADIN airborne demonstrator (A2D, chapter 3).

Chapter 2

Doppler wind lidar system

2.1 Lidar principle

LIDAR is the acronym for **light detection and ranging** and is an active remote sensing technology. Due to scattering of laser radiation from the **ultraviolet** (UV) to the **infrared** (IR) spectral region it is possible to investigate atmospheric properties with this method. A lidar consists of three main subsystems: a transmitter, a receiver and a detection unit [Weitkamp 2005]. The schematic setup of a lidar system is shown in figure 2.1.

The laser (light amplification by stimulated emission of radiation) transmitter is the light source which generates light pulses and sends them into the atmosphere. Laser light is an ideal light source for lidar systems because of its large spectral brightness, its small angular divergence from the laser beam, and its ability to create short high power pulses due to the Q-switch technique, developed by McClung and Hellwarth in 1962 [McClung and Hellwarth 1962]. When these transmitted light pulses propagate through the atmosphere, they are affected by atmospheric particles and molecules.

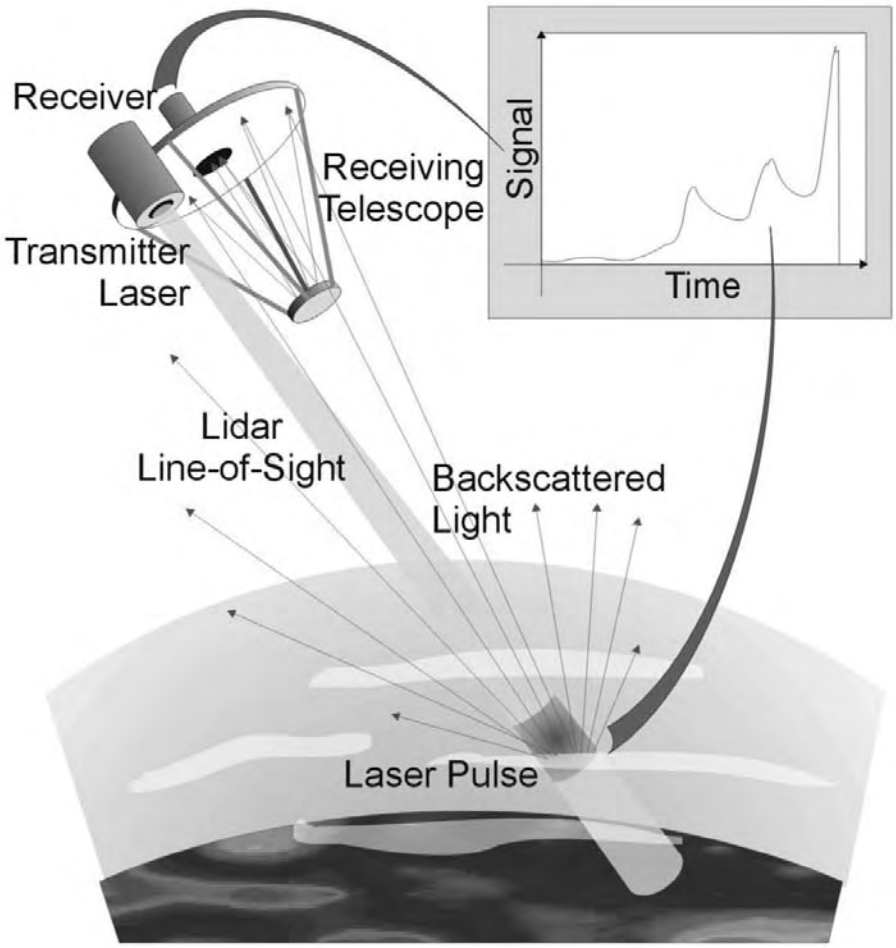

Figure 2.1: Schematic setup of a lidar system [ESA 2005].

The two relevant interactions of laser light with atmospheric particles are Mie scattering from aerosols and cloud particles and Rayleigh scattering from molecules. Rayleigh scattering is dominant at higher altitudes, whereas Mie scattering is relevant in clouds and the atmospheric boundary layer [Chester et. al 1988].

Rayleigh scattering occurs when the wavelength of the propagating light is in the order, or larger than the diameter of the particles. Therefore, typical particles for Rayleigh scattering with ultraviolet light are air molecules like oxygen and nitrogen. The intensity

of Rayleigh scattering depends strongly on the wavelength ($\sim \lambda^{-4}$). In order to obtain a Rayleigh backscatter signal with higher intensity, ultraviolet wavelengths, e.g. 355 nm in case of ALADIN, are used. Because of the absorption spectrum of the stratospere it is not possible to use even lower wavelengths.

Mie scattering occurs when the wavelength of scattered radiation is less than the dimensions of the scattering bodies. This is the case for atmospheric aerosol particles. The intensity of the return signal from aerosol scattering depends on the aerosol concentration, which varies largely horizontly and vertically, and increases in parallel with air pollution, clouds, fog and haze [Measures 1984]. Due to the comparatively lower mass of molecules to aerosols, the velocity distribution of molecules is much broader than that of aerosols, due to the Brownian motion of the particles. Figure 2.2 shows the distribution with relation to the particle speed.

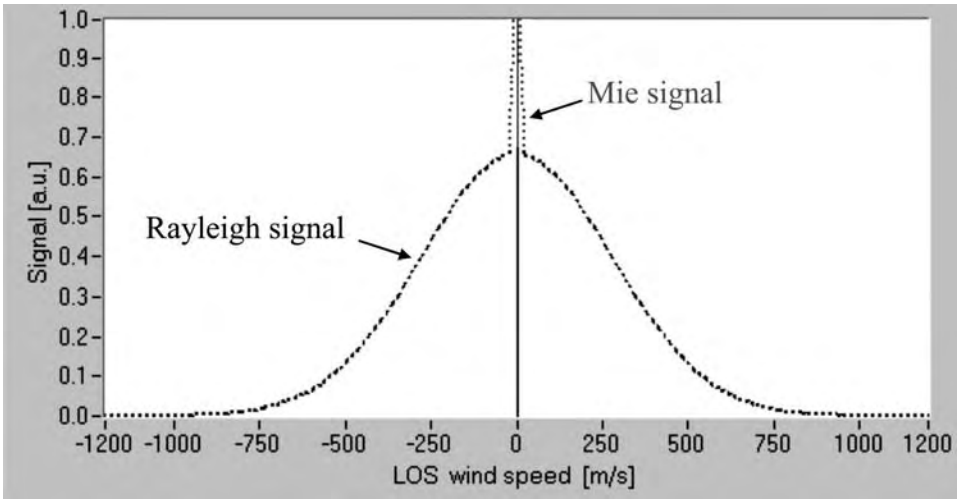

Figure 2.2: Backscatter signals with relation to the aerosol and molecule LOS speed for a wavelength of 355 nm [Paffrath 2006].

The backscattered light is detected by a receiver. Information about atmospheric properties can be obtained with this detected signal. Due to the constant velocity of light

$c = 2,9979 \cdot 10^8 \frac{m}{s}$, a range-resolved measurement is possible. The time t between the transmission of the laser pulse and the arrival of the scattered return signal can be directly related to the range R, at which the scattering occurred, using $R = \frac{c \cdot t}{2}$. A typical backscatter signal for an airborne or spaceborne lidar system which depends on time is shown in figure 2.1. The first two peaks in this figure are caused by clouds or aerosols, and the higher peak due to ground return, which is not be measured for gound based lidar systems.

2.2 Doppler effect

A **Doppler wind lidar** (DWL) uses the **Doppler effect** to determine atmospheric wind speed from space. The Doppler effect is named after the Austrian mathematician and physicist Johann Christian Andreas Doppler (*1803 - †1853) and explains a typical wave phenomenon.

The Doppler effect describes the shift in wavelength as well as in wave frequency caused by the relative motion between observer and wave source. This motion causes an increase in wave frequency, if the source moves towards the observer, and a decrease in wave frequency as they move apart. Sketch 2.3 illustrates the principle of the Doppler effect.

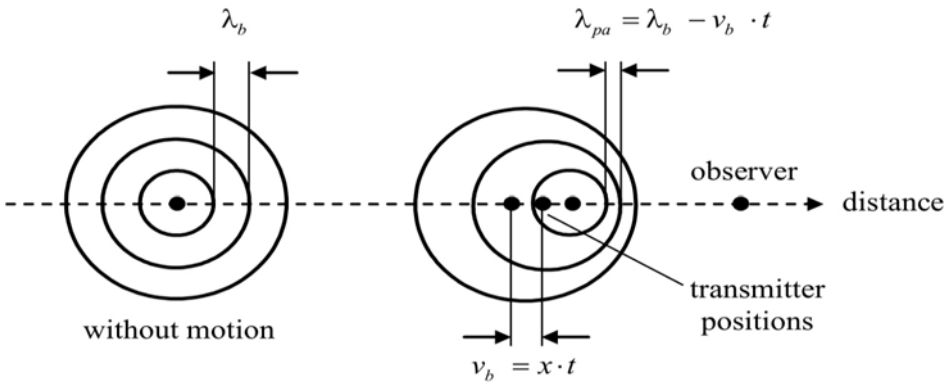

Figure 2.3: Principle of the Doppler effect. λ_b is the wavelength of the wave source. Due to the motion of the wave source with v_b, the observer detects a change in wavelength λ_{pa} and frequency f_{pa}.

During the backscatter process, which is caused by moving particles, the Doppler effect is invoked twice; once when the incident laser light, characterized by the wavelength λ_b and the frequency f_b, impinges on the moving target, and once when light with a frequency f_{pa} is scattered by the moving target particle and received by a stationary detector with the frequency f_{re}.

The frequency f_{pa} which is received from the light source at the particle can be determined with [e.g. Albrecht et. al 2002]

$$f_{pa} = f_b \cdot \left(1 - \frac{v_{pa} \cdot e_b}{c}\right) \tag{2.1}$$

where c is the speed of light in the medium surrounding the particle, v_{pa} is the velocity of the particle, and e_b is the direction unit vector of the light source propagation direction (figure 2.4). The frequency f_{re} which is received from a stationary detector can be calculated with [e.g. Albrecht et. al 2002]

$$f_{re} = f_{pa} \cdot \left(\frac{1}{1 - \frac{v_{pa} \cdot e_{pr}}{c}}\right) \tag{2.2}$$

where e_{pr} is the direction unit vector of the particle to the receiver.
With equation (2.1) in (2.2), the assumption that $|v_{pa}| << c$ and $c = f_b \cdot \lambda_b$, the detected frequency can be approximated with the first two terms of the Taylor expansion at the point $v_{pa} \to 0$. With this approximation the received frequency is described using

$$f_{re} = f_b \cdot \frac{1 - \frac{e_b \cdot v_{pa}}{c}}{1 - \frac{e_{pr} \cdot v_{pa}}{c}} \approx f_b + \frac{v_{pa} \cdot (e_{pr} - e_b)}{\lambda_b} \tag{2.3}$$

Only signals which are backscattered with an angle of 180° are detected when the receiver is placed at the same position as the transmitter ($e_b = -e_{pr}$). Therefore, the **line of sight** (LOS) frequency shift Δf_{re}, in the line of sight pointing direction of the

transmitted laser beam, is determined using

$$\Delta f_{re} = f_{re} - f_b = f_b \cdot \frac{2 \cdot v_{pa}}{c} \tag{2.4}$$

and thus, the LOS wind speed, by measuring the frequency shift between transmitted and received laser pulses. The Doppler shifted signal, caused by Rayleigh and Mie backscattering, is shown in figure 2.5.

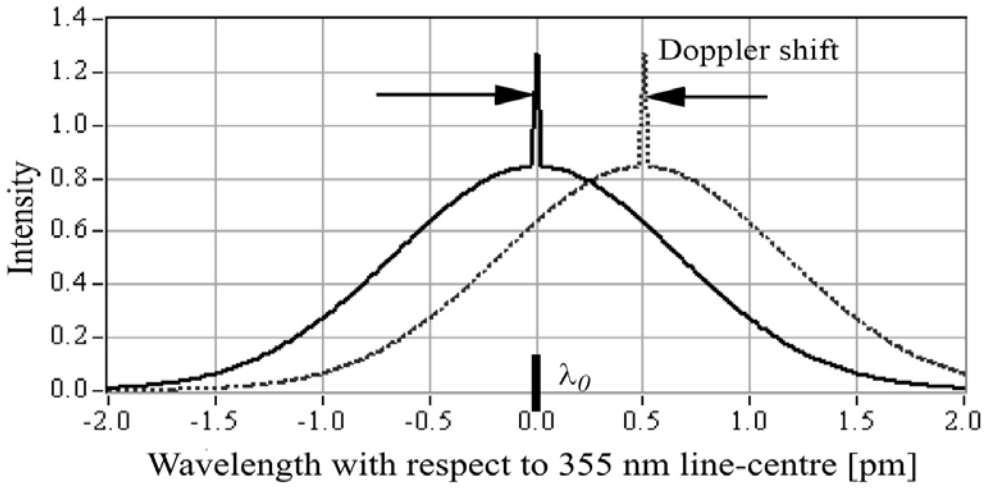

Figure 2.4: Rayleigh backscattering for a wavelength of 355 nm and 0 $\frac{m}{s}$ LOS wind speed (solid line); the Doppler shifted spectrum (dotted line) refers to a wind speed of 210 $\frac{\mathrm{m}}{\mathrm{s}}$ and a wavelength change of 0,5 pm [Paffrath 2006].

Chapter 3

The ALADIN airborne demonstrator

This chapter describes the **ALADIN airborne demonstrator** (A2D) **Doppler wind lidar** (DWL) system including the transmitter, receiver and telescope, which were developed by DLR and **European aeronautic defence and space company** EADS-Astrium Germany and France [Durand et al. 2006, Reitebuch et al. 2004]. A sketch of the A2D system is shown in figure 3.1.
In section 3.1 the setup of the transmitter, including its single components, is described. Section 3.2 introduces the setup of the telescope, and section 3.3 deals with the setup of the receiver, including its principal constituents, the Rayleigh and the Mie receiver.

3.1 Transmitter

The laser transmitter of the A2D is a key component of the DWL system. It consists of a continuous wave **neodymium doped yttrium aluminium garnet** (Nd:YAG) laser used as an injection seeder for a **low power oscillator** (LPO) in order to achieve single frequency operation and tunability. This is followed by two stages of amplification in order to reach the required energy of 60 $\frac{\text{mJ}}{\text{pulse}}$. Harmonic sections convert the original

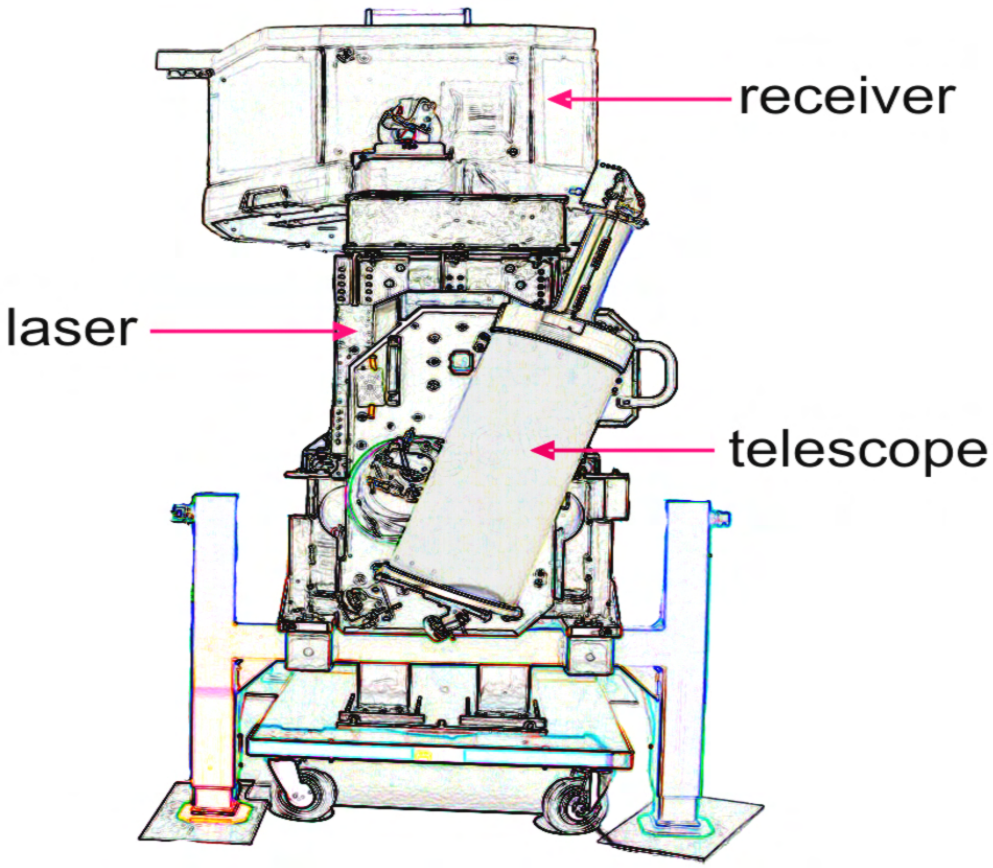

Figure 3.1: Sketch of the A2D Doppler wind lidar system like it is setup in a container.

beam from IR (1064 nm) to green (532 nm), and then UV at 355 nm, the transmitted wavelength into the atmosphere. The laser base plate, where all optical elements are mounted, is made of an iron-nickel alloy called Invar, which guaranties high thermo-mechanical stability. In order to cope with the spatial constraints within the aircraft, the laser head has been constructed in a compact setup with dimensions of 344 mm (width), 780 mm (length), 352 mm (height). A schematic setup of the A2D laser transmitter is shown in figure 3.2 and a photo in figure 3.3.

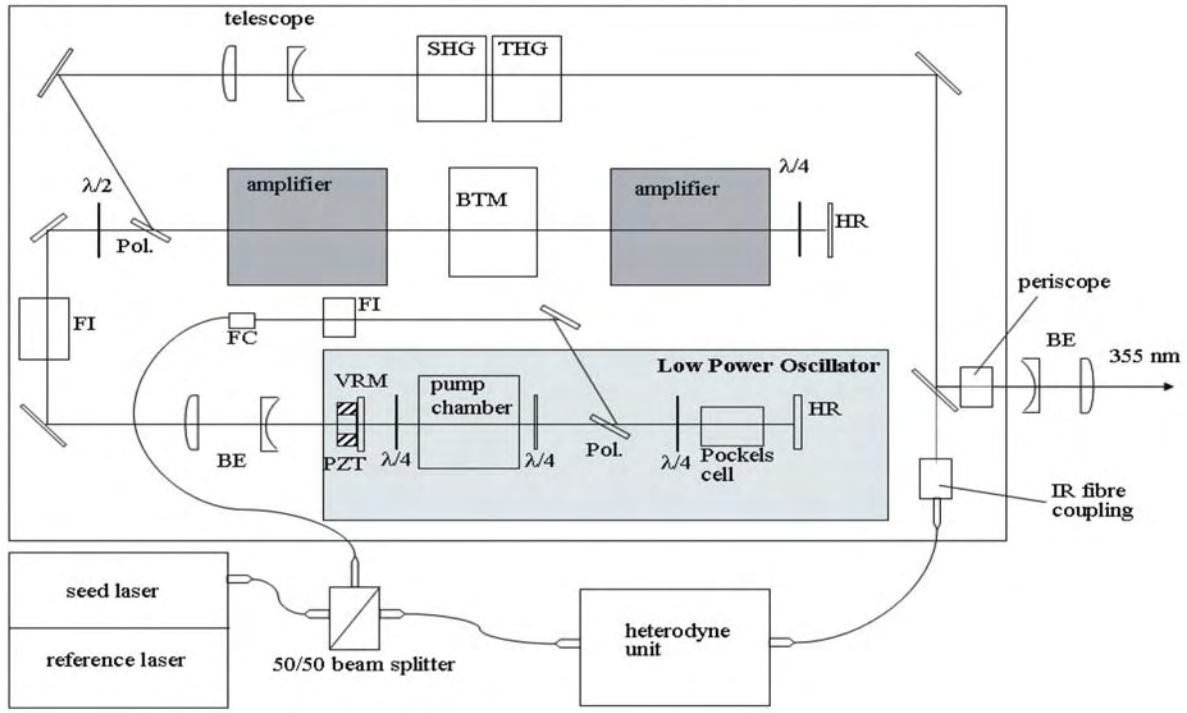

Figure 3.2: Schematic setup of the A2D laser transmitter including its principal constituents [Schröder et al.2007].

3.1.1 Reference laser head

The **reference laser head** (RLH) is a low power, continuous wave, frequency tunable IR laser system (1064 nm) with high frequency stability from Innolight [Innolight 2004]. It consists of two identical laser systems (reference laser and seedlaser) and a frequency stabilization scheme. The reference laser which acts as the frequency reference, operates as a fixed-frequency laser. However, the seedlaser must be tunable in frequency over the range of 15 GHz, for wavelength calibration of the A2D receiver interferometers. The reference laser and seedlaser are both Nd:YAG crystals based on non-planar ring geometry, which enable the combination of high frequency stability and tunability in the same device (see also chapter 4.2.1).

The laser crystal is optically pumped by laser diodes at $\lambda_{pump} = 808$ nm. To hold and tune the seedlaser at a defined frequency offset against the frequency stable reference

laser, a **phased-locked loop** (PLL) controller is used in the RLH. seedlaser frequency tuning is conducted using slow laser crystal temperature variation and fast pump diode current modulation. Hence, the seedlaser is able to tune over 15 GHz single frequency and is mode-hop free.
The seedlaser is coupled into a polarisation maintaining single mode fiber which connects the RLH, via a **fiber connector** (FC), a **Faraday isolator** (FI), and a **polariser** (Pol.), to the LPO. The frequency stability, measured by Innolight is 234 kHz (rms) during 25 min, and the maximum seedlaser power is 90 mW, measured at the fiber output [Innolight 2004].

3.1.2 Low power oscillator

The pump chamber of the linear resonator of the LPO is composed of an Nd:YAG rod which is transversally pumped by 3 standard diode stacks in a 3-fold radial symmetric configuration. Each stack provides a peak power of 350 W for a duration of 175 μs at 100 Hz. The **highly reflective mirror** (HR) is concave with a reflectivity of 99%. A convex Gaussian **variable reflectivity mirror** (VRM) is used as an output coupler to ensure good output beam parameters. With this configuration and a cavity length of about 30 cm, pulse durations of more than 30 ns are obtained. To prevent the effect of spatial hole burning within the laser crystal, two quarter wave plates ($\frac{\lambda}{4}$) are placed in front of and behind the pump chamber to create a circular polarisation within the rod. Thus, any standing-wave patterns can be avoided. For the generation of actively controlled laser pulses, a polarizer, a quarter wave plate, and a pockels cell, acting as a Q-switch, are inserted at the LPO. The Q-switch acts as an electro optical switch which was firstly discussed by [McClung and Hellwarth 1962]. The output coupler of the LPO is mounted on a **piezoelectric translator** (PZT) to allow active cavity length control. A **beam expanding telescope** (BE) positioned behind the LPO magnifies the beam diameter for optimum power amplification. The two **Faraday isolators** (FI) protect the LPO and the seedlaser from destabilizing feedback or damage from back-reflected light [Schröder et al. 2007]. To reach the required frequency stability for wind measurements,

an active frequency control is used in the A2D. The cavity length is controlled by a piezo stack mounted resonator mirror and the ramp and fire technique. Both, the injection seeding method and the ramp and fire technique are discussed in detail in the next chapter 4.2.

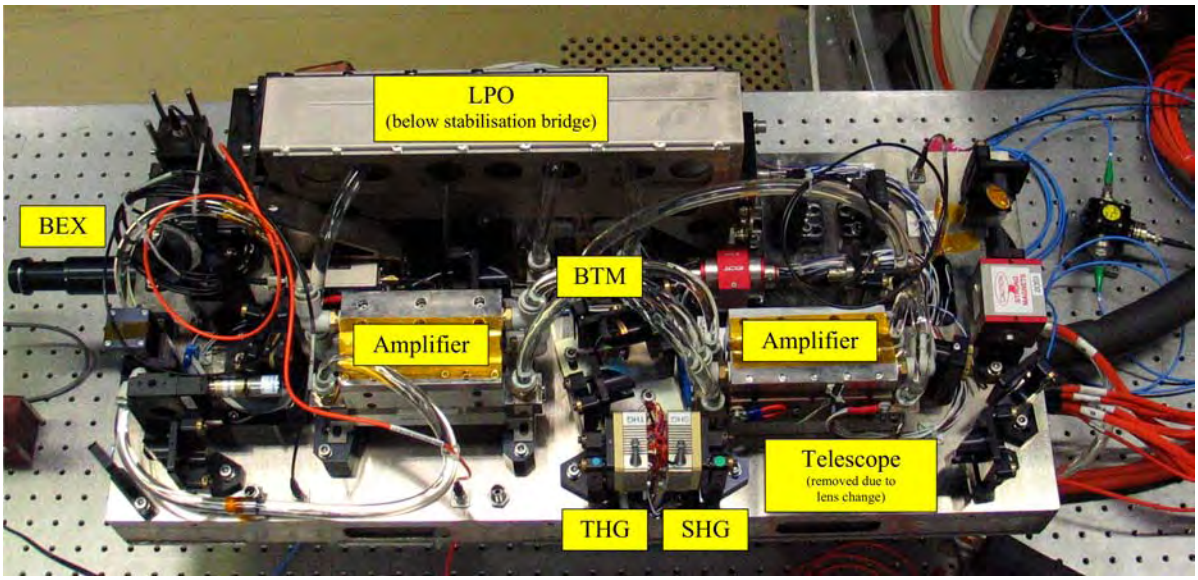

Figure 3.3: Photo of the A2D transmitter. BEX = Beam expander, LPO = Low power oscillator, BTM = Beam turning mirrors, SHG = Second harmonic generation, THG = Third harmonic generation. The dimensions are 344 mm (width), 780 mm (length), and 352 mm (height), with cover (not shown).

3.1.3 Amplifier stages

Slab geometry has been selected as a baseline for the laser crystals of the amplifier stages. This geometry allows effective removal of the strong thermal load deposited in the slab by the pump laser light. Eleven internal reflections lead to an optimum fill factor at given beam diameter and slab dimensions. Each slab is side-pumped by eight standard laser diode stacks ($\frac{1000\ \mathrm{W}}{\mathrm{stack}}$ pumped for 185 μs at 50 Hz, synchronized with the LPO). Between the two amplifier stages, three **beam turning mirrors** (BTM) rotate

the beam spatially by 90° after each pass for compensation of thermally induced astigmatism. After double pass amplification the beam is sufficiently circular to be used by spherical optics. A Galilean telescope in front of the harmonic generators reduces the spot size and adapts the divergence of the pump beam in order to optimize the UV conversion efficiency.

3.1.4 Harmonic generators

The nonlinear optical crystals for **second/third harmonic generation** (SHT/THG) are LBO (LiB_3O_5) crystals (18/16 mm long, 7·7 mm^2 section) used in critical phase-matching orientation and they are temperature stabilized at 35 °C. The high quality anti-reflection coatings at the entrance and exit faces of the SHG crystal (double band coating at 1064 nm and 532 nm) and THG crystal (triple band coating at 1064 nm, 532 nm and 355 nm) minimise the optical losses. Four heaters allow heating the mount symmetrically. A thermistor is attached to the mount as part of the temperature control circuit. An overview of the A2D laser transmitter specifications in shown in table 3.1.

	Spezifications
Transmitter	Nd:YAG, tripled, diode-pumped
Wavelength	355 nm
Repetition rate	50 Hz
Energy/pulse	60 mJ
Frequency stability (IR)	1,3 MHz rms over 7 s
Frequency stability (UV)	4 MHz rms over 7 s
Pulse duration (FWHM)	25 ns (UV)
Linewidth	$<$ 15 MHz

Table 3.1: Specifications of the A2D laser transmitter.

3.2 Telescope

After the laser beam has been emitted and oriented towards the atmosphere, a Cassegrain telescope is used to collect backscattered photons and redirects them into A2D **optical bench assembly** (OBA). A sketch of the Cassegrain telescope is shown in figure 3.4.

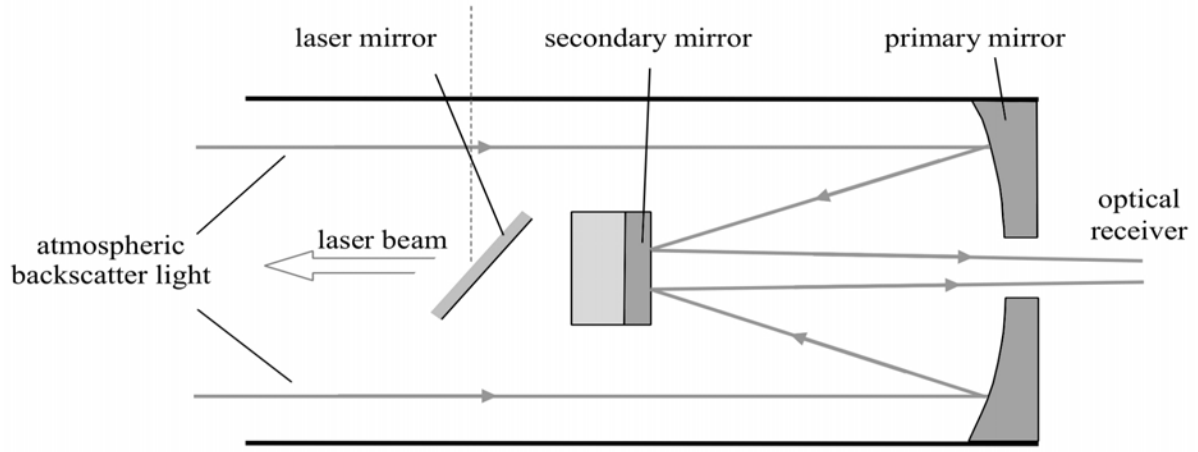

Figure 3.4: Sketch of a Cassegrain telescope.

The A2D telescope is characterized by two convex mirrors and the same optical axis for the transmitted and backscatter light. The primary mirror collects the light and the secondary mirror reflects it through a hole in the primary mirror inside the focal point. The secondary mirror obscures the beam path within the near-field, decreasing the number of photons at the detector.

3.3 Receiver

The key components of the receiver are the Fizeau interferometer for spectral analysing the Mie backscatter signal and the Fabry-Perot interferometer for the Rayleigh backscatter signal. A photo of the Fabry-Perot and the Fizeau interferometer is shown in figure 3.5 and the principle and the main components of the receiver system are shown in figure 3.6.

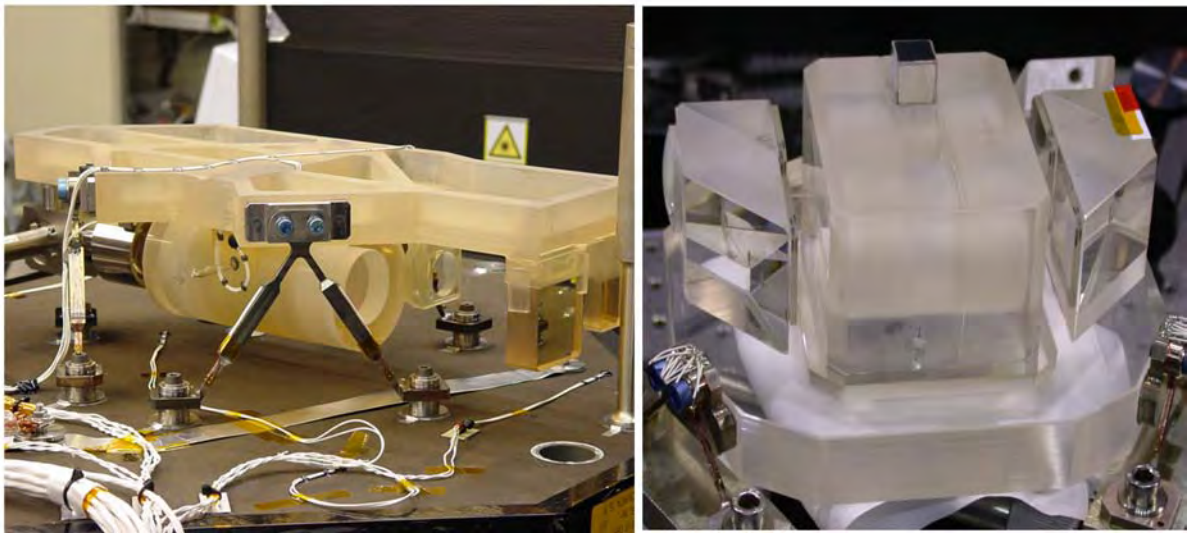

Figure 3.5: Photo of the Fizeau interferometer (left) and Fabry-Perot (right).

To minimise the disturbance due to solar background light, an interference filter is used. Then the signal is reflected off the polarising beam splitter into the Mie receiver which consists of a Fizeau interferometer and an accumulation CCD as detector. The reflected signal from the Mie path is directed towards the Rayleigh detector unit, consists of a Fabry-Perot interferometer. The Mie receiver uses the fringe imaging technique to determine the Doppler shift of the atmospheric backscatter signal, while the Rayleigh receiver uses the double edge technique (more details can be found in Paffrath 2006).

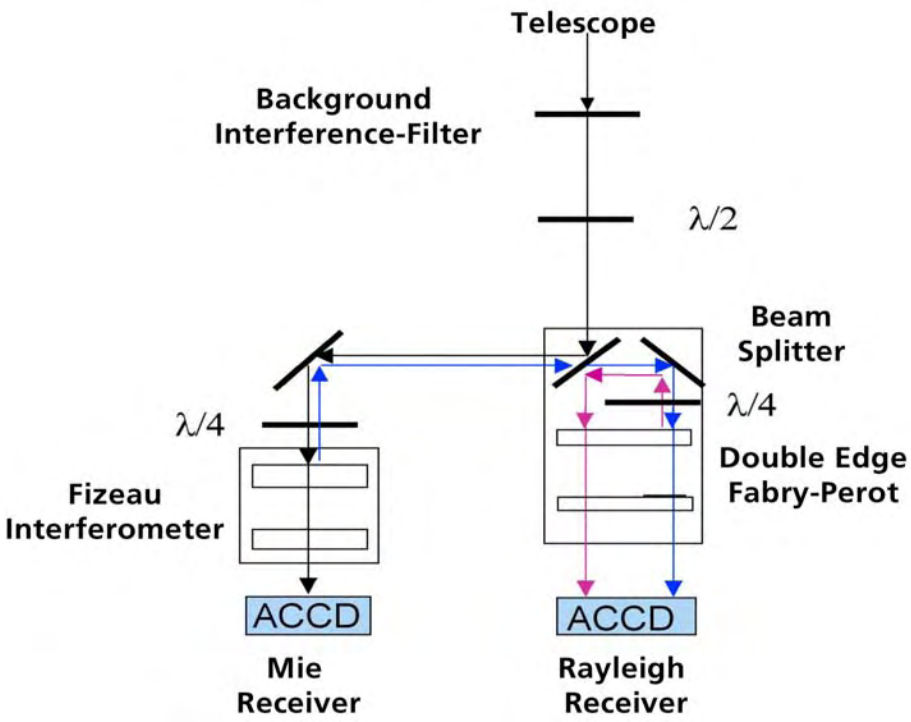

Figure 3.6: Schematic figure of the A2D receiver [Paffrath 2006].

Chapter 4

Laser frequency stability

The required shot-to-shot frequency stability of the A2D laser transmitter during one observation period of 7 s is 4 MHz (rms) at 355 nm. This requirement must be achieved in the vibrational environment of an aircraft. In this thesis, comprehensive frequency characterisation measurements concerning temperature and vibrational dependency were made to verify that the requirement with respect to frequency stability.
This chapter outlines the fundamentals of creating laser radiation (section 4.1) and discusses the theoretical background of the injection seeding frequency stabilisation method (section 4.2). The last three sections in this chapter discuss frequency measurement methods and their results.

4.1 Laser principle

Basically, lasers are devices that generate and amplify light. But unlike conventional light sources, the beam of radiation that lasers emit have remarkable properties of directionality, spectral purity, and intensity. These properties are the reason for the application of laser light in remote sensing techniques like lidar.

To generate laser radiation, only a few essential elements, shown in figure 4.1, are needed. The pumping process is required to excite atoms at the laser material into their higher quantum-mechanical energy level (figure 4.2, top). For laser action more atoms have to be excited into a higher energy level, than are in the lower one. This status is called *population inversion*. The essential condition of population inversion can be obtained, for example, using a flash-lamp, or a diode laser for better efficiency.

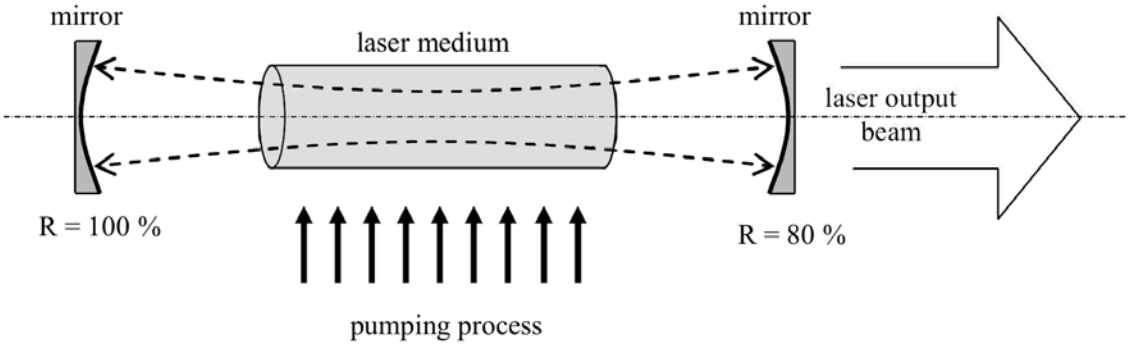

Figure 4.1: The essential elements of a laser device. A laser medium consisting of an appropriate collection of atoms, the pumping process to excite these atoms into higher quantum-mechanical levels, and suitable optical feedback elements to allow a beam of radiation to bounce back and fourth repeatedly through the laser medium [adapted from Siegmann 1986].

After a certain time the excited atoms make a spontaneous transition back to the lower level, emitting radiation with characteristic transition frequencies in the process (figure 4.2, middle). Within a Nd:YAG crystal, this transition produces radiation with a wavelength of about 1064 nm or other wavelengths depending on laser crystal temperature. Incoherent light is produced by spontaneous emission, as the point of time and therefore the phase of the emitted light waves (or photons) are generated by mere chance. To obtain the typical coherent and powerful properties of laser radiation, an optical resonator is needed. In the simplest case, this resonator is built with two high-reflective mirrors (figure 4.1). If the photon, developed from spontaneous emission gets reflected between these mirrors, a process called *stimulated emission* is started (figure 4.2, bottom). Herein, a photon prompts another atom to drop to a lower energy level while

emitting a second photon. This photon has the same properties, in terms of phase and polarisation, as the initial one.

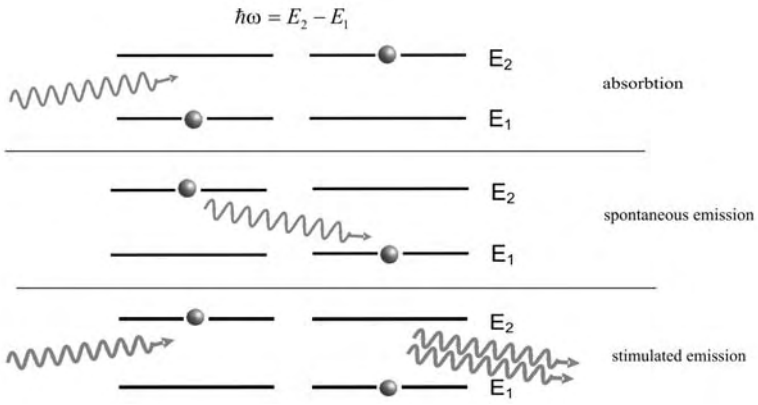

Figure 4.2: Principle of absorption, spontaneous and stimulated emission [Reitebuch and Fix 2006].

The frequency f of a photon is linked with the Planck constant $h = 6,626 \cdot 10^{-34}$ Js to the difference between the quantum energy levels:

$$E_{Ph} = E_2 - E_1 = h \cdot f \tag{4.1}$$

The wavelength λ of the photon is described with:

$$c = \lambda \cdot f \tag{4.2}$$

Due to permanent feedback between the two resonator mirrors, the light inside is amplified as long as population inversion predominates, and the optical length of the resonator $n \cdot L$ (n = index of refraction) is an integer multiple of half of the wavelength to obtain positive interference (resonance condition).

$$n \cdot L = q \cdot \frac{\lambda}{2} \qquad \text{with} \qquad q = 1, 2, 3... \tag{4.3}$$

With this setup, a coherent standing wave is established in the resonator. A part of this light can be coupled out with one of the resonator mirrors with lower reflectivity ($\approx 80\%$) e.g. a Gaussian variable reflectivity mirror to ensure good beam parameters.

This process continuous until the whole population inversion is exhausted, or until the losses in the resonator (out coupling, diffraction, reflection, closed Q-switch) becomes dominant. If the population inversion is maintained with a corresponding pump source in a way that the losses are compensated, **continuous wave** (cw) laser action will result. In case the degradation rate of the population inversion is larger than the pump rate, laser pulses will occur.

The active laser material which is used in the ALADIN airborne demonstrator laser transmitter is **Neodymium doped Yttrium Aluminium Garnet** (Nd:YAG). Nd:YAG lasers are a subgroup of solid state lasers with four energy levels at which population inversion can be relatively easily be achieved, due to the energy level configuration and the fluorescence lifetime in a Nd:YAG crystal. A simplified energy level diagram of a four level laser is shown in figure 4.3.

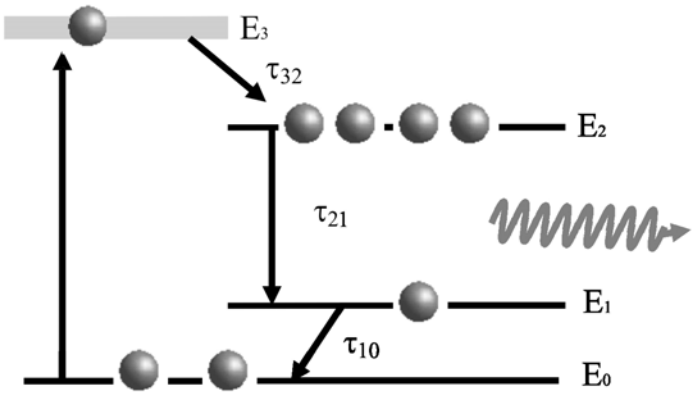

Figure 4.3: Simplified energy level diagram of a four level laser. E_0, E_1, E_2 and E_3 are the different energy levels, and τ_{32}, τ_{21} and τ_{10} are the fluorescent lifetimes between the respective energy levels [Reitebuch and Fix 2006].

Using a flash lamp or a diode laser, the atoms from the ground level E_0 are excited to E_3. Due to non-radiative relaxation which is caused by the emitting of mechanical vibrations in the surrounding crystal lattice, the atoms make a transition to level E_2.

When there are few to zero excited atoms in E_1 due to thermal excitation, population inversion between E_2 and E_1 can be reached. Therefore the life time configuration τ of the energy levels has to be $\tau_{21} >> \tau_{32}$; $\tau_{21} >> \tau_{10}$. The relaxations time τ_{32} between the energy levels E_3 and E_2 for a Nd:YAG crystal is 30μ s [Koechner 1988]. The radiative live time τ_{21} is 550μ s, and τ_{10} is $0,03\mu$s. Therefore all excited atoms will stay a relatively long time at E_2 and *population inversion* can be reached.

The gain spectrum of laser materials does not show narrowband frequency distribution. For a Nd:YAG laser, there are two effects of linewidth broadening which are due to thermally activated lattice vibrations in the active laser material. This vibration produces slightly different values for the exact energy levels of the atoms, and thus slight shifts in transition frequencies. If the local lattice surroundings are similar for every atom but vibrate rapidly and randomly in time, the vibrations will produce a dynamic *homogeneous phonon broadening* [Hitz et al. 2001]. In case the surroundings are different from site to site, due to defects, dislocations or lattice impurities at the laser crystal, the vibrations will produce a static *inhomogeneous lattice broadening* [Siegman 1986]. These broadening mechanism results in a gain spectrum of a Gaussian shape, which amplifies a bandwidth of frequencies. For a Nd:YAG laser the gain spectrum linewidth is 45 nm, respectively 120 GHz, depending on ambient preassure and crystal doping.
The resonance condition (eq. 4.3) shows that only longitudinal modes with a frequency separation of $\Delta f = \frac{c}{2 \cdot n \cdot L}$ can exist within the resonator. Concerning the A2D laser transmitter the cavity length is about 30 cm, and therefore the frequency distance between two longitudinal modes Δf is approximately $\frac{3 \cdot 10^8 \frac{m}{s}}{2 \cdot 0{,}3\mathrm{m}} = 500$ MHz. Furthermore logitudinal resonator modes are not infinitely sharp in frequency. Due to the amplification of the photons emitted spontaneously by the active laser medium, a phase noise is generated. This is caused by spontaneous photons which do not have any relation to the stimulated emitted ones. This process leads to a minimum level of the frequency stability of a laser described by the *Schawlow-Townes noise* [Koechner 1988]. From this follows that logitudinal modes do not have sharp edges, but a Lorenz shape. The combination of the

gain spectrum and the resonator modes which are higher than the gain threshold (due to losses) leads to the modes which can oscillate in a resonator (figure 4.4).

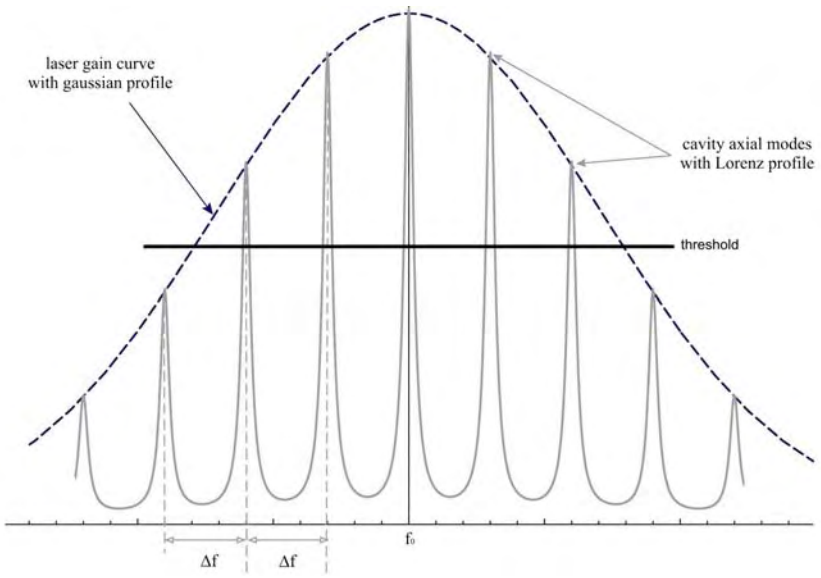

Figure 4.4: Relation between the gain spectrum and the resonator modes in a laser system. Only the longitudinal modes within the gain spectrum and above the gain threshold are amplified and emitted.

After some resonator round trips only the mode(s) in the center of the gain spectrum are amplified at cw operation. For pulsed lasers several modes within the spectrum are amplified. To reduce the spectral range of such a pulsed laser, some arrangements can be taken. One way is to lift the gain threshold due to internal losses. Another one is to control the cavity length in a way, to amplify only one longitudinal mode.
One active method which influences the output spectrum of a pulsed laser is the injection seeding method, which is explicitly discussed in the next section.

4.2 Single frequency operation

To meet the required frequency stability also in high vibrational environments, an active frequency control is necessary. For the A2D laser transmitter, first single-mode operation was achieved by injection seeding the oscillator in combination with the **Q-switch build up time** (QBUT) minimisation technique [Schröder et al. 2007].
With this configuration, the frequency stability requirement was met under laboratory conditions, but not within the vibrational environment of the Falcon 20 aircraft. To reach the required frequency stability during flight, a faster cavity control using the **ramp and fire** (RF) technique was developed and implemented in the A2D laser. The injection seeding method and the ramp and fire technique are discussed in the following section.

4.2.1 Injection seeding

Injection seeding is a method of controlling the spectral properties of a laser [Schmitt and Rahn 1986]. With this technology single longitudinal mode output can be achieved also for high power lasers. Injection seeding uses a low power output laser with a narrow spectral bandwidth, referred to as the seedlaser, to control the properties of an oscillator with higher power, referred to as the power oscillator [Barnes 1993].
To obtain single longitude mode output with the seedlaser, a very short resonator which spreads the mode distance in a way that only one mode has sufficient gain, is necessary. Additionally the effect of spatial hole burning, caused by standing waves, should be eliminated for high frequency stable lasers. Because the nodal planes of the standing waves represent regions of unexploited inversion which will preferentially contribute gain to other modes, can lead to mode hopping [Koechner 1988].
All these features are combined in a **non planar ring oscillator** (NPRO), first described by Kane and Byer 1985, which is implemented in the A2D seedlaser. As it is shown in figure 4.5, a low-noise diode laser pump source is coupled into the active laser material and travels around in a way that no standing wave is obtained. Due to the small resonator

length of some millimetres, the distance between two longitude modes can be estimated with some GHz, and therefore only one mode gets sufficient gain for amplification.

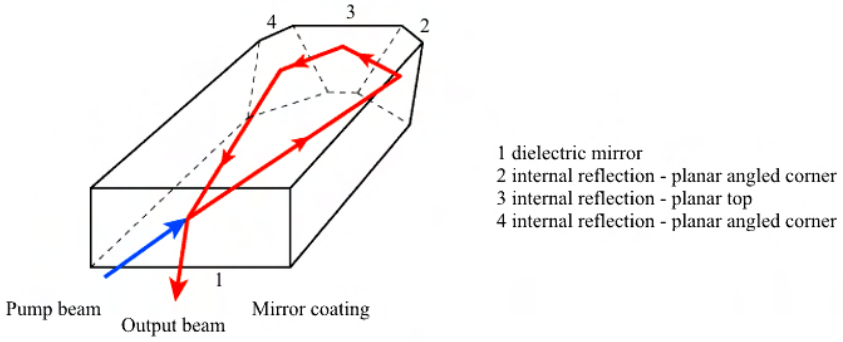

Figure 4.5: Principal of a non planar ring oscillator [Koechner 1988].

This spectral bright seedlaser radiation is injected into the resonator of the power oscillator by a polariser (in case of A2D) or one of the resonator mirrors, and serves as a seed from which the pulsed laser output grows. As mentioned in section 4.1, naturally occurring laser pulses begin from the zero point energy of the laser resonator, or from spontaneous emission. But when the seedlaser radiation with enough power is inside the resonator while opening the Q-switch, the pulse growing from the injected seed will deplete the gain of the laser material, before pulses from spontaneous emission become large. If this process happens, the laser output will have the properties as the seedlaser rather than the properties of the free running one. The theory of injection seeding is discussed in detail by Barnes 1993.

One challenging goal for reaching high frequency stability, and for using the injection seeding method correctly, is to warranty a good mechanical stability of the resonator length, and to open the Q-switch exactly in that moment, where the resonator length is in resonance with the seedlaser radiation. Therefore a ramp and fire stabilisation method is used and discussed in the next section.

4.2.2 Ramp and fire cavity control

In comparison to ground based lidar systems the vibrational load, mainly caused by engines and wings, is much higher in airborne systems, especially at frequencies of some hundred Hz or even some kHz. This vibration can lead to a disturbance of the cavity length and thus to a disturbance of the resonance frequency. For this purpose an active frequency control is realized at the A2D. This active frequency control is based on injection seeding technology [Barnes 1993] in combination with a **ramp and fire** (RF) frequency control method [Fry et al. 1990, Schmitt and Rahn 1986, Nicklaus et al. 2007] which is realized with the A2D laser from Fraunhofer-Institut für Lasertechnik ILT [ILT 2006].

The RF cavity control method utilizes the Fabry-Perot property of the cavity. Therefore it is necessary to change the cavity length constantly (ramp). This is realized with a **piezoelectric translator** (PZT) mounted **on a variable reflective mirror** (VRM), which is used as the output coupler in the LPO (see figure 3.2). The seedlaser radiation is coupled into the cavity via the polarizer of the Q-switch. The light leakage of the seedlaser is monitored with a photodiode, which is placed close to the polarizer and perpendicular to the LPO resonator axis. The photodiode signal is produced by interference between the part of the incident seed light that does not pass through the complete cavity and the part that has made one or more complete round trips trough the cavity. As the cavity length is ramped, the interference signal reaches a maximum when these two parts of the seed beam are in phase. At this point the seedlaser is in resonance with the cavity, and the laser pulse should be emitted by opening the Q-switch [Walther et al. 2001]. To get sufficiently good trigger resonance signals, the cavity is not fully closed before the pulse extraction, but operates a bit below lasing threshold. Figure 4.6 shows the typical behaviour of the resonance signal at the end of the pump pulse depending on the PZT movement.
This method can lead to very high frequency suppression, because the time between trigger detection and pulse release can be very short (up to 30 μs) and thus operates

for vibrations up to $\frac{1}{30\mu s} = 30$ kHz. The disadvantage of this method is a jitter in the trigger time from pulse to pulse.

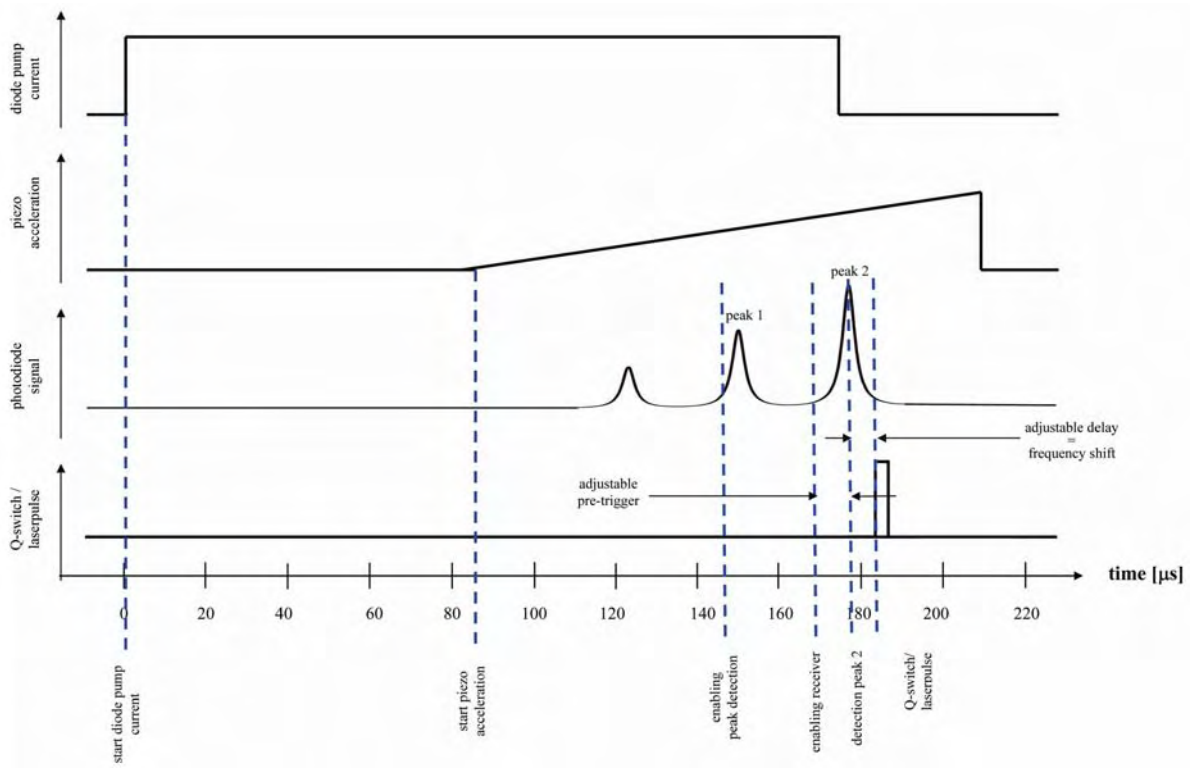

Figure 4.6: Timing sequence of the A2D cavity control.

Due to this timing jitter the RF method does not allow to predict the exact time of pulse extraction from pulse to pulse. But often the knowledge of the exact pulse release time is required prior to the actual pulse extraction, in order to trigger the start of the receiver data aquisition. The A2D system detector unit, for example, requires an exact pre-trigger in the range of 60 μs with a time jitter below 100 ns. To achieve this, the RF method [Hovis et al. 2004] has been modified by measuring more than one resonance peak in the piezo ramp. The first resonance peak is used to trigger the electronics, and the pulse is fired at the second peak or with a fixed delay to the second peak (figure 4.6). The latter method is called **ramp delay fire** (RDF) [ILT 2006]. If the piezo movement is sufficiently linear, a fixed delay leads to high frequency stability and a very low jitter

between pre-trigger and pulse extraction. If the piezo movement is not linear the RDF method will lead to a frequency jitter of the output pulse and the RF method might be the better solution for high frequency stability at the cost of timing jitter between pre-trigger and actual emitted laser pulse.

4.3 Methods of frequency characterisation

This section describes the methods of frequency measurement in this thesis. It gives a short overview of the different measurement devices, shows their setup, and their functional principle.

4.3.1 Heterodyne unit

A heterodyne unit, which was developed at DLR [Schröder et al. 2007], is used for measuring the spectral bandwidth and the relative frequency jitter between seedlaser and LPO for every single laser pulse. Therefore the pulsed LPO beam is heterodyned with a reference beam with known frequency. Figure 4.7 shows the schematic setup of a heterodyne unit.

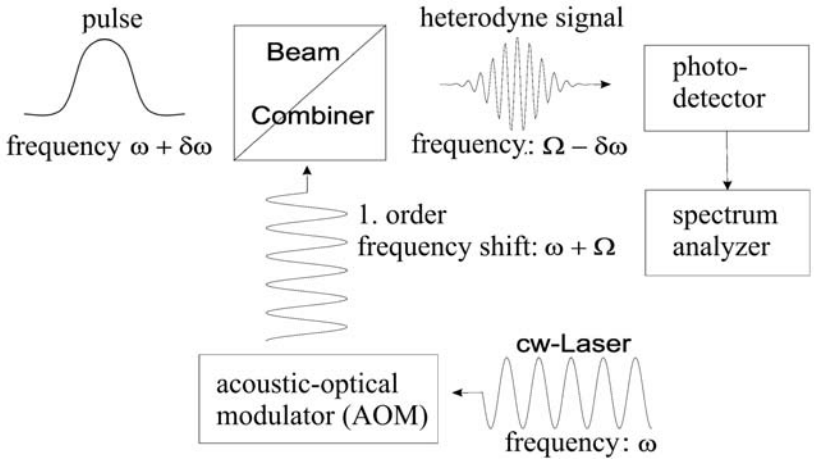

Figure 4.7: Principal setup of a heterodyne unit, which is used for frequency jitter and spectral bandwidth measurement [Schröder et al. 2007].

To shift the cw seedlaser frequency by a known frequency offset, an **acoustic-optical modulator** (AOM) is used. The principle of an AOM is shown in figure 4.8.

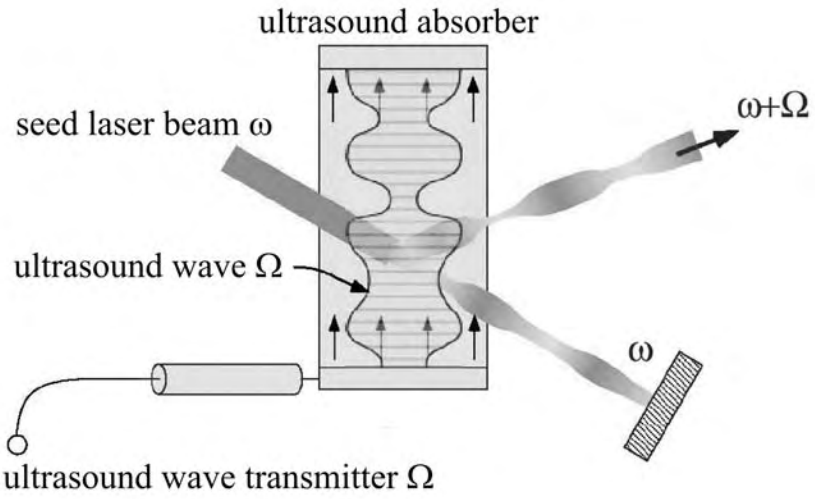

Figure 4.8: Principle of an acoustic-optical modulator [adapted from Eichler and Eichler 2003].

The plane ultrasound wave acts like a moving phase grating for the seedlaser beam. On this grating, Bragg reflection occurs. Therefore the first-order diffracted beam gets a defined frequency shift of $\pm\,\Omega$, where Ω is the angular frequency of the ultrasound wave, propagating in the AOM.

Reference beam and pulsed beam are optically mixed with a beam combiner. The intensity of the detected signal includes the sum and the difference of both frequency components. Due to the limited bandwidth of the photo detector, the sum of the frequencies can not be measured, but the difference is a low-frequency signal, called beat signal, which can be determined with high accuracy. With this signal, the frequency jitter between seedlaser and LPO pulses can be determined. Due to the AOM frequency stability of $5 \cdot 10^{-5}$ at 200 MHz, the systematic error of beat frequency measurement is smaller than 10 kHz. Also the spectral bandwidth of the laser pulse can be determined by Fourier transformation of the time series of the beat signal. Disadvantage of this method is that the frequency of the pulsed laser can only be determined relative to the seedlaser frequency. Thus, no frequency drift of the seedlaser can be detected.

4.3.2 Wavemeter

To obtain an absolute laser pulse frequency measurement, a commercial**wavelength meter** (WLM) from High Finesse (WSU - 10) [High Finesse WS Ultimate] is used. The schematic setup of a WLM is shown in figure 4.9.

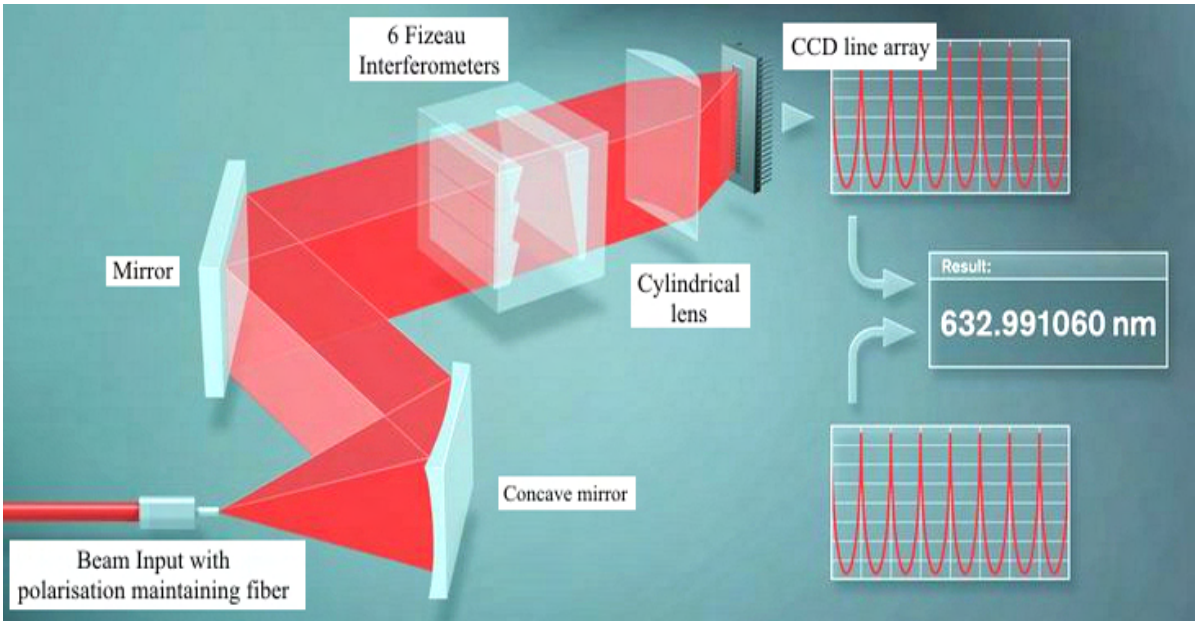

Figure 4.9: Principle setup of a wavelength meter. The laser beam is coupled into the WLM with a polarisation maintaining fiber. Then the beam is collimated with a concave mirror and is linked to 6 different Fizeau interferometers, where the beam generates interference patterns. These patterns are measured with a CCD line array, and therefore the wavelength and frequency is calculated [High Finesse WS Ultimate].

The WLM can be used for continuous and pulsed laser radiation. The laser beam is coupled into the wavemeter with a polarisation maintaining single mode fibre. Afterwards the beam is collimated with a concave mirror. Then the beam is navigated by a prism into 6 different Fizeau interferometers with different spectral ranges and finesse. The generated interference patterns are detected with a CCD detector which is linked to a computer. By correlating the single interference patterns and comparing them with

a calibration file, the wavelength of the incident beam can be determined. With the WSU-10 WLM a relative accuracy of $2 \cdot 10^{-8}$ which is equivalent to 10 MHZ or 4,2 fm at 355 nm, can be reached [High Finesse WS Ultimate], (see Appendix, figure A.2). With a cw He-Ne calibration laser (see Appendix, figure A.3), the accuracy of the WLM was verified during a 22 min. measurement to be even better than 1 MHz (figure 4.10).

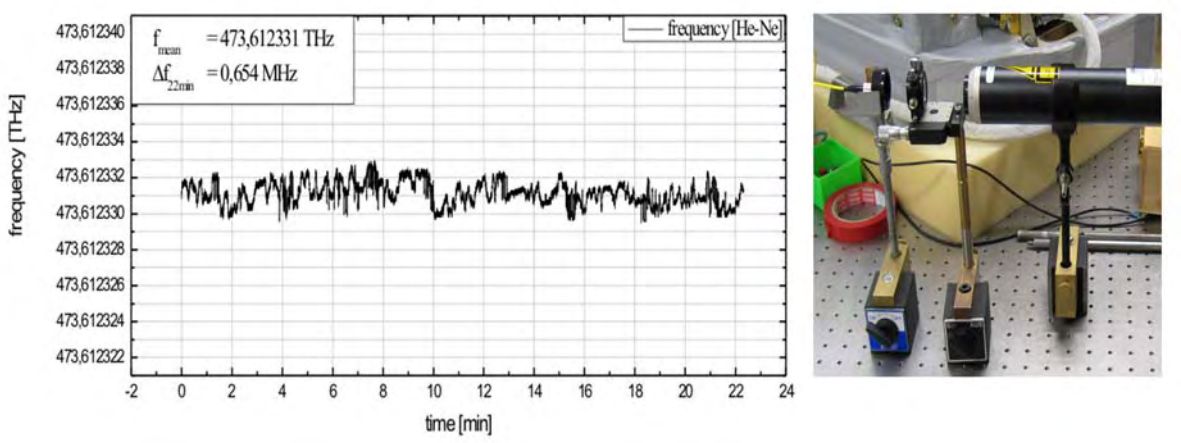

Figure 4.10: He-Ne laser frequency, measured with the WLM, versus time (left). On the right photo, the setup for WLM calibration is shown. The He-Ne calibration laser is coupled into a polarisation maintaining fiber, which is linked to the WLM (not shown).

4.3.3 Optical spectrum analyzer

The third measurement device which is used to analyse the spectral properties of the laser beam is a commercial **optical spectrum analyser** (OSA) from Yokogawa - Ando (AQ 6319) [Yokogawa AQ 6319]. The OSA can be used to measure the seed and LPO laser line spectrum. Figure 4.11 describes the basic concept of an OSA.

Similar to the other measurements, the laser light is coupled into the OSA with a polarisation maintaining single mode fiber. Then the light impinges on a rotating grating,

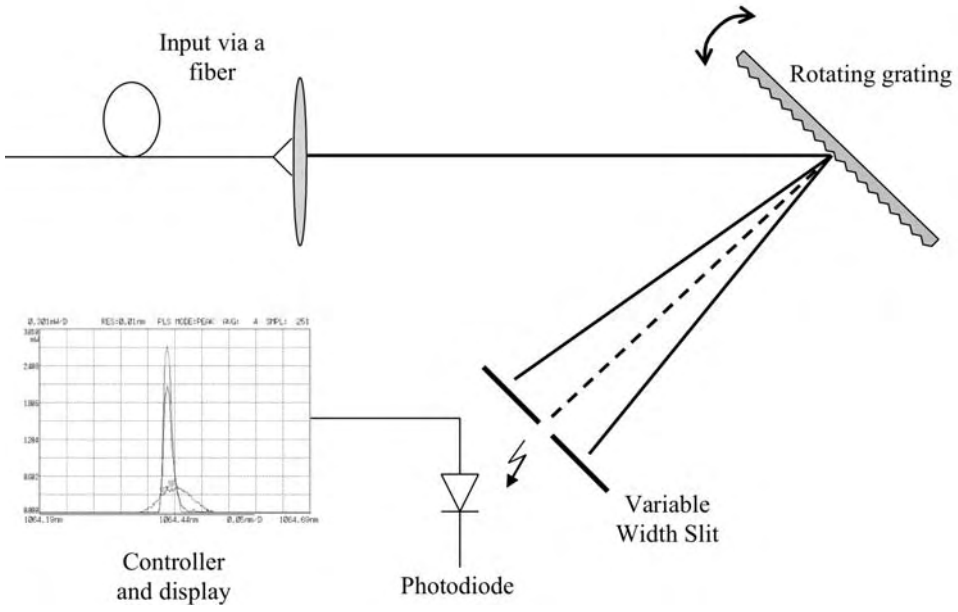

Figure 4.11: Schematic setup of an optical spectrum analyzer.

where it is split, being distributed according to its wavelength (Bragg diffraction). With the grating angle and the velocity of the grating movement, the span and the sweep of the measurement can be adjusted. Next, a variable-width slit is used to select only the wavelength desired, which is focussed on a photo detector. With changing the slit width, the resolution of the measurement can be adjusted. So the OSA can measure optical power levels versus the wavelength and can be used to measure the wavelength emitted by the laser. The OSA wavelength accuracy is $\pm$ 50 pm over the full range [Yokogawa AQ 6319].

4.4 Frequency spectrum of seed and LPO laser

4.4.1 Characterisation of the frequency spectrum

Due to the strong temperature dependency of the refraction index of the laser active material, the LPO gain spectrum changes its position in dependence of the crystal temperature. To obtain the LPO gain spectrum position in reference to the used seedlaser radiation, spectrum measurements with an OSA and a WLM were performed. For both measurements, the radiation was coupled into a polarisation maintaining single mode fibre which was linked to the respective measuring device. In figure 4.12 the result of LPO spectral measurement with the OSA is shown.

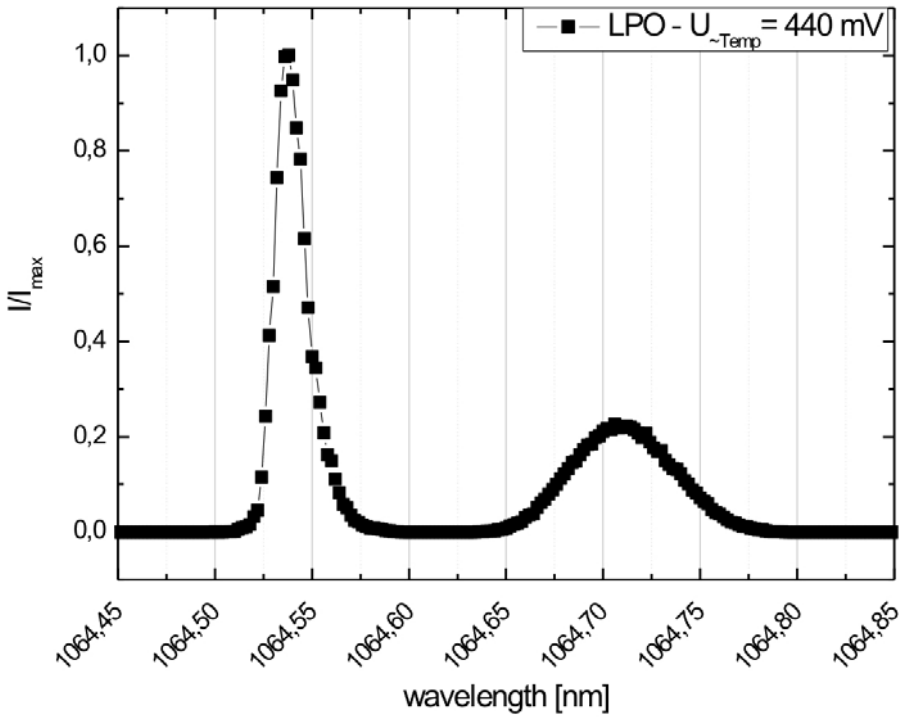

Figure 4.12: Normalized intensity of the LPO laser depending on wavelength measured with the OSA.

With the OSA, the normalized intensity is measured depending on the wavelength. Figure 4.12 shows a main maximum of intensity at 1064,54 nm. This is the wavelength of the LPO laser caused by injection of the seedlaser radiation with its wavelength. About 15 nm beside this peak at 1064,71 nm a secondary maximum was measured. This is an indication for no single frequency operation of the LPO laser, but despite this secondary peak no effects of frequency or mode-hopping were recognisable with the WLM.

According to the secondary peak is probably the spectral difference between seedlaser radiation and the maximum of the gain spectrum. According to the measured values it can be assumed that the gain spectrum of the LPO is at wavelengths of 1064,71 nm, but the seedlaser radiation is at 1064,54 nm. To verify this assumption, the seedlaser and the free running (unseeded) LPO were analyzed in more detail.

Therefore the seedlaser was coupled into a polarisation maintaining single mode fibre which was connected to the OSA and the WLM. To obtain spectral information of the unseeded LPO, it was necessary to deactivate the active cavity control stabilisation. The results of the OSA and the WLM measurement of the unseeded LPO and the seedlaser are shown in figure 4.13.

With these measurements, the assumption of the difference between seedlaser and the free running LPO was verified. The linewidth of the unseeded LPO laser (figure 4.13, left, black line), with a centre wavelength of 1064,69 nm is about 0,13 nm (FWHM: full width half maximum), which is a third of the Nd:YAG typical linewidth (figure 4.4) [Koechner 1988]. The linewidth of the seedlaser (figure 4.13, left, red line) is about 0,05 nm, but due to the low resolution of 0,02 nm of the OSA measurement, the spectral width of the seedlaser is significantly broadened by the OSA. This was verified with a WLM measurement (figure 4.13, right side). The spectral range in the free running laser is around 60 pm (figure 4.13, right, top) whereas the range of the seedlaser is only 14 fm

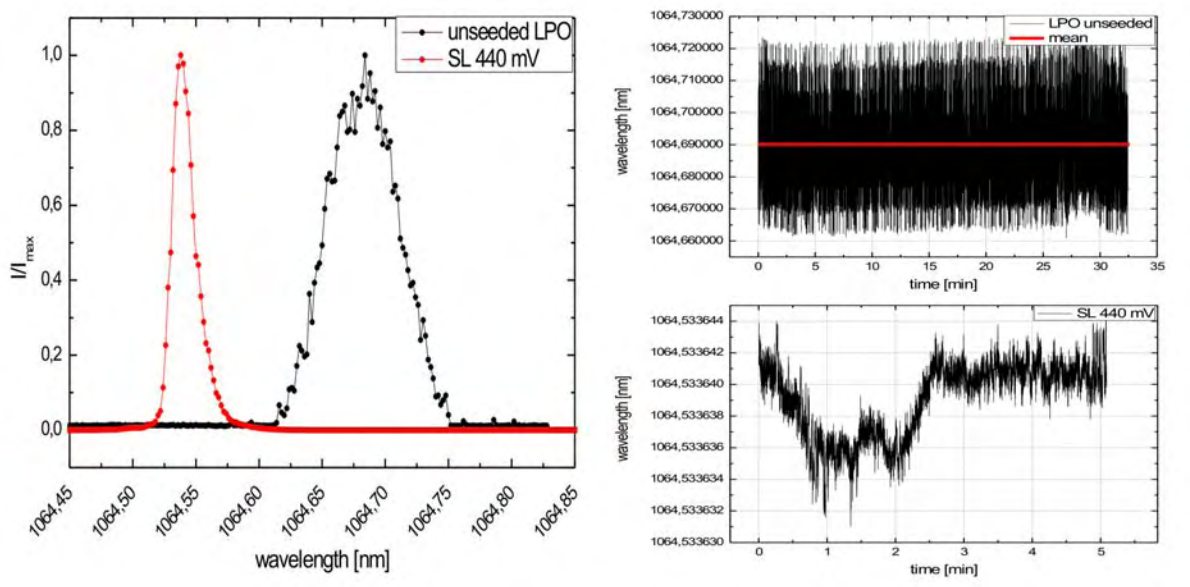

Figure 4.13: On the left hand side the spectral difference of the seedlaser (red) and the unseeded LPO (black), measured with the OSA is shown. On the right hand side, the corresponding WLM measurement for unseeded LPO (top) and seedlaser (bottom) is shown.

(figure 4.13, right, bottom), which is one order of magnitude smaller.
Another interesting fact was shown with this measurement. Although the seedlaser wavelength is not in the range of the LPO gain spectrum (at least not with the OSA sensitivity), the process of injection seeding does work properly with the actual seeding configuration.

4.4.2 Optimisation of seedlaser temperature

To match the seedlaser frequency to the unseeded LPO gain spectrum the seedlaser must be tuned in the right direction, and there are two possibilities to tune the seedlaser in its frequency. The first and fast one is a modulation of the diode pump current. If the pump current increases, also the charge carrier density in the active zone of the semiconductor material and therefore its refraction index will increase. With this refraction index

increase, the optical wavelength calculated with $x_{res} = c \cdot n_{semi} \cdot t$ is increasing too. In this equation x_{res} is the optical path length in the NPRO for the travelling wavelength, c is vacuum light velocity, n_{semi} the diffraction index of the NPRO material and t is the time for one round trip in the crystal. In case the optical wavelength becomes to long for the actual longitudinal mode, the next one will oscillate. This process is called mode-hopping. Due to the manufacture of the seedlaser, the distance between to modes is about 15 GHz [Innolight 2004].
The second and slower method of wavelength variation is realized by changing the temperature of the NPRO crystal. In this case, the increase of the refraction index, and therefore the optical wavelength due to a temperature increase is the reason for a change in wavelength. The temperature of the NPRO can not be measured directly, but a thermo element which is placed at the surface of the laser crystal yields a voltage which is proportional to the NPRO temperature. Despite the non-linearity between seedlaser temperature and thermo element voltage, 10 mV are equivalent performed to 1 °C in the area of operation [Innolight 2004]. The measurement results of temperature dependency of LPO IR radiation, measured with the OSA, and laser output UV radiation, measured with the WLM are shown in figure 4.14.

The seedlaser temperature for the A2D laser system was set to 44,2 °C (442 mV). The corresponding seedlaser wavelength was measured with the OSA to 1064,52 nm (figure 4.14, top, maximum of the blue curve), and the resulting frequency of the outcoming UV beam was measured with the WLM as 844,860 THz. For a higher temperature of 46,5 °C (465 mV), the LPO wavelength increased to 1064,58 nm (figure 4.14, top, yellow curve) and the UV frequency decreased to 844,830 THz. For a still higher temperature of 47,5 °C (475 mV) the wavelength decreases to 1064,55 nm (figure 4.14, top, magenta curve) and the UV frequency increased to 844,852 THz. This is a result of mode hopping which is due to the continuous resonator length increasing. The green curve (figure 4.14, top, 1064,62 nm) and the red curve (figure 4.14, top, 1064, 64 nm) show the further spectral behaviour of the seedlaser radiation while temperature increase (50,7 °C (507 mV), 53,5 °C (535 mV)). It is obvious, that the seedlaser radiation comes closer to

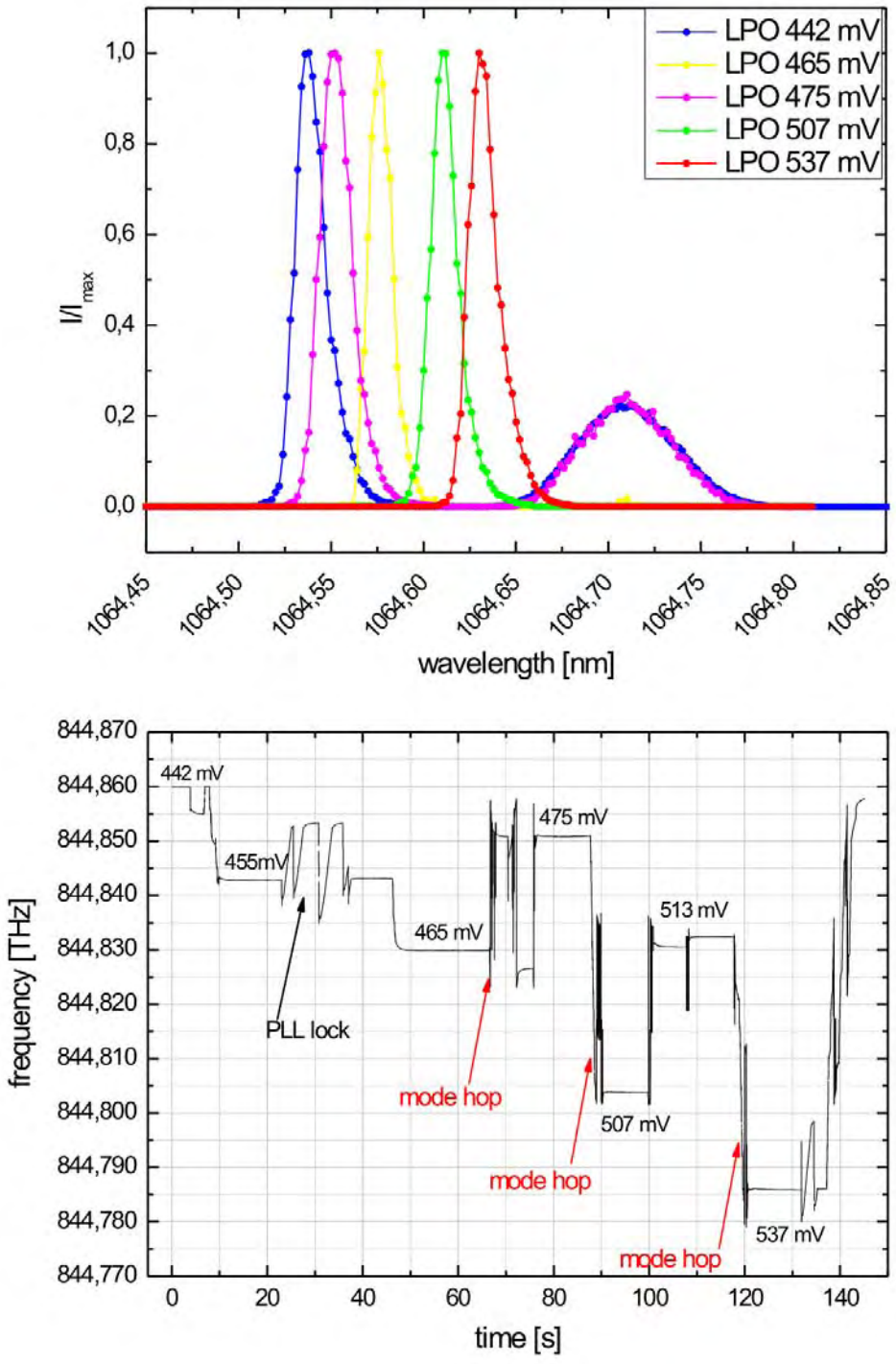

Figure 4.14: In the upper diagram, the normalized spectrum of the LPO depending on seedlaser temperature are shown; different colors indicate different thermo-element voltages. The corresponding WLM measurement of the of the UV frequency is shown in the lower diagram.

the gain spectrum maximum of the LPO for higher temperatures.
Remarkable to note is that the secondary peak in the LPO spectrum disappears almost completely for seedlaser temperatures above 50 °C. This can be explained with the better match of the seedlaser wavelength, and the fundamentals of the injection seeding technique. If the seeded photons have their energy closer to the gain spectrum, nearly all excited atoms will emit at the seedlaser frequency.
With this measurement it was be shown that the higher seedlaser temperature will shift the seedlaser frequency closer to the gain spectrum of the LPO laser.

To get a direct relation between wavelength and the seedlaser temperature, a continuous temperature tuning between 40 °C and 60 °C was done next. Therefore, the UV radiation was measured with the WLM depending on the seedlaser temperature, which was recorded with an oscilloscope. The result of this measurement is shown in figure 4.15.

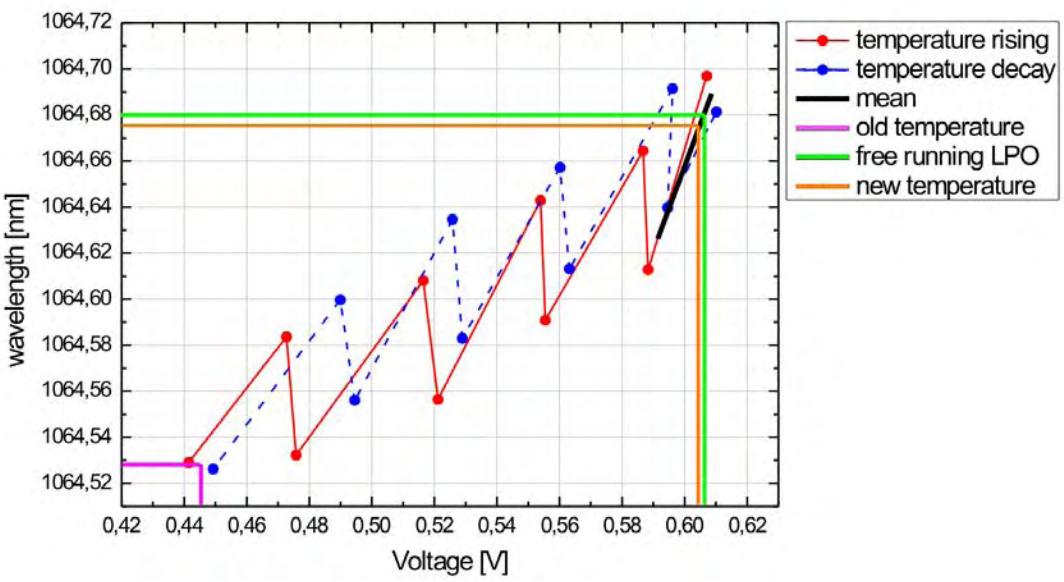

Figure 4.15: Wavelength measured with the WLM of the seeded LPO while temperature increase (red curve) and temperature decrease (blue curve); the old/new temperature/wavelength are shown in magenta/yellow, and the values for the free running LPO in green.

The red and the blue line in figure 4.15 show the wavelength of the seedlaser depending on its temperature. The hysteresis of this curve is due to the difference between the surface crystal temperature which is measured with the thermo-element, and the temperature at the inner crystal. To find the optimum position for the new seedlaser temperature, the mean value of the hysteresis curve close to the unseeded LPO wavelength was determined (figure 4.15, black curve).
To find the right seedlaser temperature it was necessary to consider that the new wavelength is far enough away from a mode hop. This is important due to the fact that a frequency tuning over 15 GHz has to be possible for A2D receiver interferometer calibration. With the relation $\frac{\Delta f}{f} = -\frac{\Delta \lambda}{\lambda}$, the frequency change of 15 GHz (@ 1064,68 nm) leads to a wavelength change of 0,056 nm. With this information and the mean value of the hysteresis curve (figure 4.15, black), it was decided to increase the seedlaser temperature, and therefore also the reference laser temperature to 60,6 °C (606 mV) (orange line). With this adjustment, the seedlaser spectrum is only 0,05 nm away from the gain maximum of the free running LPO.
After the temperature modification, the wavelength of the LPO laser was measured with the OSA and is shown in figure 4.16 in comparison to wavelengths of other temperature settings (from figure 4.14).

Figure 4.16 shows the seedlaser frequency spectrum for temperatures not matching the unseeded LPO spectrum (grey lines), and for the determined new seedlaser temperature (red curve).
It is obvious in this figure, that the secondary peak at the gain maximum of the LPO was eliminated with the new seedlaser temperature. This change did not have any remarkable influences to the frequency stability, but the energy per pulse in the UV laser power has increased more than 10 % , from 60 $\frac{mJ}{\text{pulse}}$ to 70 $\frac{mJ}{\text{pulse}}$ after this modification.

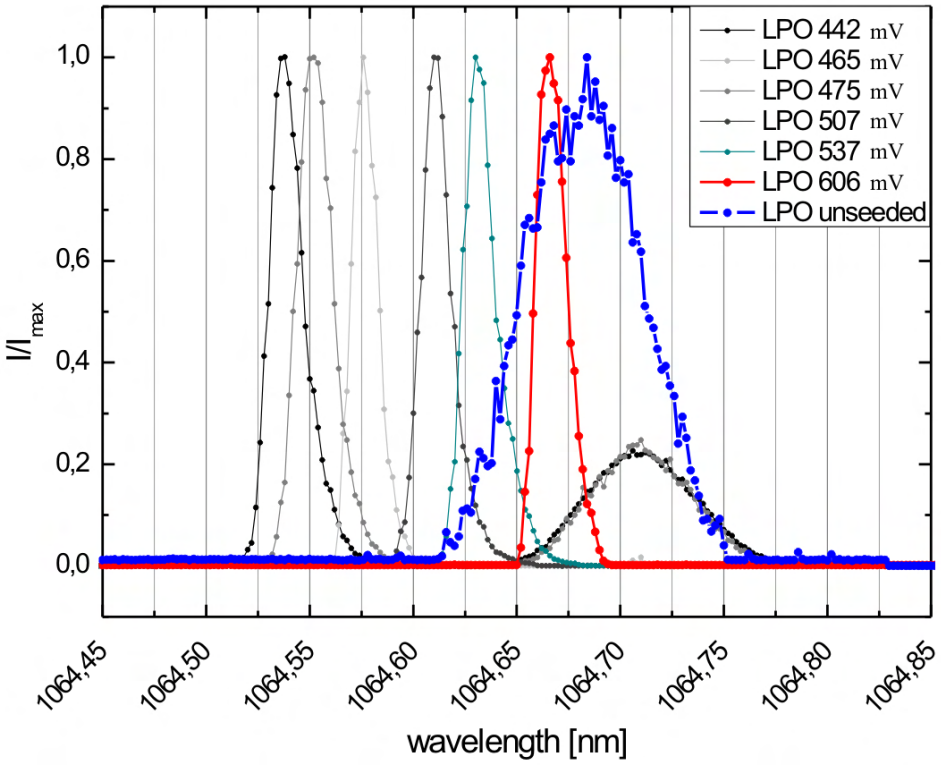

Figure 4.16: Normalized spectrum from the unseeded LPO (blue), the seeded laser with old temperature settings (grey), and the new seedlaser temperature (red).

4.5 Frequency measurement during vibrations

The first test flight with the A2D has been carried out in October 2005. During this test flights it was realised that the high vibrational levels within the aircraft prompts the laser to unseeded operation. Therefore no accurate wind measurement using the Doppler effect was possible with this laser transmitter configuration. It was realised that the QBUT minimisation technique works well in laboratory [Schröder et al. 2007], but is too susceptible for vibrations. To obtain a seeded laser operation despite these vibrational levels, a mechanical cavity stabilisation and the new ramp fire, and ramp delay fire cavity control method was developed (section 4.2.2).

4.5.1 Measurements in laboratory

To verify the frequency stability with the new active frequency control configuration, a vibration test in laboratory was accomplished. Therefore the laser system was fixed onto an aluminium plate, which was hanged up with 22 expanders. Near the centre of gravity of the laser an electrodynamics vibration shaker was positioned and fixed by a rod to the lower side of the aluminium plate. A photo of the test setup is shown in figure 4.17.

In order to measure the acceleration levels at different positions, 3-axis accelerometers were fixed on the laser platform. The excitation was realised by using a random signal in the x and z direction created by a shaker control system. The applied vibration spectrum during the test from frequencies of 10 - 2000 Hz was extracted from measurements of vibration levels during test flights in 2005. With these vibrational levels it was possible to simulate the excitation spectrum in the aircraft across the whole frequency band from 10 - 2000 Hz.

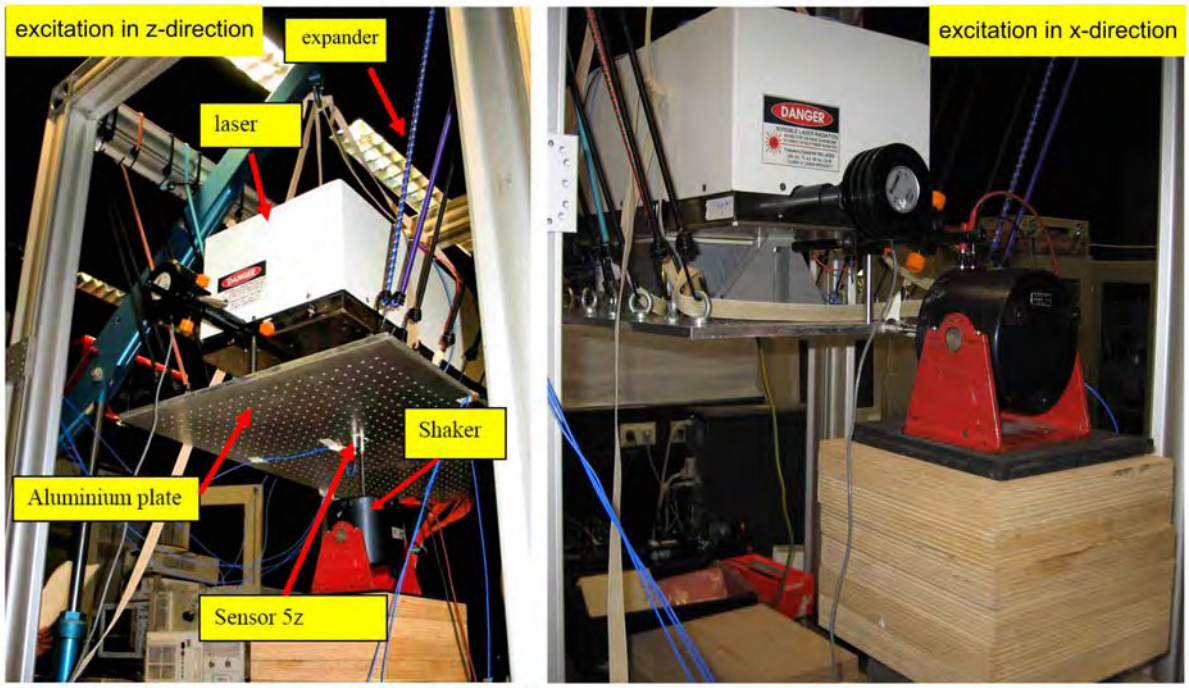

Figure 4.17: Setup for vibration test at EADS-Astrium (Ottobrunn) in z-direction (left) and x-direction (right).

During the vibration test, different control loop settings for the cavity control using the RF and RDF technique were tested. The frequency stability was measured with the heterodyne unit, and the timing jitter between estimated and actual pulse release was estimated with an oscilloscope.

The requirement for the frequency stability of the A2D laser system is 4 MHz rms (UV) which is equivalent to 1,3 MHz (IR), and the timing jitter should be below 100 ns.

The summarised results of frequency and timing stability measurements during the excitation in z- and x-directions are shown in table 4.1 and 4.2. The red printed values are not compliat with the requirements for the A2D laser.

	Operation mode	Settings	Standard deviation of frequency [MHz]	Standard deviation of timing [ns]
without excitation	RF	-	0,202	-
		-	0,206	-
	RDF	-	0,453	0,3
		Z1 = 100, Z2 = 50, PR4 = 14 µs, Dyn. = slow	0,350	-
		Z1 = 100, Z2 = 50, PR4 = 14 µs, Dyn. = fast	0,392	-
Random excitation in z-direction $2{,}5{\cdot}10^{-3}$ [(m/s²)²/Hz] (10 - 100) Hz	RF	-	0,615	43
		-	0,379	43
		-	0,409	43
	RDF	PR4 = 12 µs	0,455	1,7
		PR4 = 14 µs	0,506	1,7
		PR4 = 16 µs	0,428	1,7
		PR4 = 14 µs, PZ1 = 100 µs, PZ2 = 50 µs	0,399	1,7
Random excitation in z-direction $2{\cdot}10^{-4}$ [(m/s²)²/Hz] (100 -2000) Hz	RF	Dyn. = fast	0,845	260
		Dyn. = slow	0,638	190
	RDF	-	3,730	1,5
		Dyn. = fast	3,899	11
		Dyn. = slow	3,015	11
		Dyn. = off	3,056	-
		Dyn. = fast, PR4 = 14 µs, Z1 = 100, Z2 = 50, p-controller = 0,2	3,110	-
		Dyn. = slow, PR4 = 14 µs, Z1 = 100, Z2 = 50, p-controller = 0,5	3,420	-
		Dyn. = slow, PR4 = 14 µs, Z1 = 100, Z2 = 50, p-controller = 0,1	3,177	-
Random excitation in z-direction 2,5·10-3 [(m/s2)2/Hz] (10 - 100) Hz	RF	-	1,731	400
		Dyn. = slow	1,836	600

Table 4.1: Results of frequency and timing stability measurements during vibrational excitation in z-direction. Values in red indicate non-compliance.

	Operation mode	Settings	Standard deviation of frequency [MHz]	Standard deviation of timing [ns]
without excitation	RF	-	0,426	-
	RDF	-	0,431	-
Random excitation in x-direction $2{,}5{\cdot}10^{-4}$ [(m/s²)²/Hz] (10 - 2000) Hz	RF	Dyn. = slow, Z1 = 95, Z2 = 50, p-controller = 0,2	0,705	150
		Dyn. = slow, Z1 = 95, Z2 = 50, p-controller = 0,2	0,816	150
		Dyn. = slow, Z1 = 95, Z2 = 50, p-controller = 0,2	0,687	150
		Dyn. = slow, Z1 = 95, Z2 = 50, p-controller = 0,2	0,712	150
	RDF	p-controller = 0,2, i-controller = 0,2	2,594	1
		p-controller = 0,1, i-controller = 0,2	2,577	1
		p-controller = 0,05, i-controller = 0,2	2,651	1
		p-controller = 0,05, i-controller = 0,3	2,587	1
		p-controller = 0,05, i-controller = 0,4	2,575	1
		p-controller = 0,1, i-controller = 0,3	2,585	1

Table 4.2: Results of frequency and timing stability measurements during vibrational excitation in x-direction. Values in red indicate non-compliance.

In the first column, the shaker settings, which are split in two different frequency ranges, from 10 - 100 Hz and 100 - 2000 Hz, due to technical limits of the shaker are shown. The frequency stability and timing jitter was measured without excitation, with vibrations comparable to the aircraft (**power spectral density** PSD $= 2,5 \cdot 10^{-3} \frac{(m/s^2)^2}{Hz}$ for 10 - 100 Hz and $2 \cdot 10^{-4} \frac{(m/s^2)^2}{Hz}$ for 100 - 2000 Hz), and with vibrations one order of magnitude higher than in the aircraft ($2,5 \cdot 10^{-3} \frac{(m/s^2)^2}{Hz}$ for 10 - 100 Hz). The second column indicates the operation mode (RF or RDF), while the third column shows the respective cavity control settings. The settings were varied concerning the dynamic lookup table operation (off, slow, and fast), the time when the piezo gets ramped (Z_1), and the time when the peak detection of the cavity control gets enabled (Z_2). The parameter PR_4 is the target time for the first peak appearance, and $p-controller$ and $i-controller$ shows the settings for the proportional and integral part of the cavity controller. In the fourth and fifth column, the standard deviation of frequency, measured with the heterodyne unit, and the standard deviation of timing between expected and actual pulse, measured with an oscilloscope are shown. Table 4.2 shows the result of frequency stability and timing jitter measurements during excitation in the x-axis.

Due to the new stabilisation arrangements a seeded operation of the A2D laser was achieved with vibrational levels comparable with aircraft vibration levels all the time. Very good frequency stability, with values below 1 MHz, was achieved with the ramp and fire technique for vibrations in z-directions as well as in x-direction. With this adjustment, the timing jitter exceeds the requirement of 100 ns by a factor of 2-3 for higher vibration frequencies. This will result in an uncertainty of the vertical range gate assignment by 45 m for 300 ns, which is still lower than the minimum vertical range gate resolution of 315 m for 2,1 μs. With the ramp delay fire technique, the timing jitter is in a range of some nanoseconds, but the frequency stability exceeds the requirement of 1300 MHz by a factor of 2-3 for higher vibration frequencies. With both methods, the variation of time Z_1 which is the time between the start of pumping and piezo acceleration, and Z_2 which is the time between piezo acceleration and enabling of peak detection (figure 4.7), and also the variation of the dynamic look-up table, did not lead to remarkable changes in reference to timing and frequency stability.

4.5.2 Measurements during flight

Due to the good frequency stability performance during the vibration test on ground, it was decided to continue with a test flight with the A2D in April 2007. Therefore the laser transmitter, the telescope, the OBA, and all necessary electronics were setup in the DLR Falcon 20 aircraft. The system was fixed onto a Newport honeycomb plate via its mounting isolation system, and the plate was supplied by a special frame built for the integration into the aircraft. A photo the aircraft and the A2D within the aircraft is shown in figure 4.18.
In order to obtain information of the vibration level at different positions during flight operation, several accelerometers were fixed to the seat rails, the mounting rack, and the laser platform.

Figure 4.18: The DLR Falcon 20 aircraft (left) and the A2D integrated in the aircraft cabin (right).

The vibration levels, measured during the flight, were recorded with a sample frequency of 5 kHz [ISMB 2007]. In figure 4.19 the acceleration data for sensor 1 (seat rail) and sensor 3 (laser) in all three axes are shown. Thereby, sensor 1, which was mounted on

the seat rail, measured the vibrations caused by the aircraft, and sensor 3, which was mounted on the laser base plate, measured the vibrations which affect the laser (see figure 4.18 right, for positions).

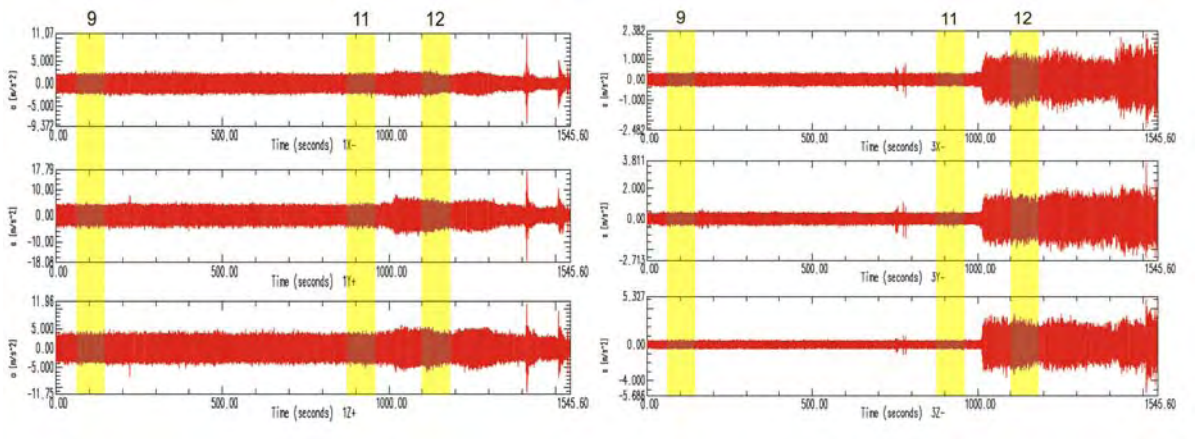

Figure 4.19: Time record which shows the acceleration data in x(top), y(middle), and z(bottom) direction of sensor 1 (seat rail, left) and sensor 3 (laser, right) in $\frac{m}{s^2}$, during travel flight conditions until 1000 s and during descent (1000 - 1550 s) [adapted from ISMB 2007] with the period of the heterodyne measurements (yellow) of figure 4.21; note that the y-axis is scaled differently for each plot.

The yellow marked areas in figure 4.19 indicate the times where frequency measurements using the heterodyne method were done (table 4.3). As obviously in figure 4.19, the acceleration on the seat rail sensor is much higher than on the sensor which is placed on the laser base plate. So the mechanical damping of vibrations did work quite well, applying for travel flight with lower vibrational levels ($\approx$ 0 - 1000 s) as well as for descent flight with higher vibrations ($\approx$ 1000 - 1550 s). In order to obtain the spectral behaviour of the aircraft vibrations, the **power spectral density** (PSD) was computed for 4096 time samples ($\hat{=}$ 0,82 s) and an average PSD during stationary conditions for travel flight. The PSD representative for descent flight were obtained from the maximum amplitudes from single PSD during this period.

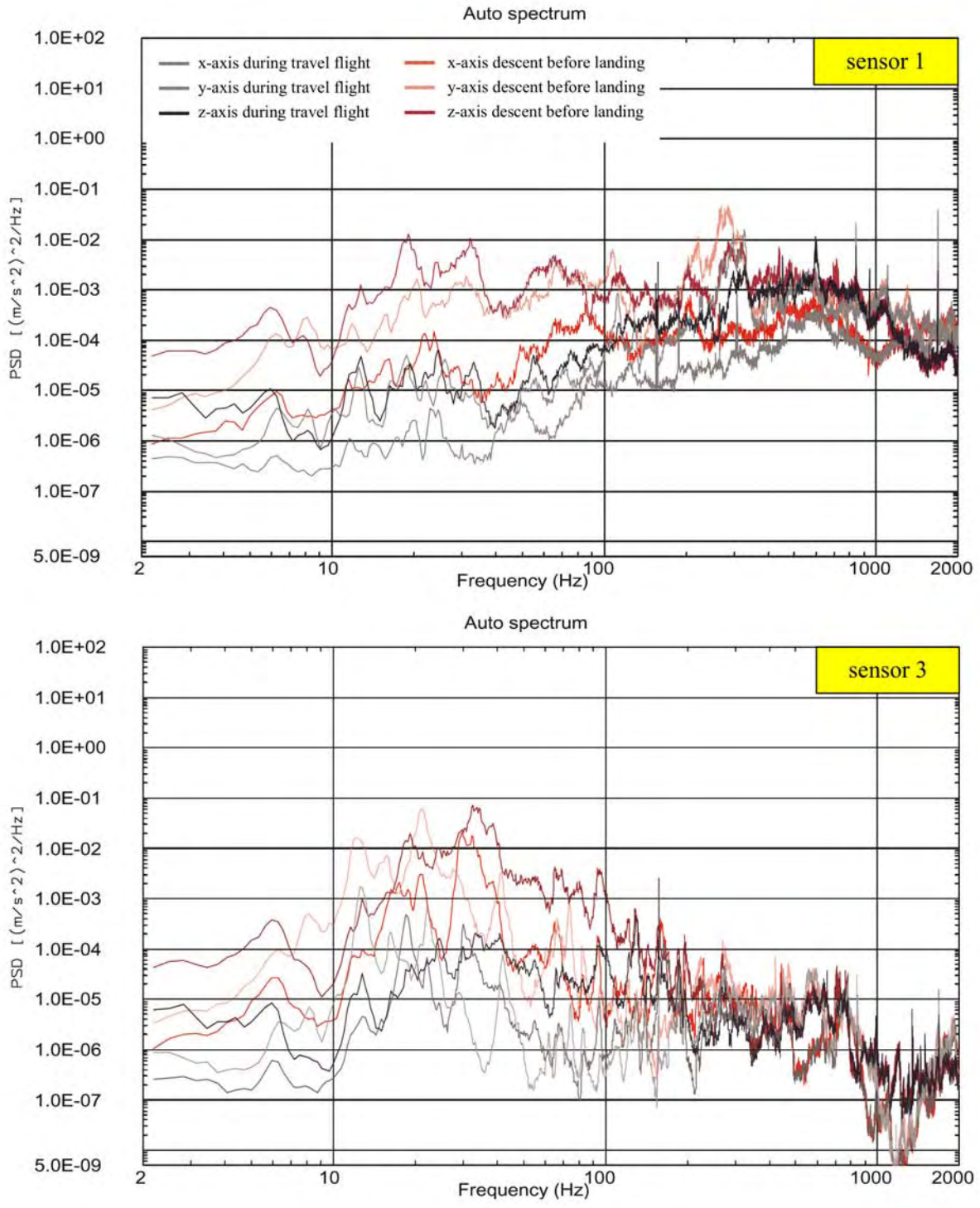

Figure 4.20: Power spectral density of sensor 1 (top) and sensor 3 (bottom) during travel flight (grey colors, average PSD) and descent flight (red colors, maximum amplitude of PSD) in the frequency range from 2 - 2000 Hz [adapted from ISMB 2007].

Figure 4.20 shows the PSD in $\frac{(\frac{m}{s^2})^2}{Hz}$ depending on frequency in the range of 2 Hz to 2000 Hz. The grey lines show the average PSD of measurements during travel flight, the red lines the maximum amplitude PSD during descent flight. As it is obvious in this diagram, the power density for descent flight is orders of magnitudes higher than for travel flight. By comparison the PSD measured with sensor 1 and sensor 3, the attenuation due to the mechanical damping of the aircraft mounting rack is obvious in the frequency range between 100 and 2000 Hz. Figure 4.21 shows the corresponding frequency and timing jitter measurement results using the heterodyne method.

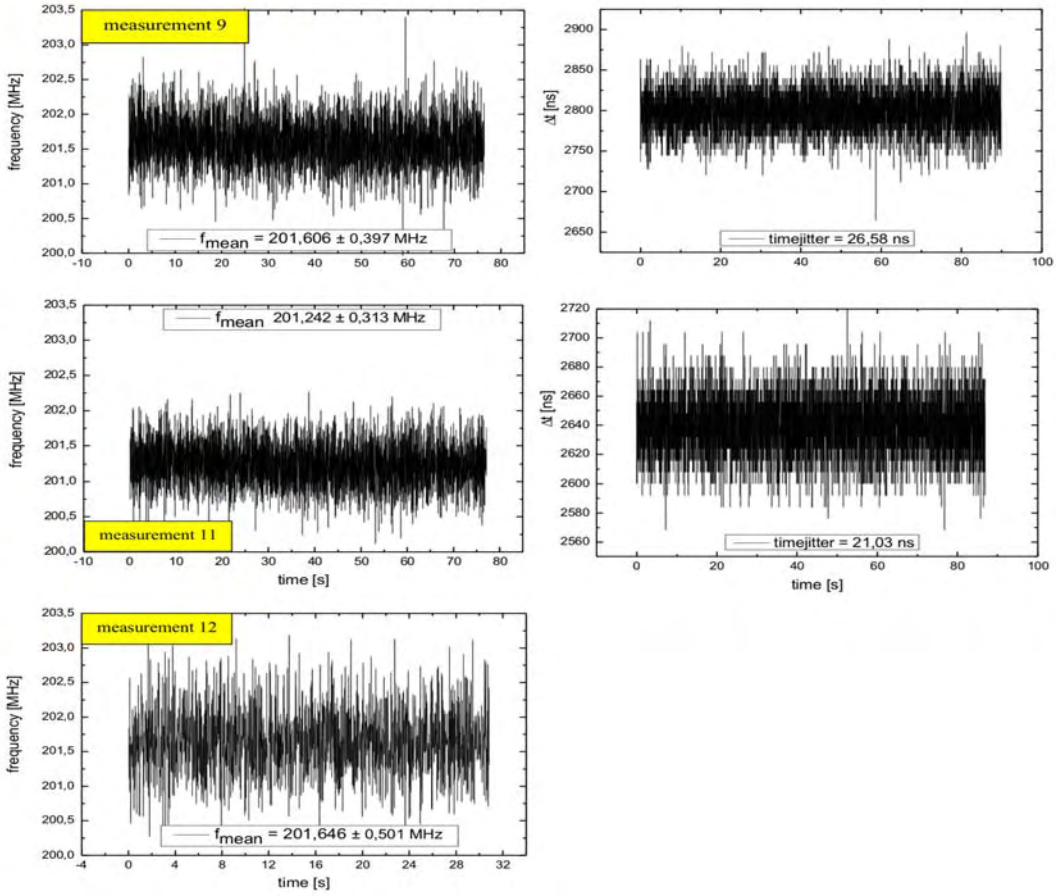

Figure 4.21: Heterodyne measurements of frequency (left) during travel flight (top, middle) and descent flight (bottom). Timing jitter measurements (resolution 8 ns) during travel flight are shown on the right.

The frequency stability requirement of 1,3 MHz was reached for travel flight (0,3 MHz - 0,4 MHz) as well as for descent flight (0,5 MHz). Despite the vibrational disturbance in descent flight of orders of magnitude higher than in travel flight, the laser was operating seeded all the time, and met the stability requirements concerning frequency and timing.

Flight Situation	Operation mode	Settings	Standard deviation of frequency [MHz]	Standard deviation of timing [ns]
Travel flight	RF	Dyn. = slow	0,170	18,73
		Dyn. = slow	0,156	17,70
		Dyn. = slow	0,143	35,30
		Dyn. = slow	0,202	21,95
		Dyn. = fast 3of 4883 shots unseeded ≈ 0,035 %	0,171	24,68
		Dyn. = slow	0,564	30,14
		Dyn. = slow	0,331	24,61
	RDF	-	0,274	20,97
		Dyn. = fast 33 of 3855 shots unseeded ≈ 0,86 %	0,397	26,58
		-	0,313	21,03
		Dyn. = slow 53 of 2570 shots unseeded ≈ 2,06 %	0,330	51,45
		Dyn. = fast 91 of 2570 shots unseeded ≈ 3,54 %	0,413	43,66
		Dyn. = fast 3of 2570 shots unseeded ≈ 0,12 %	0,250	17,86
		Dyn. = fast	0,260	20,57
		Dyn. = fast 3 of 7710 shots unseeded ≈ 0,039 %	0,452	32,57
		Dyn. = fast	0,254	18,87
Curve flight	RF	Dyn. = slow 1 of 2827 shots unseeded ≈ 0,035 %	0,212	42,04
		Dyn. = slow	0,311	411,66
		Dyn. = fast	0,292	28,43
	RDF	-	0,309	18,35
		Dyn. = fast 45 of 5911 shots unseeded ≈ 0,76 %	0,297	21,49
		-	0,288	20,07
Descent flight	RDF	Dyn. = fast 3 of 1542 shots unseeded ≈ 0,19 %	0,501	-

Table 4.3: Results of frequency measurements during flight.

In table 4.3 the results of all heterodyne measurements is shown. It turns out that the frequency stability is always smaller than 600 kHz, for travel flight as well as for curve flight, as well as for descent flight. This result is independent of cavity control settings and of operation mode (ramp fire - ramp delay fire). Also the timing jitter between expected and actual laser pulse emission meets the requirement. It is smaller than 50 ns in all cases, except measurements with the ramp and fire setting during curve flight

which leads to a timing jitter of 411 ns. The number of unseeded shots is below 3 % determined from heterodyne measurements, which could be also disturbed by vibrations for the coupling of the seedlaser and the LPO laser into the heterodyne unit.

Concluding it can be pointed out that the new active frequency control, based on the ramp fire technique, did work well compared to the earlier Q-switch build up time method. A significant difference between ramp and fire and ramp delay fire method, concerning to frequency and timing jitter was not observed. Also the different look-up table settings did not influence the results remarkably.

4.6 Frequency stability measurements during receiver calibration

During calibration, the laser frequency is changed in steps over a defined frequency interval and the signal detected with the Mie and Rayleigh receiver is recorded. This is used to calibrate the receiver response function. The response function for the two Rayleigh receiver filters is shown in figure 4.25.

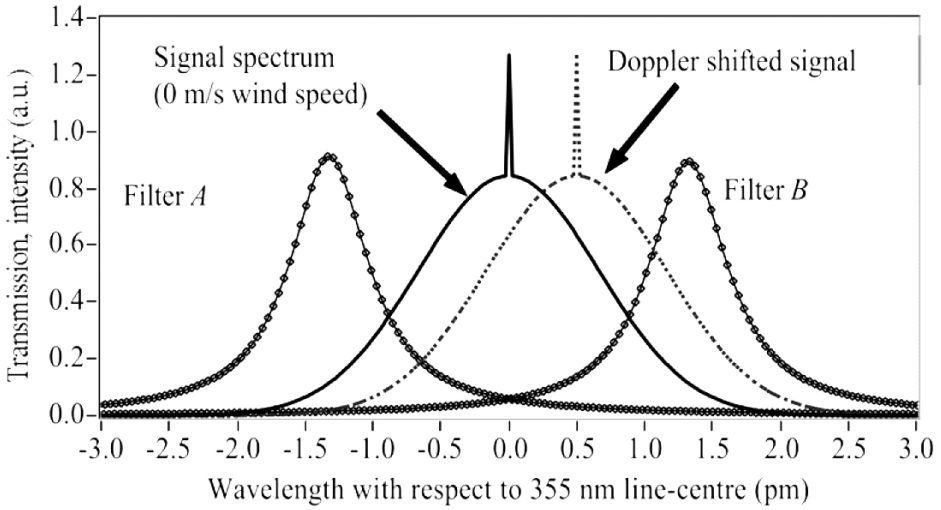

Figure 4.22: The transmission curves of Rayleigh interferom filter A and B, and the intensity distribution of the Mie and Rayleigh signal from a 355 nm source with respect to zero wind speed and to a Doppler-shifted signal versus wavelength [Paffrath 2006].

Wind measurements are performed at the frequency of the crosspoint of both filter curves. To get an approximate position of the cross point, the laser frequency is changed in 250 MHz steps over a range of 11 GHz to cover both filter transmission maxima. If this approximate position of the cross point is found, the frequency step resolution is increased to 24,9 MHz over a range of 1,8 GHz around the cross point. The frequency is changed every 700 laser pulses.

To characterise this process the output frequency (UV) of the A2D was measured during one calibration. The result of this frequency measurement is shown in figure 4.23.

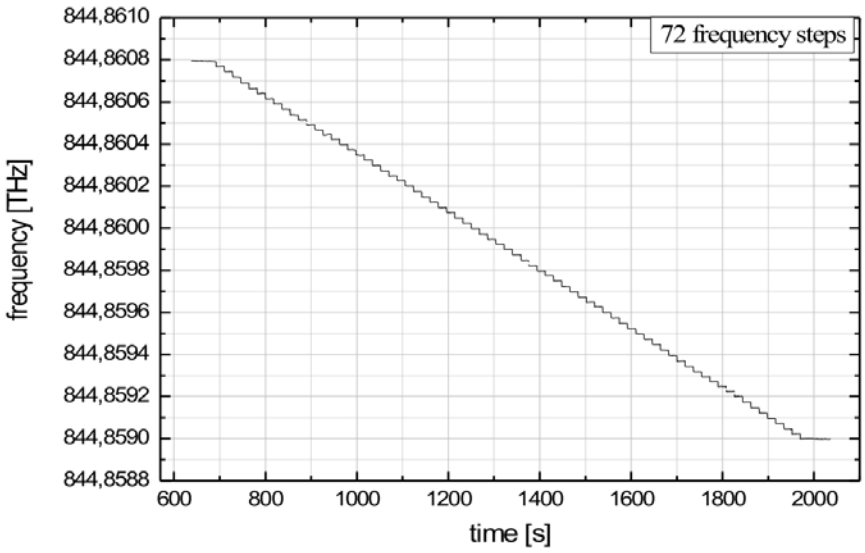

Figure 4.23: Frequency measured by the WLM versus time during the interferometer calibration. Laserfrequency is changed in 24,9 MHz steps every 18 s.

The frequency jitter for every frequency step is analysed, because it affects the accuracy of the calibration. Therefore, the respective frequency intervals were fractionized. So it was possible to calculate the frequency mean value of each step (700 shots) and its standard deviation (figure 4.24).

The mean value of frequency deviation is about **0,68 MHz (UV)**. So the requirement for frequency stability of 4 MHz (UV) is clearly met during the calibration. The histogram on the right side shows the distribution of the frequency standard deviation. With the calculated mean values of frequencies, the compliance of the frequency step size (24,9 MHz) can be verified. Therefore the frequency difference between the frequency mean values is calculated (figure 4.25).

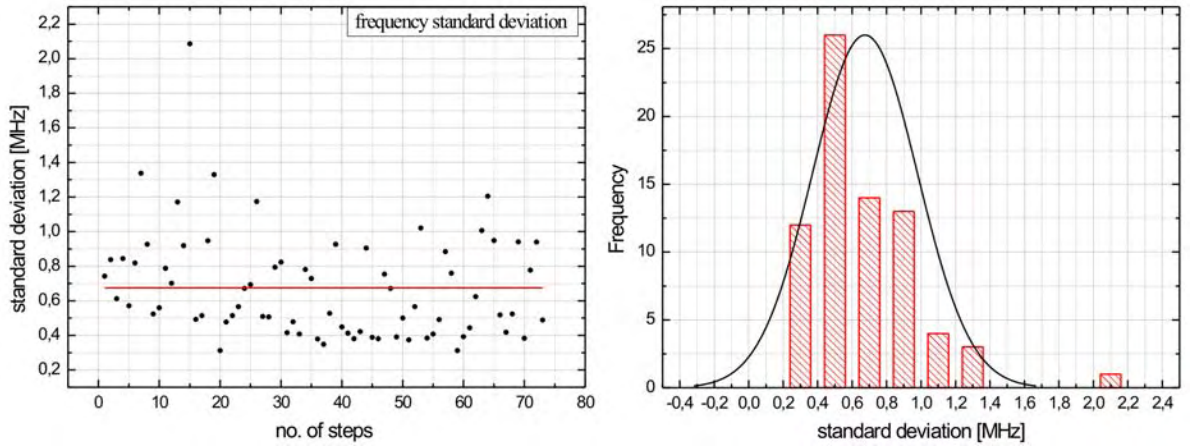

Figure 4.24: Standard deviation of frequency, for every single frequency step (left), and the corresponding histogram of standard deviation (right).

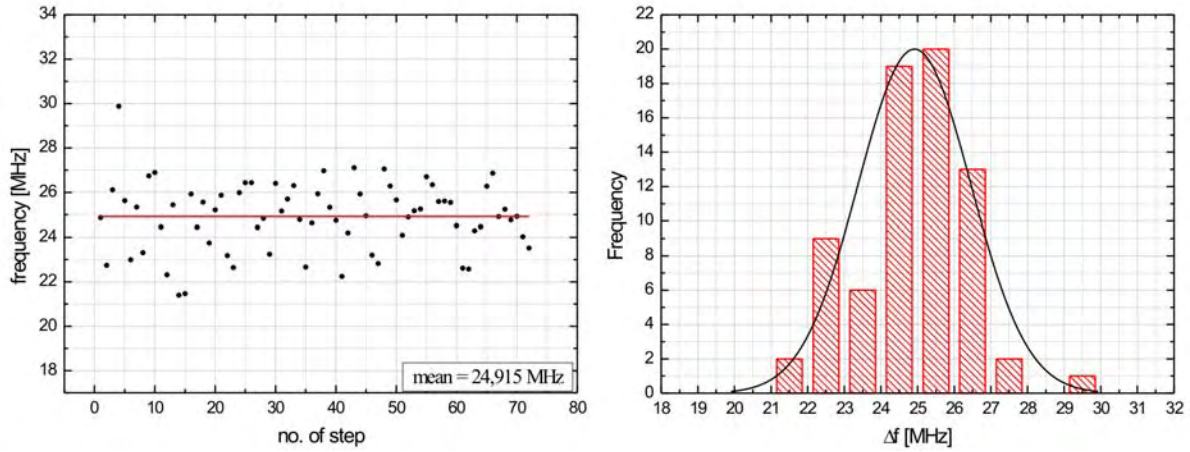

Figure 4.25: Difference between the mean frequency of every single step (left), and the corresponding histogram of the differences (right).

The mean value of one frequency step is **(24,915 ± 1,54) MHz**. Hence the frequency mean value differs only 15 kHz from the set value. The deviation of the interval steps is 1,54 MHz. With these measurements it was shown that the laser tunability complies with the requirements.

Chapter 5

Laser beam parameters

For accurate wind measurements with a Doppler wind lidar system the quality of the emitting laser beam is very crucial. An important parameter therefore is the divergence of the laser beam. The angular divergence of the transmitted beam determines if the beam is completely in the **field of view** (FOV) of the receiver. The FOV of the A2D receiver is fixed to a very small value of 100 μrad in order to reduce the solar background light in the Rayleigh receiver. The full divergence angle of the laser transmitter has to be smaller than the FOV for optimal lidar performance. Beam divergences in the range of 100 μrad are neither easy to achieve nor easy to measure. To get accurate information of the characteristic of the A2D laser beam two different divergence measurement methods and its results are discussed in this chapter.

In section 5.1 the propagation and characterisation of a Gaussian beam and non-Gaussian beams are discussed. Section 5.2 deals with beam diameter measurement using the knife-edge method. In section 5.3 beam characterisation with a converging lens in combination with an UV-camera is discussed.

5.1 Laser beam theory

5.1.1 Beam spatial profile

Before the propagation and characterisation of a Gaussian beam will be analysed in detail, the genesis of such a beam gets recapitulated.
A laser beam is the result of light amplification by stimulated emission of radiation (see chapter 4). An active laser medium, which is pumped by an external energy source, is placed in a resonant optical cavity. The process of generating laser radiation was discussed in more detail in chapter 4.
Essential for beam analysis is the transverse spatial distribution of energy within an optical resonator. In optical resonators only electromagnetic fields can exist whose distribution of amplitudes and phases reproduce themselves upon repeated reflections between the mirrors. This is a process of positive interference. These particular field configurations comprise **transverse electromagnetic modes** (TEM_{mn}) of a passive resonator. The integers of m and n represent the numbers of nodes and zeros of intensity transverse to the beam axis in the vertical and horizontal directions. Some examples of TEM patterns are shown in figure 5.1.

The mode with a special importance is the TEM_{00} mode, also called fundamental mode or Gaussian mode. One reason for this special importance is the minimum divergence angle θ and waist diameter d_0 of the TEM_{00} mode. Also the property that a Gaussian beam is reproduced in another Gaussian beam by non-aberrative optics makes it so peculiar. As the name suggests in TEM_{00} mode the beam emitted from the laser has an ideal Gaussian intensity profile. This intensity profile is given by the equation [e.g. Koechner 1988]

$$I(r) = I_0 \cdot exp(\frac{-8r^2}{d^2}) \tag{5.1}$$

in which I_0 is the intensity at the center, $r = \sqrt{x^2 + y^2}$ is the distance from the center,

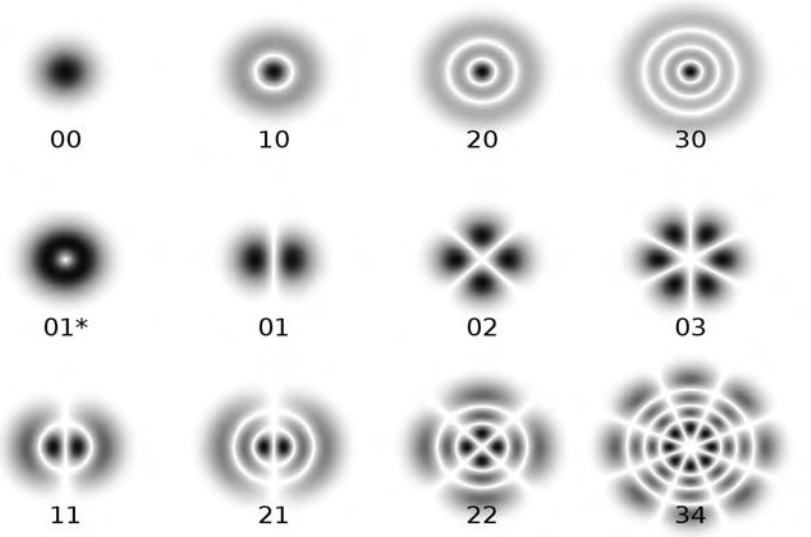

Figure 5.1: Examples of cylindrical transverse mode patterns. The first subscript indicates the number of colored rings, whereas the second subscript indicates the number of colored bars across the pattern. The modes marked with an *, are linear superposition of two like mode, one rotated 90° about the axis relative to the other [Koechner 1988].

and d is the beam diameter.

As the Gaussian beam does not have sharp edges, the limitation of such a beam has to be defined. For a Gaussian beam the beam radius is defined at the point where the intensity is down to $e^{-2} \approx 13,5\%$ of its intensity maximum. The intensity profile with the corresponding beam diameter is shown in figure 5.2.

For a non ideal Gaussian beam, the diameter is defined by the first and second order moments [ISO 11146]. The first order moment x, y gives the centroid of the beam. It is calculated similar in both, x and y directions with

$$\bar{x}(z) = \frac{\int\int x \cdot I(x,y,z) \cdot dxdy}{\int\int I(x,y,z) \cdot dxdy} \tag{5.2}$$

The second order moment ${\sigma_{x,y}}^2$ is called variance.

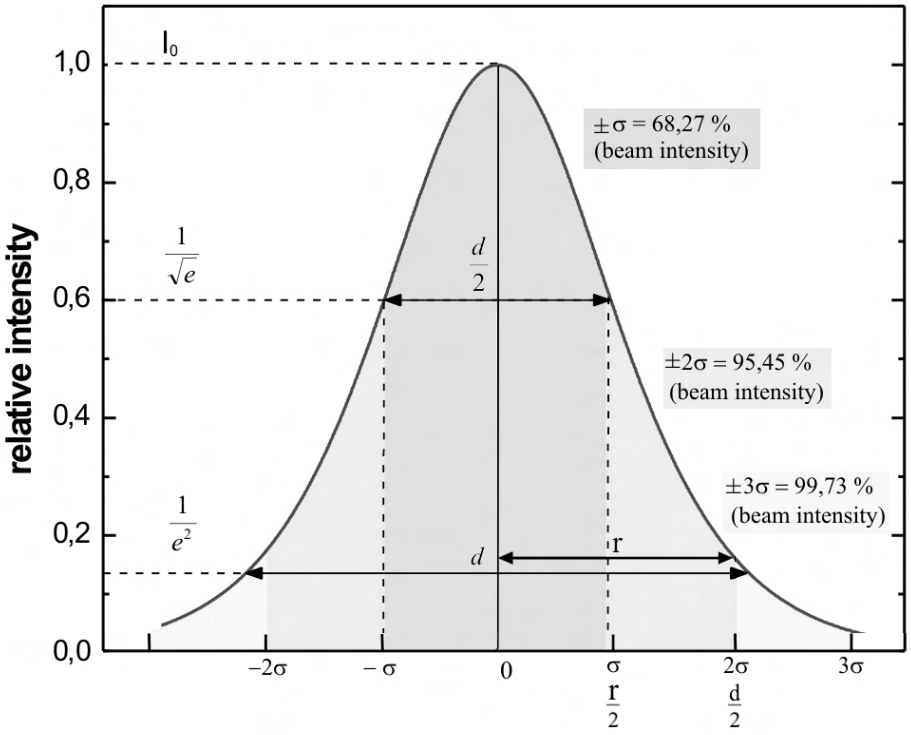

Figure 5.2: The intensity profile of a Gaussian beam. The distance from the position where the intensity reaches its maximum to the position where it is decreased to e^{-2} is defined as the beam radius r.

The variance is given by

$$\sigma_{x,y}{}^2(z) = \frac{\int\int r^2 \cdot I(x,y,z) \cdot dxdy}{\int\int I(x,y,z) \cdot dxdy} \tag{5.3}$$

where r is the distance to the centroid ($\bar{x}$,$\bar{y}$).

The square root of the variance is defined as the standard deviation σ. The interval between $\pm$ 2σ about the mean value includes 95,45 % of the complete beam intensity and is defined as the beam diameter d [ISO 11146]

$$d(z) = 4 \cdot \sigma_{x,y}(z) \tag{5.4}$$

Due to the A2D laser requirements the divergence angle in this thesis is always calculated with the 6 - σ - diameter. This is the interval where 99,73 % of the whole beam intensity is included.

5.1.2 Beam propagation and divergence

Gaussian Beam

If light waves propagate, diffraction causes them to spread transversally, and it is not possible in this case to obtain a perfectly collimated beam. The spreading of intensity of a Gaussian beam is in precise accordance with the predictions of pure diffraction theory [Bouwkamp 1954]. Thus, a Gaussian beam contracts to a minimum diameter $2 \cdot w_0$ at the beam waist where the phase front is planar. The spot size at a distance z from the beam waist $w_0 = \frac{d_0}{2}$ expands as a hyperbola, which is described by the following equation [e.g. Koechner 1988]

$$w(z) = w_0 \sqrt{1 + \left(\frac{\lambda \cdot z}{\pi \cdot {w_0}^2} \right)^2} \tag{5.5}$$

where z is the distance from the plane z_0 where the wavefront is flat, w_0 is the beam waist radius of the e^{-2} irradiance contour at the waist position z_0, and λ the wavelength. $w(z) = \frac{d(z)}{2}$ is the beam radius at any distance z from the waist (figure 5.3).
The asymptote of the hyperbola is inclined at an angle $\frac{\theta_G}{2}$ with the axis, as shown in figure 5.3, and defines the far-field divergence angle θ_G of the emerging beam. The full divergence angle for the TEM_{00} mode is given by

$$\theta_G = \lim_{z \to \infty} \frac{d(z)}{z} = \frac{4 \cdot \lambda}{\pi \cdot d_{0G}} \tag{5.6}$$

where d_{0G} is the diameter of a Gaussian beam at the waist position z_0.
At sufficiently large distances from the beam waist, the wave has a spherical wavefront

appearing to emanate from a point on the beam axis at the waist. The radius of curvature R(z) of the wavefront that intersects the axis at z is described by

$$R(z) = z \cdot \left[1 + \left(\frac{\pi \cdot {w_0}^2}{\lambda \cdot z}\right)^2\right] \tag{5.7}$$

Another parameter which is often used to characterise a laser beam is the Rayleigh length z_R. The Rayleigh length gives the position on the propagation axis, where the phase front curvature has a maximum value. Therefore the Rayleigh length is calculated by differentiation of equation 5.7

$$\frac{dR}{dz} = 0 \rightarrow z_R = \frac{\pi \cdot {w_0}^2}{\lambda} \tag{5.8}$$

Thus, the Rayleigh length is the position where the beam waist radius is increased by a factor of $\sqrt{2}$. The typical form of the Gaussian beam propagation with its beam diameter d_0 and the curvatures of the wave fronts $R(z)$ is shown in figure 5.3.

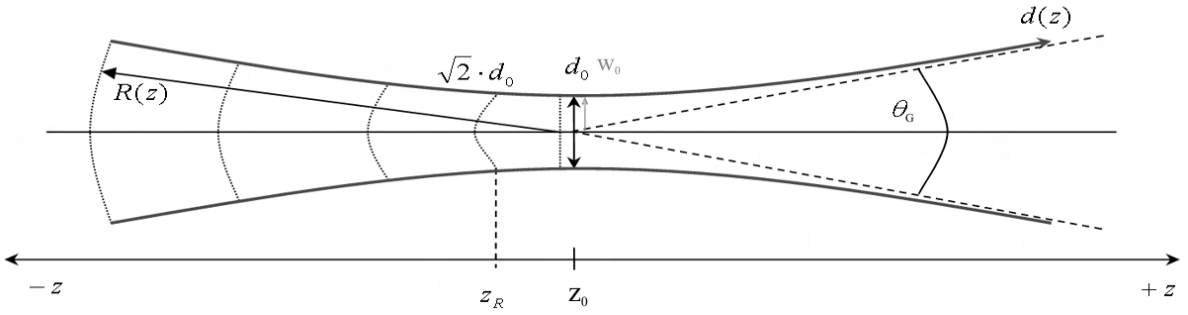

Figure 5.3: Gaussian beam propagation where d(z) shows the position of the intensity, where it is decreased to e^{-2} compared to the maximum on the propagation axis z, and d_0 is the waist diameter. On the left side of the waist, the curvature radius $R(z)$ is shown. It is plane at the waist and at infinity, and reaches its maximum one Rayleigh length z_R away from the waist. On the right side the divergence angle θ_G with the hyperbola asymptotes are shown. z_0 is the waist position along the propagation axis z.

Non Gaussian beam

Most real laser beams show a deviation of the ideal Gaussian profile. Reasons therefore can be the excitation of higher transverse modes in the optical resonator, the inhomogeneous amplitude and phase amplification of the laser medium, or interference with splitted beams. These real laser beams show a higher divergence and a larger focus diameter after focussing with a lens.
The usual way to compare a real laser beam with the ideal Gaussian one is to determine the beam-propagation factor M^2 [ISO 11146]. For higher transverse modes or mode mixtures both the waist diameter d_0 and the divergence θ are higher than for Gaussian beams by a factor M [Roundy 1999, Roundy 2000]. The relation between a real beam and an ideal Gaussian beam is shown in figure 5.4.

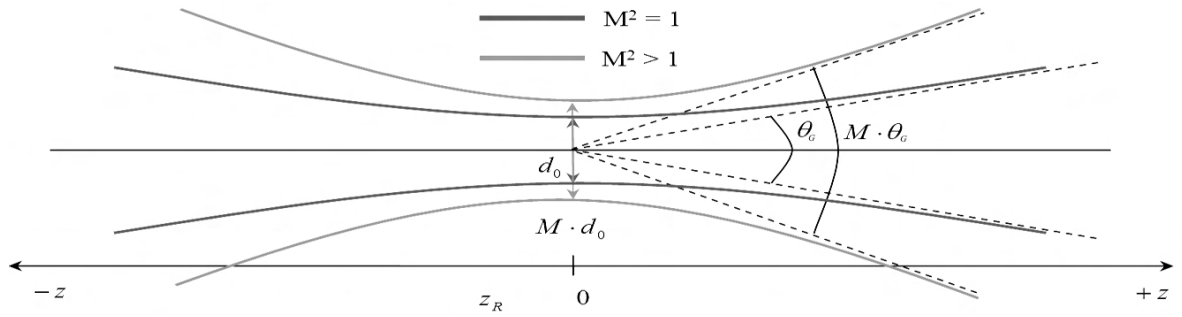

Figure 5.4: Beam waist diameter d(z) and full divergence angle of a real beam $M \cdot \theta_G$. Both are a factor M larger than Gaussian beam parameters. M^2 is the times-diffraction limit factor.

Hence, Equation (5.6) gets modified for real laser beams with the factor M^2 giving

$$\theta \cdot d_0 = M^2 \cdot \frac{4 \cdot \lambda}{\pi} = M^2 \cdot \theta_G \cdot d_{0_G} \tag{5.9}$$

where θ is the full divergence angle, d_0 the beam waist diameter of a non Gaussian beam. M^2 is called the times-diffraction-limit factor.
The product of θ and d_0 is called the **beam parameter product** (BPP), and is used

to specify the quality of a laser beam. Significant to mention is that the BPP does not change when the beam is sent through non-aberrative optics. If the lens generates a focus with smaller beam waist diameter, the beam divergence will correspondingly increase. So the relation

$$\theta \cdot d_0 = \theta_f \cdot d_{0_f} \tag{5.10}$$

can be written, where $\theta \cdot d_0$ is the BPP of the emanated beam and $\theta_f \cdot d_{0_f}$ this of the focused one. This property is used for laser beam characterisation as described in section 5.3.

5.2 Methods for beam divergence characterisation

The following subsections discribe two different methods to determine the beam divergence and discuss their results.

5.2.1 Knife-edge method

For divergence measurement respectively diameter measurement using the knife-edge method, the propagating beam is cut via an edge. The transmitted power is measured with a powermeter depending on the edge position. In figure 5.5 the transmission curve measured while cutting the beam in one axis is shown, assuming a Gaussian intensity profile.

The transmission $T(x)$ of a Gaussian beam depending on the edge position x can be calculated with [e.g. Eichler et al. 2004]

$$T(x) = \frac{1}{P} \int_{x}^{\infty} \int_{-\infty}^{\infty} I(x,y) \cdot dxdy = \frac{1}{2} \left(\mathrm{erf}\left(2\sqrt{2} \frac{x}{d} \right) + 1 \right) \tag{5.11}$$

where $I(x,y)$ is the intensity on the respective position, P the laser power, d the beam diameter and *erf* the error function.
To obtain the beam radius r it is necessary to measure the transmission at the egde position of $\pm \frac{d}{4}$, because the difference between $\pm \frac{d}{4}$ is equal to 2 σ, which defines the beam radius. This value can be calculated with equation (5.11) and table 5.1 where values of the numerical solution of the error function are listed.

It follows that the transmitted power at 16 % and 84 % yields the value which includes the beam radius. If the beam radius gets measured on different positions of the propagation axis, the spreading of the diameter and therefore the full divergence of the beam

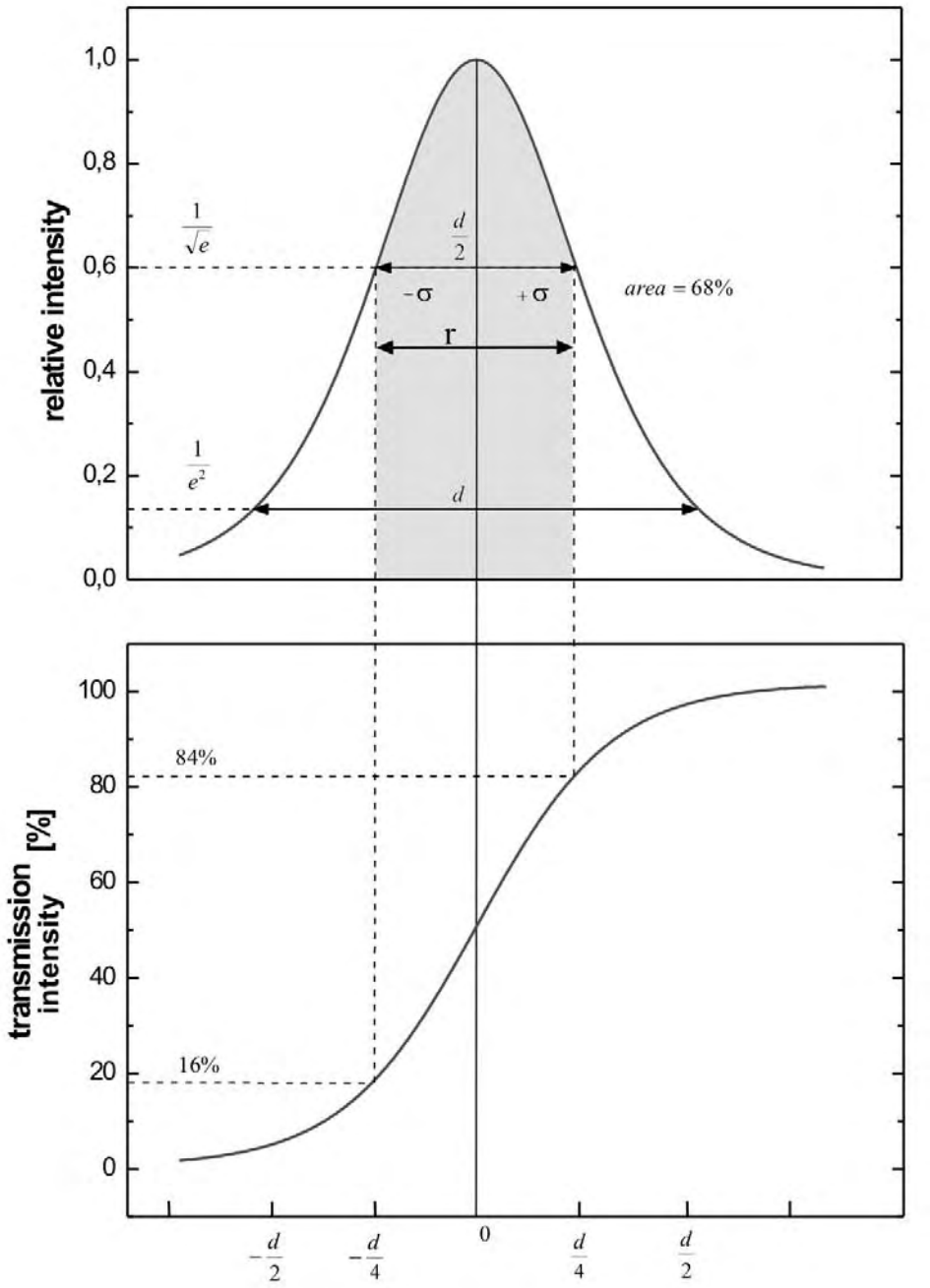

Figure 5.5: Determination of the beam diameter with the knife-edge method. Above: Intensity profile of a Gaussian beam. Below: Transmission depending on the edge position. The beam radius is defined as the distance between the value of 16 % and 84 % transmission [adapted from Eichler et al. 2004].

x	erf(x)	x	erf(x)	x	erf(x)
0,00	0,0000000	0,45	0,4754817	0,90	0,7969082
0,05	0,0563720	0,50	0,5204999	0,95	0,8208908
0,10	0,1124629	0,55	0,5633234	1,0	0,8427008
0,15	0,1679960	0,60	0,6038561	1,1	0,8802051
0,20	0,2227026	0,65	0,6420293	1,2	0,9103140
0,25	0,2763264	**0,70**	**0,6778012**	1,3	0,9340079
0,30	0,3286268	0,75	0,7111556	1,4	0,9522851
0,35	0,3793821	0,80	0,7421010	1,5	0,9661051
0,40	0,4283924	0,85	0,7706681	1,6	0,9763484

Table 5.1: Numerical solution of the error function *erf* [Abramowitz and Stegun 1972]. To obtain the beam width from the measured transmitted power, equation (5.11) has to be solved for $x = \pm\frac{d}{4}$. Therefore, the bold printed value, and the relation $erf(-x) = -erf(x)$ is used.

can be calculated according to:

$$\theta = \frac{d_2 - d_1}{\Delta z} \tag{5.12}$$

where d_2 and d_1 are the diameters at different positions with distance Δz.

To arrange this measurement the A2D laser transmitter was set up in a container without telescope and receiver. An aluminium was mounted on a micrometer drive to cut the beam. Because of an expected divergence of around 100 μrad the edge length was chosen to 5 cm. With this size it ensured that in 100 m distance from the container 99,5 % of the beam intensity gets cut from the plate.
The moving plate was placed in front of a thermal sensor (PM 150 - 19C, coherent) which was linked to a powermeter (Field Max - TO, coherent). A schematic diagram of the measurement setup is shown in figure 5.6.

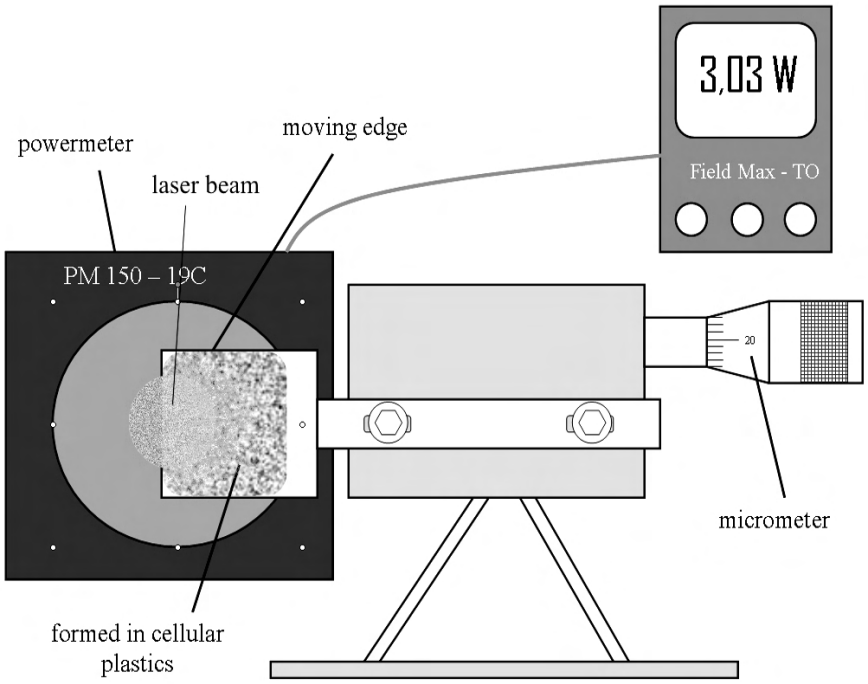

Figure 5.6: Setup of divergence measurement with the knife-edge method. The laser beam gets cut with an edge. The transmitted power, measured with the powermeter, provides information of the beam diameter.

The diameter measurements were done in 1,26 m, 37,18 m and 77,68 m distance from the laser **beam expander** (BEX) output. At about 300 power measurements per edge position were used to build the mean value of one power measurement with its standard deviation. The mean value, error bars of the measurements and the resultant beam diameters at different positions of the z-axis are shown in figure 5.7.

In figure 5.7, the transmission curves measured in 1,26 m (top, left), 37,18 m (top, right), and 77,68 m (bottom, left) and the respective resulting 4-σ and 6-σ-diameters are shown. The diagram on the lower right side shows the 4-σ diameter propagation in z-axis. From this diagram it is obvious that the beam diameter decreases along the propagation axis until about 40 m, before it increases. This matter of fact does not agree with the theoretical expected propagation of a divergent laser beam, but can be explained with a wrong BEX alignment.

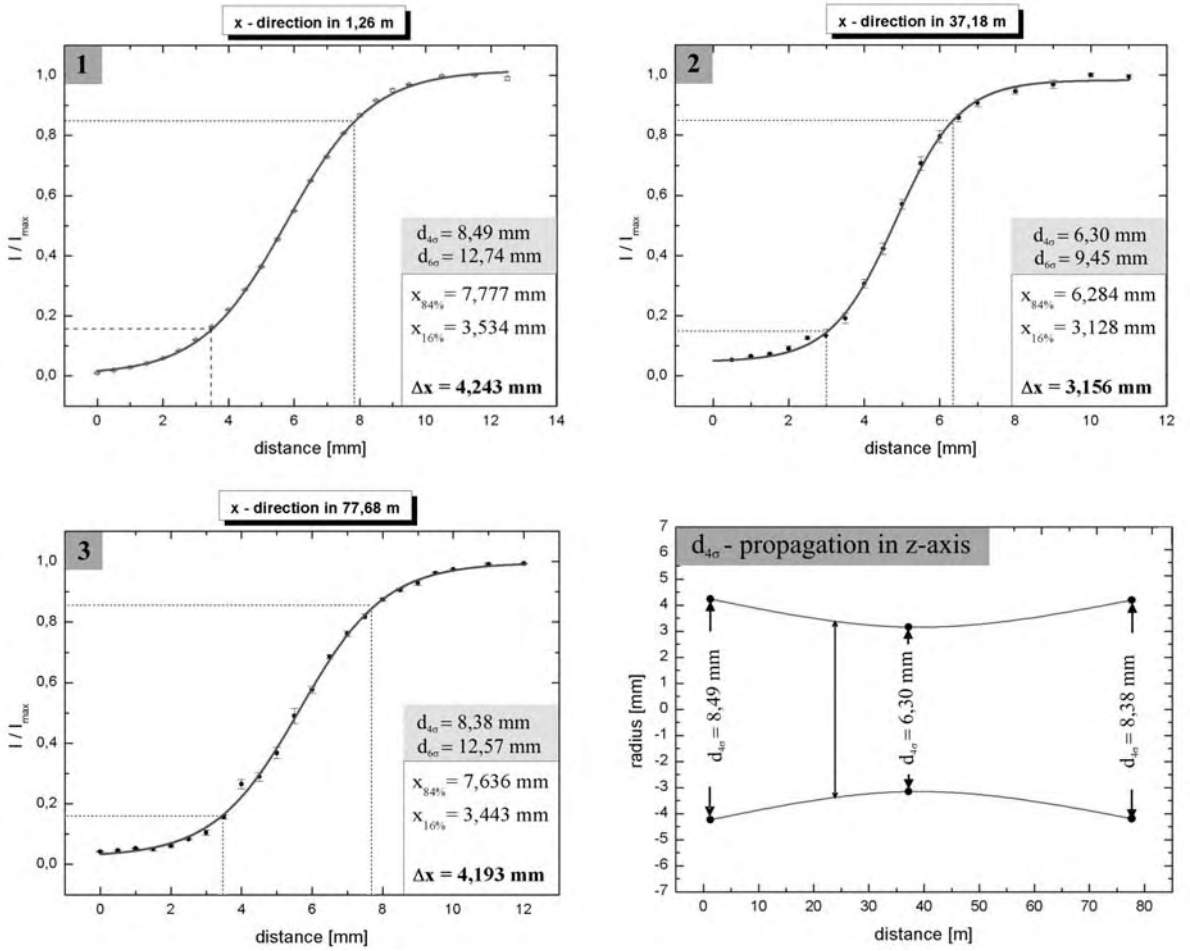

Figure 5.7: Power transmission depending on the edge position in the distances of 1,26 m (top, left), 37,18 m (top, right), and 77,68 m (bottom, left). The 4-σ diameter along the propagation axis z is shown in the right, bottom diagram.

For beam expansion at the laser output, a Galilean beam expander, consisting of a negative input lens and a positive objective is used. A sketch of the beam expander is shown in figure 5.8.

If the distance between both lenses is too large, the outcoming beam will propagate convergent first. By means of the performed measurement the waist diameter would be close to 40 m.

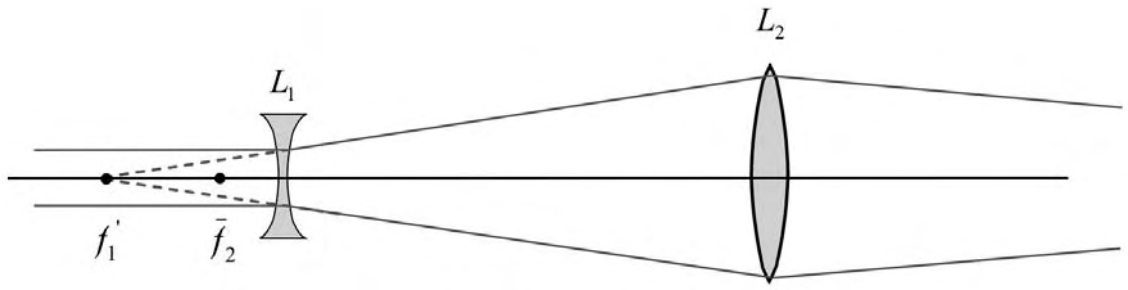

Figure 5.8: Galilean BEX with 2 lenses L_1, L_2 and its focal points f_1, f_2 in a configuration, where the distance of the lenses is too large.

The full divergence angle is calculated with (5.12), $d_2 = 12,57$ mm, $d_1 = 9,45$ mm, and $\Delta z = 40,5$ m (figure 5.7) and yields an angle of 76,8 μrad (6-σ). The diffraction limited divergence angle for a Gaussian beam with a waist diameter of 6,3 mm is calculated with equation (5.9) to be 107 μrad (6-σ). Since the diffraction limited divergence angle is the minimum possible value, the result of the knife-edge measurement is not consistent with the theory.

One explanation for this inconsistency can be an insufficient accuracy of beam width measurement because of the sensibility of the used thermal sensor for power measurement. The power sensor absorbs the incident laser radiation and converts it into heat. The temperature between the absorbing area and an air cooled reference area is measured, and gives a value which is proportional to the power of the incident laser radiation. If the ratio between both areas is disturbed by temperature changes (like wind fluctuations during field measurements) or other external influences, the accuracy of power measurement, thus diameter determination will decrease. For beam width measurement at 37,18 m and 77,68 m the complete measurement setup inclusive thermal sensor were exposed to outside influences like wind, solar radiation and temperature fluctuations. These effects disturbed the temperature difference between absorber and heat sink and therefore yield to a random error which could be a reason for an inaccurate measurement result. Since the data points in figure 5.7 are a result of averaging 300 measurements, and due to the of the data points with the expected error-function the described error is not significant.

Another issue which could lead to errors in the knife-edge measurement is the beam profile of the emanating beam. Figure 5.9 shows the intensity profile measured with an UV camera. It is obvious that the beam profile is not radial symmetric but has an elliptic shape. If an elliptic beam first propagates convergent, the ellipse will rotate due to the higher divergence of the major axis. If now the edge cuts the beam in an arbitrary axis, the resulting measurement is not along the major axis. The ratio between major and minor axis is about 1:1,30. So the half angle divergence between major and minor axis will differ 15 % at the most. Therefore the ellipticity of the beam can not fully explain the inconsistence between measured divergence and diffraction limited divergence.

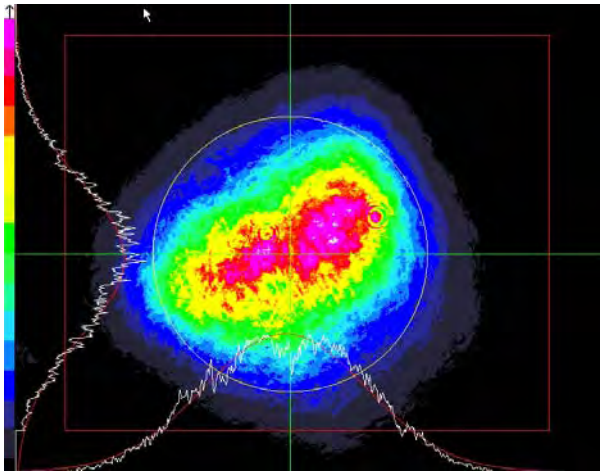

Figure 5.9: Intensity profile of the emanated beam, recorded with an UV camera.

It turned out that the large Rayleigh length of the emanating beam has lead to a wrong divergence result. To calculate the far field divergence angle with (5.12) it is necessary that both d_2 and d_1 are some Rayleigh lengths away from the laser output (figure 5.10), because equation (5.12) assumes a linear diameter increase for divergence calculation. The Rayleigh length from equation (5.8), with $\lambda = 355$ nm and $d_0 = 6,3$ mm results in $z_R = 44$ m. Due to the waist at around 40 m, the diameter measured in 77,68 m is only about one Rayleigh length away from the waist and therefore not useful for divergence

calculation. Diameter measurements in larger distances were not possible due to the limited powermeter aperture size.

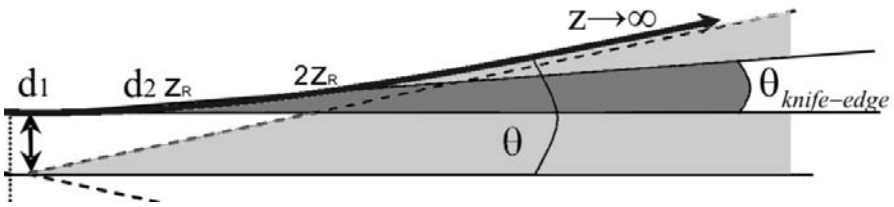

Figure 5.10: The dark grey area shows the divergence angle $\theta_{knife-edge}$ which is calculated with equation (5.12), where the diameters are $d_2 \approx d(z_R)$ and $d_1 \approx d(z_0)$. Due to the long Rayleigh length of the laser beam, the assumption of linear diameter increasing leads to an error. For comparison, the actual divergence angle θ is indicated with the light grey area.

To obtain an approximate value of the divergence angle, equation (5.5) was used for a statistical curve fit through the 3 measured diameters. With this hyperbola fit the waist diameter d_0, the Rayleigh length z_R and the waist location z_0 can be determined, and therefore a calculation of the divergence angle θ and the times-diffraction limit factor M^2 was possible. A detailed explanation of this calculation is given in next subsection 5.2.2. The three measured diameters along the beam axis position including the hyperbola are shown in figure 5.11.

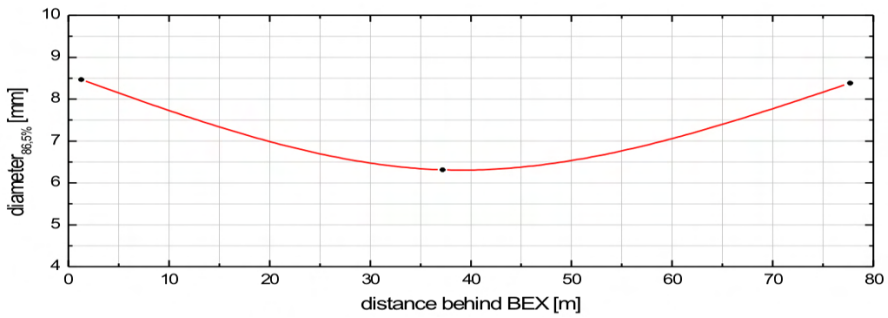

Figure 5.11: Diameters of the laser beam along the propagation axis from the knife-edge method and equation (5.5), and the resulting hyperbola curve.

For d_0 = 6,3 mm and z_R = 44,0 m, the M^2 value is calculated to 2,04 and the full divergence angle to be 219 μrad.

Summarized it can be shown that the knife-edge measurement method has some limitations which can not be eliminated. Nevertheless, with the non-linear curve fit it was possible to get a first estimate of the beam parameters M^2 and θ. To verify these results, a second divergence measurement method is discussed in the following section.

5.2.2 Lens method

In comparison to the knife-edge method the beam width measurement with a UV camera is a more comfortable method and yields to more accurate values. Also the determination of the second moment diameter is much easier, due to accumulation of the intensities of every single pixel by the UV camera software.
Because of the limited active area size of the camera chip the laser beam can not be completely acquired without a focussing lens. If the given input beam with a width D will be focussed by a lens, the diameters of the focussed beam can be measured some Rayleigh lengths in front and behind the beam waist and therefore also the divergence of the focussed beam can be determined. The typical setup of a diameter measurement with an UV camera is shown in figure 5.12.

If the diameter of the focused beam is measured on different positions along the propagation axis z, the waist diameter d_0, the waist position z_{f0}, and the Rayleigh length z_{fR} can directly be determined by a hyperbolic curve fit according to equation (5.5), and using equation (5.6) for θ_f. For accurate fit results, at least 10 diameter measurements within one Rayleigh length, and 10 beyond were done.
To obtain the divergence angle of the focussed beam θ_f, and the times-diffraction-limit factor M^2, the square of the measured diameters is calculated and fitted with the square of equation 5.5 [ISO 11146].

$$d^2(z) = {d_0}^2 + (z - z_{f0})^2 \cdot {\theta_f}^2 \tag{5.13}$$

$$d^2(z) = A + B \cdot z + C \cdot z^2 \tag{5.14}$$

The coefficients A, B and C of the parabola $d^2(z) = A + B \cdot z + C \cdot z^2$ are determined by curve fitting, and θ_f can be calculated using

$$\theta_f = \sqrt{C} \tag{5.15}$$

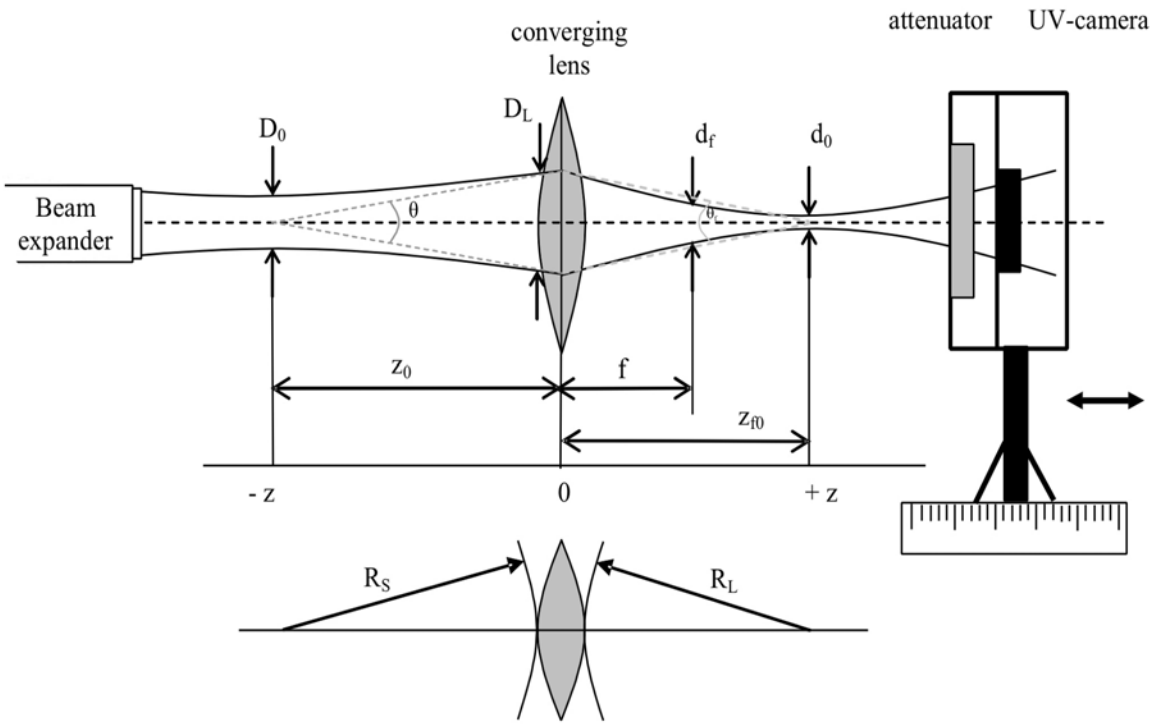

Figure 5.12: Setup for beam characterisation with a UV camera and a converging lens. The orientation of the radius of curvature R_s of the emanating beam and R_L of the focussed beam is shown at the bottom.

To determine the beam width D_L at the lens position, equation 5.13 has to be solved for $z = 0$ giving

$$D_L = \sqrt{A} \tag{5.16}$$

The times-diffraction-limit factor M^2 is described by $M^2 = \frac{\theta \cdot d_0}{\theta_G \cdot d_G}$ (eq. 5.9). The BPP of the focussed beam can be calculated using $\theta_f \cdot d_f = \sqrt{A \cdot C - \frac{B^2}{4}}$, and the BPP of the ideal Gaussian beam is given by $\theta_G \cdot d_G = \frac{4 \cdot \lambda}{\pi}$ (eq. 5.6). Thus, M^2 is determined according to

$$M^2 = \frac{\pi \cdot \sqrt{A \cdot C \ - \frac{B^2}{4}}}{4 \cdot \lambda} \tag{5.17}$$

To accurately determine the angular beam divergence θ, the waist diameter of the emanating beam D_0 is needed. This is done by "retransforming" the radius of curvature of the focussed beam.
The radius of curvature on the measurement side of the lens (right of the lens in figure 5.12) can be calculated according equation (5.7)

$$R_L = z_{f0}\left[1 + \left(\frac{z_{fR}}{z_{f0}}\right)^2\right] \tag{5.18}$$

where z_{fR} is the Rayleigh length of the focussed beam.

This radius of curvature is changed while it was passing the lens. The radius of curvature on the source side of the lens can be calculated according to [e.g. Wright et al. 1992, Sasnett et al. 1989]

$$R_S = \frac{1}{\frac{1}{f} - \frac{1}{R_L}} \tag{5.19}$$

Using R_s, the beam width minimum D_0 on the source side of the lens can be calculated with [e.g. Wright et al. 1992]

$$D_0 = \frac{D_L}{\sqrt{\left[1 + \left(\frac{\pi \cdot {D_L}^2}{4 \cdot \lambda \cdot M^2 \cdot R_S}\right)^2\right]}} \tag{5.20}$$

The waist location z_0 is determined with [e.g. Wright et al. 1992, Kogelnik 1966]

$$z_0 = \frac{R_S}{\left[1 + \left(\frac{4 \cdot \lambda \cdot M^2 \cdot R_S}{\pi \cdot {D_L}^2}\right)^2\right]} \tag{5.21}$$

For diameter measurement with a setup shown in figure 5.12, the LaserCam - HR (Coherent) was used. The active area of the **complementary metal oxide semiconductor**

(CMOS) of this camera is 6,8 x 8,5 mm and comprises 1024 x 1280 pixels. For accurate diameter calculation a minimum of 30 digital pixels are required according to the manufacturer. Hence, it is necessary to choose an appropriate converging lens for an accurate diameter determination.

The size of the focus diameter d_{0f} can be approximated with [e.g. Siegman 1986]

$$d_{0f} \approx \frac{2 \cdot f \cdot \lambda}{D_L} \tag{5.22}$$

which should be at least 6,7 μm·30 = 0,201 mm. For λ = 355 nm and the diameter D_L in the position of the lens of approximately 8 mm (taken from figure 5.7, measured in 1,26 m), a focal length f of 2,25 m is required. This calculation assumes an ideal Gaussian beam. Since a real beam creates a larger waist diameter than the ideal one, a 2 m converging lens will be sufficient. In the following measurements both, a 2 m and a 3 m converging lens were used.
Because of the UV radiation, the lenses are made of fused silica (leading to high transmission) and have a surface figure of $\frac{\lambda}{10}$. The focal length tolerance of both lenses is ± 0,5 % [Appendix A.4, Laser Components].

To reduce the laser power density at the surface of the detector, some attenuation devices are used in this measurement setup. In the laser system itself a half-wave plate ($\frac{\lambda}{2}$) in combination with a polariser is applied to reduce the exiting laser power from 3,2 W to 30 mW. To realize a variable attenuation for matching the beam intensity for the different diameters to the CMOS saturation, a UV attenuator (Type C-VARM from Coherent) is used. This attenuator consists of two wedge attenuators. One which is continuously variable and one which allows stepwise attenuation from 10^7 : 1 down to 3000 : 1. The third way of attenuation is caused by two tilted mirrors which navigate the beam around the optical bench in a way that the beam waist of the focused beam is at the position of the UV-camera. On these devices 4 % of the incident beam power is

reflected. With these three attenuation devices it is possible to adjust the laser power to be lower than the camera power saturation. The material of the attenuation optics is properly specified and polished so that the beam is not distorted by the introduction of the attenuation.
To realize sufficiently large distances along the z-axis for enough diameter measurements, the UV-camera was mounted on a 2 m long rail.

Results

One example of the diameter measurement using the UV-camera is shown in figure 5.13. The beam width is calculated with the method of the second moments by the UV camera software for the major and the minor axis of the beam. The beam width is an average of 50 measurements and the error bars show the standard deviation. The result of beam parameter calculation in comparison with the knife-edge method is shown is Table 5.2.

	UV-camera (major axis)	UV-camera (minor axis)		knife-edge (x axis)
M^2	1,87 ± 0,22	1,74 ± 0,20		2,04
D_0 [mm]	6,56 ± 0,57	5,61 ± 0,61		6,299
D_L [mm]	8,49 ± 0,23	7,37 ± 0,38		8,48
Z_0 [m]	42,0 ± 6,0	33,7 ± 3,6		39,89
$\theta_{6\sigma}$ [μrad]	193 ± 21	210 ± 15		219

Table 5.2: Result of the beam parameter measurement with the lens and the UV camera (major, minor axis with mean ± 1 σ) and the knife-edge measurement (x-axis), for times-diffraction-limit factor M^2, waist diameter of the original beam D_0, the beam diameter at lens position D_L, the beam waist position of the original beam Z_0, and the 6σ value of the beam divergence $\theta_{6\sigma}$.

The mean values and their standard deviation, shown in table 4.2, are calculated from 8 different divergence measurements (4 times with f = 2 m lens and f = 3 m lens each).

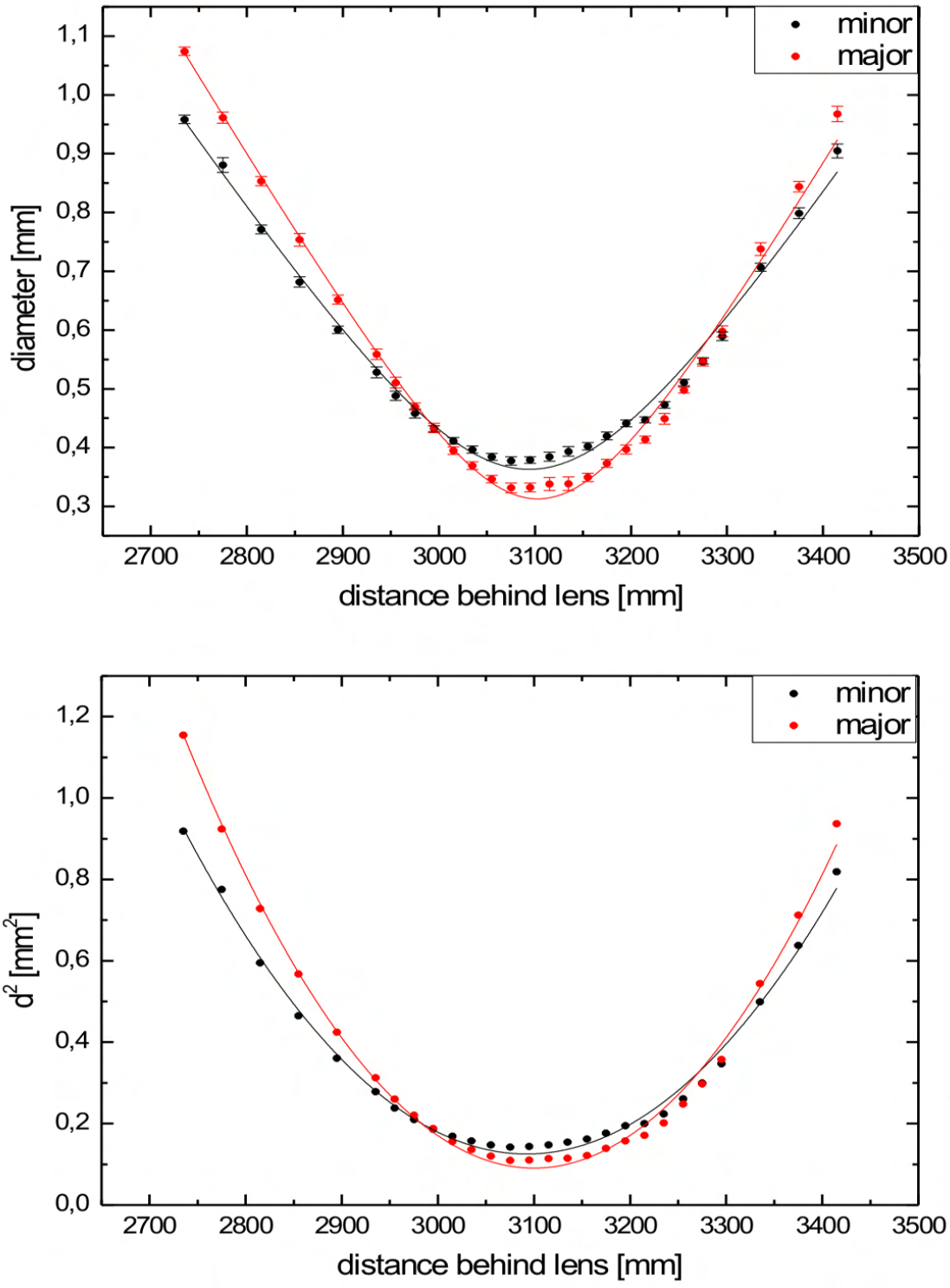

Figure 5.13: Measurement with a f = 3 m converging lens. The beam diameter depending on the position behind the lens, including the hyperbola curve fit (top), and the square of the diameters including the parabola fit (bottom) is shown for minor axis (black), and major axis (red).

The accuracy and also the repeat accuracy of this measurement method is in a range of 10 %.
The results of the UV camera measurement are very consisting with the knife-edge measurement results. This is obvious for all measured parameters. Also the waist location at about 40 m can be confirmed. The measured divergence in both axes is about 200 μrad ($6\sigma = 99{,}7$ %), and therefore it is more than two times larger than the receiver FOV.

One way to reduce the laser divergence and to eliminate the waist at 40 m is an optimisation of the position of the BEX lenses. If the waist of the emanating beam is aligned at infinity, the waist diameter would be as large as the diameter at the lens position, and therefore the divergence will be smaller. Another way to magnify the beam diameter is to use a BEX with a larger magnification. Both options were realized within this thesis and are described in the next section.

5.3 Optimisation of laser beam parameters

To realize a laser beam which is completely in the FOV of the telescope (100 μrad) the two lenses of the BEX are changed with lenses of different focal length. With this modification it was possible to change the magnification of the beam diameter from 4 to 5. A higher magnification was not feasible due to the limited BEX diameter of 1 inch. If the diameter of the beam is larger than 50 % of the BEX lens diameter, diffraction effects will not be negligible.
After exchanging the lenses it was necessary to optimize the distance between the 2 BEX lenses. To realize this, the measurement setup described in 5.2.2 was used. The emanating beam was focussed with a f = 2 m converging lens, and the UV camera was placed exactly one focal length away from the lens (2164 mm @ 355 nm). If now the distance between the lenses of the BEX gets changed in a way that the beam waist is exactly positioned in the focus of the converging lens, the alignment will be perfect.
Due to the different waist positions for major and minor axis, not the beam diameter

was chosen to find the focus of the beam, but the power density which hits the CMOS. Thus, the BEX was aligned in a way that the spot onto the CMOS chip creates the highest power density. For an ideal transformed Gaussian beam, this point would be the beam waist.

After this alignment, the measurement procedure described in 5.2.2 was repeated. The result of this measurement is shown in figure 5.14 and table 5.3.

	UV-camera	UV-camera
	(major axis)	(minor axis)
M^2	1,21	1,14
D_0 [mm]	11,09	7,94
D_L [mm]	11,25	9,80
Z_0 [m]	38,5	88,7
$\theta_{6\sigma}$ [μrad]	74	97

Table 5.3: Results of divergence measurements after BEX modification, for times-diffraction-limit factor M^2, waist diameter of the original beam D_0, the beam diameter at lens position D_L, the beam waist position of the original beam Z_0, and the 6σ value of the beam divergence $\theta_{6\sigma}$.

As expected from the modification of the BEX, the beam diameter in both axes is at a factor of $\frac{4}{5}$ larger than before. However, the waist diameter D_0 is only slightly smaller (for major axis), and about 10 % smaller (for minor axis) than the beam diameter at the lens position. This fact is an indication for a nearly collimated propagating beam. The difference of waist diameter for major and minor axis is due to the effect of astigmatism which can not be removed.

The remarkable improvement of M^2 is not explained with the new BEX. The M^2 is a ratio between ideal and real BPP, and the BPP is not depending on transformations between lenses. The reason for the improvement of the M^2 is the adjustment of the IR path of the laser. Clipping effects on the power amplifier crystals led to diffraction effects which increased the beam waist diameter, and therefore M^2.

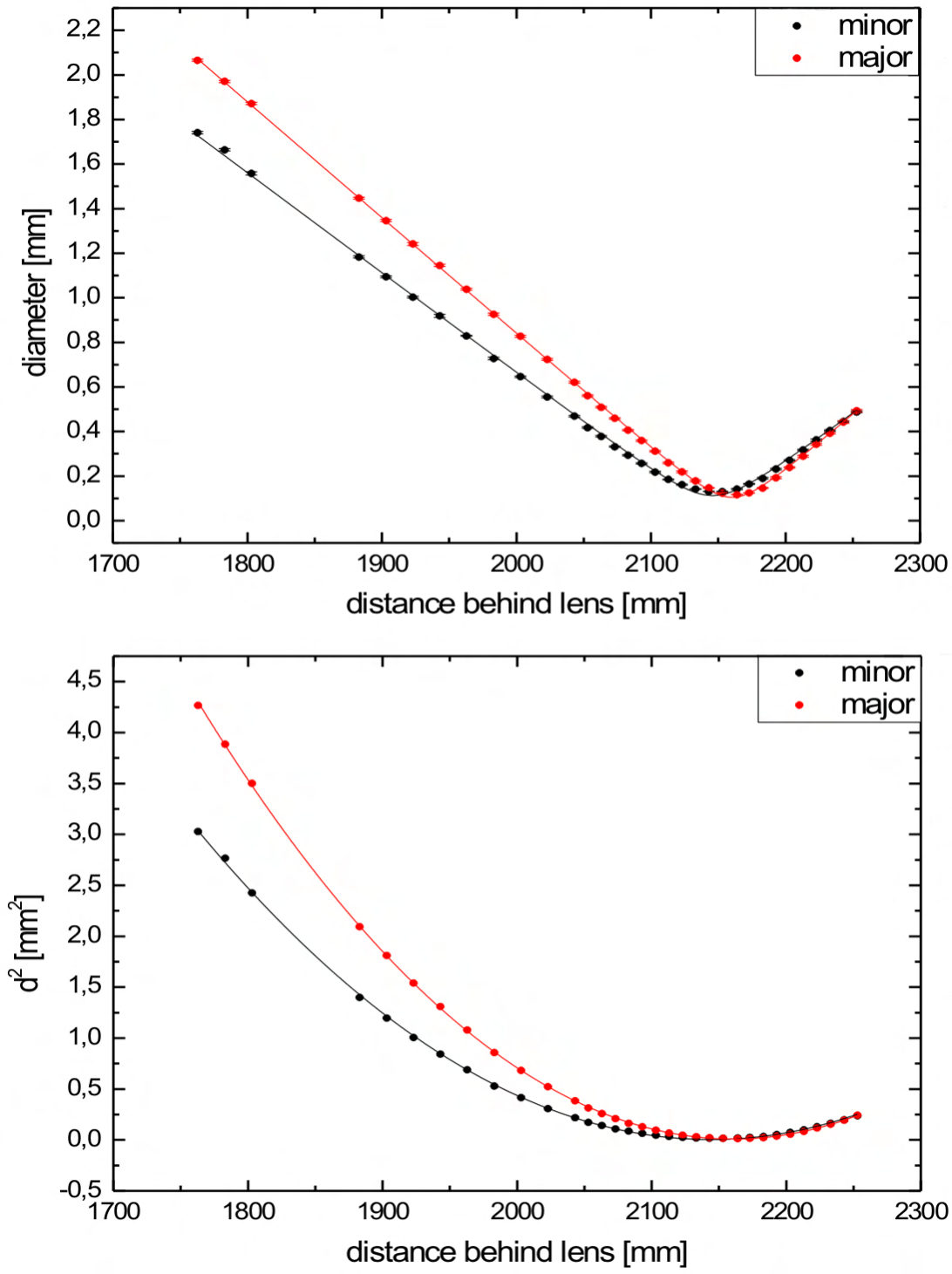

Figure 5.14: Measurement with a f = 2 m converging lens using a new BEX configuration and alignment. In the upper diagram, the beam diameter depending on the position behind the lens, including the hyperbola curve fit is shown. In the lower diagram, the square of the diameters including the parabola fit is shown.

The divergence of the current laser beam is below the requirement of 100 μrad, and therefore 99,7 % of the Gaussian beam are within the FOV of the telescope.

5.4 Summary of divergence measurements

It was shown in the previous chapter that laser beam divergence measurements with values of some 100 μrad are not easy to achieve. The divergence measurement with both methods requires accurate diameter measurement. Therefore it is important to know if the beam shape is radial symmetric, or not. For non radial symmetric beams it is necessary to make a difference between the major and the minor axis. Also the method of diameter determination should be well chosen. For real beams, the diameter calculation using the method of the first and the second moment would lead to minimal errors.

Using the knife-edge method it is important to realize that the Rayleigh length of the outcoming beam could be higher than 50 m for UV wavelengths, and a beam waist diameter larger than 6 mm. So the approximation of linear diameter propagation could only be done, if the diameter measurements are performed in a distance of at least two time the Rayleigh length. If not, the hyperbola fit has to be used for beam parameter determination.

Using a converging lens for beam transformation it is crucial to choose non aberrative optics. The focal length of the lens must be well known, because the accuracy of the measurement is mainly depending on the knowledge of the focal length. Furthermore, the focal length must be chosen in a way that the focus diameter is measurable with the used CMOS detector. It must be pointed out that at least 10 diameter measurements within one Rayleigh length, and 10 beyond are necessary to minimise the fit error. Additionally it is important to determine the beam waist diameter of the emanating beam by the radius of curvature. If the approximation is used that the waist diameter of

the original beam is nearly as large as the one at the lens, the error in the divergence calculation would not be negligible.

If above criteria are met, both measurement methods will be able to determine the divergence with an accuracy of 10 %, for divergence values in the order of 100 μrad. Due to the comfortable setup in laboratory, the non radial symmetric beam, and the easier diameter determination, the lens method would be preferred to the knife-edge method. Also the BEX alignment is easier to achieve with this method.

After optimisation of the laser alignment and magnification of the BEX, the divergence of the emanating beam was smaller than **100 μrad**. Therefore the beam is completely in the FOV of the receiver telescope, and an optimal radiometric performance of the A2D lidar system is possible.

Chapter 6

Summary and conclusion

The main objective of this thesis was to characterise the laser beam parameters and the frequency stability of the ALADIN airborne demonstrator A2D in the vibrational environment of an aircraft. It was shown that the cavity control technique, based on ramp and fire, allows seeded laser operation despite the vibration levels in the aircraft. This was not achieved with the earlier cavity control based on pulse build up time minimisation technique. The frequency jitter from pulse to pulse, measured during 2 flights in April 2007 was smaller than **0,6 MHz (IR)** which is below the requirement of 1,3 MHz. This frequency stability was reached for ramp fire and ramp delay fire settings, independent of vibration level and the respective flight attitude (travel flight, curve flight, descent flight). The timing jitter between actual pulse and expected pulse during the flights was smaller than **50 ns (rms)**. This value is a factor of 2 lower than the requirements. During the test flights, no dependence between cavity control settings, flight situation and timing jitter was realized. During the vibration test in laboratory it was shown that the ramp fire control method leads to a lower frequency jitter, and the ramp delay fire method to a lower timing jitter, which is expected.

The pulse energy requirement for the laser transmitter is 60 $\frac{mJ}{pulse}$, which is equivalent to a laser power of 3,0 W for 50 Hz pulse repetition rate. It was shown that the seedlaser

frequency was not in the gain spectrum of the low power oscillator. After changing the seedlaser frequency due to a higher laser crystal temperature, and after coarse alignment of the laser beam through the second and third harmonic crystals for a better conversion efficiency, a laser power between **3,4 W and 3,5 W (68-70** $\frac{mJ}{pulse}$**)** was achieved.

The beam divergence for the A2D laser transmitter has to be smaller than 100 μrad (6σ diameter) to be completely in the field of view of the telescope. To determine the actual divergence angle, comprehensive measurements were done in field and laboratory. These measurements yields values for M^2 of **1,8** and divergence angles at about **200** μ**rad**. After changing the lens combination of the beam expander to get a larger beam diameter magnification from 4 to 5, and after realigning the optical path the of IR beam to obtain a better M^2, the divergence angle was determined to be smaller than **100** μ**rad**, and a M^2 **value of 1,2** was achieved. A summary of the required laser parameters in comparison with the actual measured values in this thesis is show in table 6.1.

	Requirement	Characterized value	Comment
Laser energy per pulse	**> 60 mJ**	**70 mJ**	After spectral modifications and alignment
Frequency stability (pulse to pulse)	**< 1,3 MHz (rms, IR)**	**< 0,6 MHz (rms, IR)**	During flight operation, independent of cavity control settings
Timing jitter (between expected and actual pulse)	**< 100 ns**	**< 50 ns**	During flight operation, independent of cavity control settings
Divergence (6σ = 99,7%)	**100 µrad**	**< 100 µrad**	After change and realigning laser beam expander

Table 6.1: Comparison between requirements and characterized laser parameters in this thesis.

It is obvious from table 6.1, that all laser requirements are met. The future measurements with the A2D receiver and laser should verify that the radiometric performance of the A2D is within the expected values of the simulations. If the measured signal of the Rayleigh and Mie receiver is lower than the expected one, one reason can arise from pointing stability of the laser beam from short term (pulse to pulse) or long term effects. In this case it is necessary either to improve the pointing stability of the laser beam or to decrease the laser divergence further.

Appendix A

LaserCam-HR

High-Resolution Laser Beam Profiling System

		LaserCam-HR
Specifications	Matrix Size	1280 x 1024 pixels
	Pixel Size	6.7 x 6.7 µm
	Sensor Active Area	8.5 x 6.8 mm (2/3 inch format)
	Spectral Range	300 to 1,100 nm (400 to 1,100 with LDFP)
	Glassless Sensor	Low Distortion Faceplate is removable
	Low Distortion Faceplate (LDFP)	NG10 glass, nominal OD = 2.3
	Electrical Interface	USB 2.0
	Modes of Operation	Pulsed, CW
	Pulsed Mode Trigger Methods	Trigger In (TTL)
	Maximum Pulse Trigger In Rate	100 Hz (without averaging adjacent pulses)
	Maximum Frame Rate	15 FPS (live video, no calculations), 10 FPS (capture with calculations)
	CW Saturation @ 633 nm	40 mW/cm² (with LDFP), 16 µW/cm² (without LDFP)
	CW Saturation @ 1064 nm	800 mW/cm² (with LDFP), 320 µW/cm² (without LDFP)
	USB 2.0 Connector	5-pin standard USB cable included
	Trigger Connector	BNC connector, trigger cable included
BeamView-USB Analyzer PC Software	Measures	Centroid & peak locations, pointing stability beam width/diameter, divergence, gaussian fit analysis, elliptical analysis and uniformity analysis
	Beam Width Calculations	Multiple, including the ISO standard d4 Sigma
	Displays	2-D, 3-D and choice of 4 color styles
	Data Logging	For long-term laser stability analysis
	Data File Formats	Binary, ASCII, Bitmap, JPEG/JIF and many more
	Operating System Compatibility	Windows XP (service pack 1 or higher)
	Pass/Fail Analysis	Of all measurements for production automation
	Statistical Analysis	Of all measured laser parameters
	Background Noise Level Monitoring	Alerts user when background correction is invalid
	Password Protection	Limits unauthorized access to system configuration
	Automated Apertures	Display calculated beam dimensions
	User-Defined Apertures	Limit the scope of data for "Power-in-the-Bucket" calculations
	Cursors	Display centroid, comparative and fit data
	Crosshair	Defines bore-sighting central axis, centroid and/or peak locations
	Total Power or Energy Calibrated with an External Meter	Enables power density or fluence measurements
	Features	On-line help, hot function keys, graphical pan, zoom and many more
Part Number	BeamView-USB with LaserCam-HR	1068156

Figure A.1: Coherent - LaserCam Hr - Datasheet [Coherent LaserCam HR].

Technical Data		WS5 Precision	WS6 High Precision	WS7 Super Precision	WSU Ultimate Precision	
Measurement range [nm]:	Standard:	350 – 1120				
	UV:	248 – 1100			–	
	UV-II:	192 – 800			–	
	IR:	630 – 1750				
	IR-II	1000 – 2250			–	
					WSU-10	WSU-30
Relative accuracy:		5×10^{-6}	10^{-6}	10^{-7}	2×10^{-8}	5×10^{-8}
Absolute accuracy:	350 – 1100 nm [MHz]:	3000	600	60	10	30
	1100 – 2250 nm [MHz]:	2000	500	50	–	30
	192 – 350 nm [pm]:	3	0.6	0.2	0.2	
Quick coupling accuracy (with 400 µm fiber) [MHz]:		3000	600	200	100	
Measurement speed [Hz]:* (depending on PC hardware and settings)	Wavelength:	500		200		
	Interferometer picture:	100		50		
	Linewidth option:	20			15	
	Resolver option:	3	–	3	–	
Required input power [µW]: (1 s exposure)	Standard:	0.02 – 5		0.06 – 15		
	UV:	0.1 – 20		0.3 – 60	–	
	UV-II:	20 – 200		50 – 500	–	
	IR:	1 – 80	1 – 20	3 – 200	3 – 60	
	IR-II (10 ms exposure):	100 – 2000		250 – 5000	–	
Fizeau interferometers: [5]	FSR [GHz]:	100	15 (100)	4 (15)	2 (15)	
	Spectral resolution [GHz]:	20	20 3	3 0.8	3	0.4
Linewidth option: [4]	Max. bandwidth [GHz]:	60		20		
	Accuracy [MHz]: [1]	5 % (≥ 2000)[1]	5 % (≥ 500)[1]	5 % (≥ 200)[1]	5 % (≥100)[1]	
Resolver option: [4]	Range [THz]:	40	–	40[2] 0.003[3]	–	
	Max. bandwidth [GHz]:	30	–	30[2] 2[3]	–	
	Spectral resolution [GHz]:	5	–	5[2] 0.25[3]	–	
Grating option: [4]	Spectral resolution [nm]:	0.02		–	–	
Coupling fiber diameter [µm]:		400 or 50		400 or SM fiber set	SM fiber set	
Calibration:		With integrated calibration source		With supplied external calibration source	Using stabilized HeNe laser or any other well-known laser source	
Warm-up time:		No warm-up time under constant ambient conditions (except IR: >30 minutes warm-up time required) Otherwise until thermal equilibrium is reached				
Weight [kg]:		2.8		5.6	6.3	
Dimensions L × W × H [mm]:		360 × 120 × 120		360 × 210 × 120		
Interface:		High-speed USB 2.0 connection				
Power supply:		Power consumption < 2.3 W, supply directly via USB cable IR and PID LaserControl option: external power supply included				

1) Max. accuracy for narrow linewidth lasers in MHz
2) Resolution for broad linewidth laser sources
3) Resolution for narrow linewidth
4) For standard range
5) Values for wide-/fine-mode
*) On request

Note: HighFinesse follows a policy of **continuous product improvement.**
Specifications are subject to change without notice.

HighFinesse
Laser and Electronic Systems

HighFinesse GmbH
Auf der Morgenstelle 14 D
72076 Tübingen/Germany

T +49 (0) 7071-96 85 15
F +49 (0) 7071-96 85 17
E info@highfinesse.com

Additional information and distributors:
www.highfinesse.com

Figure A.2: High Finesse - Wavelengthmeter WSU-10 - Datasheet [High Finesse WS Ultimate].

Specifications

Applicable fiber		SM (9.5/125µm), GI (50/125µm)
Measurement wavelength range		600 to 1700nm
Span		0.1nm to full range and zero span
Wavelength accuracy[1,2,3,4]		±10pm (1520 to 1580nm, after calibration with built-in source) ±20pm (1450 to 1520nm, after calibration with built-in source) ±20pm (1580 to 1620nm, after calibration with built-in source) ±50pm (Full range, after calibration with built-in source)
Wavelength linearity[1,2,3,4]		±10pm (1520 to 1580nm, after calibration with built-in source) ±20pm (1450 to 1520nm, after calibration with built-in source) ±20pm (1580 to 1620nm, after calibration with built-in source)
Wavelength repeatability[1,2,3,4]		±2pm (1min. or less, 1450 to 1620nm)
Number of samplings		101 to 50001
Resolution bandwidth		0.01, 0.02, 0.05, 0.1, 0.2, 0.5 and 1nm
Resolution accuracy[1,3,4,5]		±2% (RES.: 0.1nm or wider, 1450 to 1620nm) ±2.5% (RES.: 0.05nm, 1450 to 1620nm) ±6% (RES.: 0.02nm, 1450 to 1620nm)
Level sensitivity setting[8]		NORM_HOLD, NORM_AUTO, MID, HIGH 1, HIGH 2 and HIGH 3
Level sensitivity[1,3,5,7]		-90dBm (1250 to 1620nm, RES.: 0.05nm or wider, SENS.: HIGH 3) -80dBm (1000 to 1250nm, RES.: 0.05nm or wider, SENS.: HIGH 3) -60dBm (800 to 1000nm, 1620 to 1680nm, RES.: 0.05nm or wider, SENS.: HIGH 3)
Level accuracy[1,5],7,8		±0.3dB (1550/1600nm, 0/-20dBm, RES.: 0.02nm or wider) ±0.3dB (1310nm, 0/-20dBm, RES.: 0.05nm or wider)
Level linearity[1,3,5,7]		±0.05dB (-50 to +10dBm, RES.: 0.02nm or wider, SENS.: HIGH 1 to 3)
Level flatness[1,5,7],8		±0.1dB (1520 to 1620nm, -20dBm, RES.: 0.02nm or wider)
Level stability[1,5],7,8		±0.01dB at 1min., ±0.02dB at 15min. (1550/1600nm, -20dBm, RES.: 0.05nm or wider)
Maximum input power[1]		+23dBm (Per channel, Full span, Attenuation on)
Safe max. input power[1]		+27dBm (Total safe power, Attenuation on)
Close-in dynamic range[1,3],7,9		40dB (±50pm from peak at 1523nm, RES.: 0.01nm) 60dB (±100pm from peak at 1523nm, RES.: 0.01nm) 70dB (±200pm from peak at 1523nm, RES.: 0.01nm) 60dB (±200pm from peak at 1523nm, RES.: 0.1nm)
Polarization dependency[1],5,7		±0.05dB (1520 to 1620nm, RES.: 0.02nm or wider) ±0.07dB (1450 to 1520nm, RES.: 0.02nm or wider) ±0.07dB (typ.) (1310nm, RES.: 0.05nm or wider)
Sweep time		0.5 sec. (any 100nm, SMPL.: 1001, SENS.: NORM_HOLD)[10] 1 sec. (any 100nm, SMPL.: 1001, SENS.: MID)[10] 3 sec. (any 100nm, SMPL.: 1001, SENS.: HIGH 1)[10] 15 sec. (any 100nm, SMPL.: 1001, SENS.: HIGH 3)[11] 120 sec. (any 100nm, SMPL.: 1001, SENS.: HIGH 3 with chop mode on)[11]
Function	Automatic measurement	Program function (64 programs, 200 steps)
	Setting of measuring conditions	Span setting: 0 to 1100nm, Number of averaging setting: 1 to 999 times, Automatic measuring condition setting function, Sweep between line markers function, 0nm sweep function, External trigger measurement function, Air/Vacuum wavelength measurement function
Function	Display	Level scale setting: 0.1 to 10dB/div., Vertical division number setting: 8, 10 or 12, Ref. level position setting function, Linear scale display, Simultaneous display of 7 independent traces, Data table display, Label display, Split display, Normalized display, Curve-fit display,
Function	Display	Power density display, % display, dB/nm display, dB/km display, Template display, Horizontal scale zoom in/out display, Frequency display of horizontal axis scale
	Trace	7 independent traces, Max./Min. hold, Calculate between traces, Roll average, Normalize, Curve-fit
	Marker/Search	Delta marker (Max. 1024), Line marker, Peak search, Next peak search, Bottom search, Next bottom search, Auto search, Peak/Bottom search between line markers, Search in the zooming area
	Analysis	WDM analysis, EDFA analysis, Optical filter analysis, WDM filter analysis, Spectral width, Notch width, SMSR analysis, PMD analysis, LED/FP-LD/DFB-LD analysis, Power analysis, Go/NoGo judgment, Auto analysis, Analysis between line markers, Analysis in the area
	Ethernet	TCP/IP Protocol, FTP function
	External printer[12]	ESC/P
	Others[13]	Self wavelength calibration with built-in reference light source Optical alignment with built-in reference light source
Memory	Build-in FDD (3.5-inch 2HD)	MS/DOS format
	Internal memory	32 traces, 20 programs
	File format	Binary/CSV(Text), BMP/TIFF
Printer		Built-in high-speed thermal printer
Interface	Remote control	AQ6317 Series compliant commands (IEEE488.1), IEEE488.2 full support
	Others	GPIB x 2, RS232C, Printer port, External SVGA, PS/2 x 2, LAN
Display		10.4-inch color LCD (Resolution: 800 x 600 dots)
Optical connector[14]		AQ9447 (*) connector adapter: optional
Power requirement		100 to 240 (±10%) V, 50/60Hz, approx. 400VA
Environmental conditions		Operating temperature: +5 to +40°C Storage temperature : -10 to +50°C Humidity: 80%RH or less (no condensation)
Dimensions and mass[15]		Approx. 425 (W) x 222 (H) x 500 (D) mm, 33kg
Accessories		Power cord: 1, printer paper: 1, instruction manual: 1

Notes:

1) With 9.5/125µm SMF, after 1 hour warm-up, after optical alignment
2) At 15 to 30 °C
3) At chop mode off
4) Horizontal scale: wavelength display mode
5) At 23 ± 3 °C
6) Internal chop mode available at HIGH1 to 3 sensitivity settings
7) With applied input fiber Type B1.1 9.5/125µm SMF defined on IEC60793-2 (Mode field diameter: 9.5µm, NA: 0.104 to 0.107, PC polished), attenuation off, vertical scale: absolute power display mode
8) Sensitivity setting is MID, HIGH1 to 3 and chop mode off
9) Sensitivity setting is HIGH3 and chop mode on
10) For wavelength resolution ≦0.2nm
11) For wavelength resolution ≦0.5nm
12) Please ask local agent for printer type.
13) AQ9441 universal adapter (optional) is required for the output port of the reference light source (specify FC, SC or ST for connector type).
14) *: Connector type. Specify FC, SC or ST connector.
15) Except protector

Figure A.3: Yokogawa - Optical spectrum analyzer AQ 6319 - Datasheet [Yokogawa AQ 6319].

Plankonvex-Linsen aus fused silica

gültig ab August 2006

LASER COMPONENTS

Diese Liste umfasst alle Vorzugstypen, die bei uns ab Lager erhältlich sind. Alle Linsen sind λ/10-passgenau und laserfeinstpoliert für höchste Laserleistungsdichten.

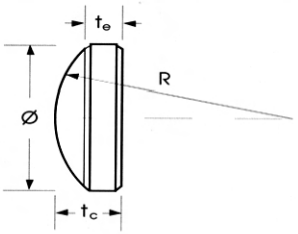

Spezifikationen

Material	fused silica Q1 oder equivalent
Formtreue	λ / 10 bei 632.8 nm beidseitig
Oberflächenqualität	5 / 4 x 0.025 beidseitig
Durchmessertoleranz	+ 0.00 mm, -0.25 mm
Dickentoleranz	± 0.25 mm
Schutzfacette	0.2 mm - 0.4 mm bei 45° typ
Freie Apertur	85% mittig vom Durchmesser
Konzentrizität	≤ 0.2 mm, 4/3'
Fokuslängentoleranz	± 1%

Typenbezeichnung: PLCX (Produkt Code) - 25.4 (Durchmesser in mm) / 25.8 (Konvex-Radius in mm) UV (Material Code)

Nominal f (mm)	Durchm. Ø (mm)	248 nm f (mm)	308 nm f (mm)	355 nm f (mm)	1064 nm f (mm)	Radius R (mm)	tc (mm)	te (mm)	Typenbezeichnung	Preis EURO
25.0	25.4	25.4	26.6	27.1	28.7	12.9	12.7	2.0	PLCX-25.4/12.9UV	180 €
30.0	12.7	30.5	31.9	32.6	34.5	15.5	2.4	1.0	PLCX-12.7/15.5UV	130 €
35.0	25.4	35.4	37.1	37.8	40.0	18.0	7.2	2.0	PLCX-25.4/18.0UV	150 €
40.0	25.4	40.5	42.4	43.3	45.8	20.6	5.3	0.9	PLCX-25.4/20.6UV	150 €
50.0	25.4	50.7	53.1	54.2	57.4	25.8	5.3	2.0	PLCX-25.4/25.8UV	130 €
60.0	25.4	60.8	63.6	64.9	68.7	30.9	4.2	1.5	PLCX-25.4/30.9UV	130 €
65.0	12.7	66.3	69.4	70.8	75.0	33.7	3.0	2.4	PLCX-12.7/33.7UV	110 €
65.0	25.4	66.3	69.4	70.8	75.0	33.7	5.0	2.5	PLCX-25.4/33.7UV	120 €
75.0	12.7	75.9	79.5	81.1	85.8	38.6	3.0	2.5	PLCX-12.7/38.6UV	110 €
75.0	25.4	75.9	79.5	81.1	85.8	38.6	3.6	1.5	PLCX-25.4/38.6UV	120 €
100.0	25.4	101.3	106.0	108.2	114.5	51.5	4.0	2.4	PLCX-25.4/51.5UV	110 €
125.0	25.4	126.6	132.6	135.3	143.2	64.4	2.6	1.3	PLCX-25.4/64.4UV	100 €
150.0	25.4	152.0	159.2	162.4	171.9	77.3	4.0	2.9	PLCX-25.4/77.3UV	100 €
200.0	12.7	202.5	212.1	216.4	229.1	103.0	2.2	2.0	PLCX-12.7/103.0UV	90 €
200.0	25.4	202.5	212.1	216.4	229.1	103.0	4.0	3.2	PLCX-25.4/103.0UV	100 €
250.0	25.4	253.3	265.2	270.5	286.5	128.8	4.0	3.4	PLCX-25.4/128.8UV	100 €
300.0	25.4	303.8	318.1	324.5	343.6	154.5	4.0	3.5	PLCX-25.4/154.5UV	100 €
350.0	25.4	354.5	371.3	378.7	401.0	180.3	4.0	3.6	PLCX-25.4/180.3UV	100 €
400.0	25.4	405.1	424.2	432.7	458.2	206.0	2.4	2.0	PLCX-25.4/206.0UV	100 €
500.0	25.4	506.3	530.2	540.9	572.7	257.5	4.0	3.7	PLCX-25.4/257.5UV	100 €
600.0	25.4	607.8	636.5	649.3	687.5	309.1	4.0	3.7	PLCX-25.4/309.1UV	100 €
700.0	25.4	709.1	742.5	757.4	802.0	360.6	2.2	2.0	PLCX-25.4/360.6UV	100 €
800.0	25.4	810.3	848.6	865.6	916.5	412.1	4.0	3.8	PLCX-25.4/412.1UV	100 €
1000.0	25.4	1012.9	1060.7	1082.0	1145.6	515.1	4.0	3.8	PLCX-25.4/515.1UV	100 €
1500.0	25.4	1519.2	1590.9	1622.9	1718.3	772.6	2.2	2.1	PLCX-25.4/772.6UV	100 €
2000.0	25.4	2025.8	2121.3	2164.0	2291.2	1030.2	4.0	3.9	PLCX-25.4/1030.2UV	100 €

Für weitere Nicht-Vorzugs-Typen beachten Sie bitte unseren Optikkatalog.

Stand: August 2006, ersetzt Ausgabe vom Februar 2006 / Version 6 / HW / Plankonvex-fused-silica.xls/de

Bei einem Bestellwert unter 50,-- € wird ein Mindermengenzuschlag von 5,-- € erhoben.
Preisänderungen vorbehalten
Preisstellung: ab Werk Olching, unverpackt, unversichert, zuzüglich derzeit gültiger Mehrwertsteuer
Zahlungsbedingungen: 30 Tage netto

Wir akzeptieren / We accept EUROCARD MasterCard VISA TÜV ISO 9001

www.lasercomponents.com

LASER COMPONENTS GmbH, Werner-von-Siemens-Str. 15, 82140 Olching, Germany, Tel.: +49 8142 2864-0, info@lasercomponents.com

Figure A.4: Laser Components - Fused Silica Singlet Lenses - Datasheet [Laser Components].

List of Figures

List of Tables

Acronyms

A2D	ALADIN airborne demonstrator
ACCD	Accumulation CCD
ADM	Atmospheric Dynamics Mission
ALADIN	Atmospheric laser Doppler instrument
AOM	Acousto-optic modulator
BEX	Beam expander
BPP	Beam parameter product
BTM	Beam turning mirrors
CCD	Charge-coupled device
CMOS	Complementary metal oxide semiconductor
CW	Continous wave
DLR	Deutsches Zentrum für Luft- und Raumfahrt
DWL	Doppler wind lidar
EADS	European aeronautic defence and space company
ESA	European space agency
FC	Fibre connector
FI	Faraday isolator
FSR	Free spectral range
FWHF	Full width half maximum
HLOS	Horizontal line of sight
HR	High reflective mirror
ILT	Institut für Lasertechnik

IR	Infrared
ISO	International organisation for standardisation
LASER	Light amplification by stimulated emission of radiation
LBO	Lithium triborate
LIDAR	Light detection and ranging
LOS	Line of sight
LPO	Low power oscillator
Nd:YAG	Neodymium doped Yttrium Aluminium Garnet
NPRO	Non planar ring oscillator
OBA	Optical bench assembly
OSA	Optical spectrum analyzer
PLL	Phased locked loop
Pol.	Polariser
PSD	Power spectral density
PZT	Piezoelectric translator
QBUT	Q-switch build up time
RDF	Ramp delay fire
RF	Ramp and fire
RLH	Reference laser head
RMS	Root mean square
SHG	Second harmonic generation
TEM	Transverse electromagnetic mode
THG	Third harmonic generation
UV	Ultraviolet
VRM	Variable reflective mirror
WLM	Wavelength meter

Bibliography

[Abramowitz and Stegun 1972] Abramowitz M. and Stegun I. A. (1972), *Handbook of mathematical functions with formulas, graphs, and mathematical tables*. United States Department of Commerce, National Bureau of Standards, Applied Mathematics Series 55, No. 6, 310 p.

[Albrecht et al. 2003] Albrecht H.-E., Borys M., Damaschke N., Tropea C. (2003), *Laser Doppler and phase Doppler measurement techniques*. Springer, Berlin, 750 p., ISBN 3-540-67838-7.

[Baker et al. 1995] Baker W. E., Emmitt G. D., Robertson F., Atlas R. M., Molinari J. E., Bowdle D. A., Paegle J., Hardesty R. M., Menzies R. T., Krishnamurti T. N., Brown R. A., Post M. J., Anderson J. R., Lorenc A. C., McElroy J. (1995), Lidar-measured winds from space: A key component for weather and climate prediction. *Bull. Am. Meteorol. Soc.*, Vol. 76, No. 6, p. 869 - 888.

[Barnes 1993] Barnes N. P., Barnes J. C. (1993), Injection seeding. I. Theory. *IEEE Journal of Quantum Electronics*, Vol. 29, No. 10, p. 2670 - 2683, ISSN: 0018-9197.

[Bouwkamp 1954] Bouwkamp J. (1954), Diffraction Theory. *Reports on Progress in Physics XVIII*, p. 35 - 100.

[Chester et al. 1988] Chester A. N., Letokhov V. S., Martellucci S. (1988), *Laser science and technology*. Springer, New York, 455 p., ISBN 0-036-430339.

[Coherent LaserCam HR] Coherent LaserCam HR, user manual, (available from http://www.coherent.de/produkte/laserzubehoer/strahldiagnose/lasercam-hr-usb-kamera/).

[Durand 2006] Durand Y., Chinal E., Endemann M., Meynart R., Reitebuch O., Treichel R. (2006), ALADIN Airborne Demonstrator: a Doppler wind lidar to prepare ESA's ADM-Aeolus Explorer Mission. *Proc. SPIE*, Vol. 6269, No. 1D, 9 p.

[Eichler and Eichler 2003] Eichler H. J., Eichler J. (2003), *Laser: Bauformen, Strahlführung, Anwendung*, Springer, Berlin, 476 p., ISBN 3540301496.

[Eichler et al. 2004] Eichler J., Dünkel L., Eppich B. (2004), Die Strahlqualität von Lasern - Wie bestimmt man Beugungsmaßzahl und Strahldurchmesser in der Praxis? *Laser Technik Journal*, Oktober 2004, No. 2, p. 62 - 65.

[ESA 1998] ESA (1998), Earth Explorers: The science and research elements of ESA's Living Planet Programme. Report, SP-1227, 106 p., ISBN 92-9092-504-3.

[ESA 1999] ESA (1999), Atmospheric Dynamics Mission - The four candidate Earth Explorer Core missions. Reports for Mission selection, SP-1233, 157 p., ISBN 92-9092-528-0.

[ESA 2005] ESA (2005), ESA's wind mission (2005). ADM-Aeolus Brochure, BR-236, 17 p. (available from http://www.esa.int/esapup/br/br236/br236.pdf).

[Fry et al. 1990] Fry E. S., Hu Q., Li X. (1990), Single frequency operation of an injection-seeded Nd:YAG laser in high noise and vibration environments. *Appl. Opt.*, Vol. 30, No. 9, p. 1015 - 1017.

[High Finesse WS Ultimate] High Finesse WSU - 10 data sheet, (available from http://highfinesse.de/wsu.php), 2 p.

[Hitz et al. 2001] Hitz B., Ewing J. J., Hecht J. (2001), Introduction to laser technology, 3rd edition. *IEEE press, New York*, 304 p., ISBN 0-7803-5373-0.

[Hovis et al. 2004] Hovis F. E., Rhoades M., Burnham R. L., Force J. D., Schum T. (2004), Single-frequency lasers for remote sensing. *Proc. SPIE*, Vol. 5332, No. 6, p. 263 - 270.

[ILT 2006] Fraunhofer Institut Lasertechnik, Becks L. (2006), Betriebsanleitung für Platine EADS A2D-Lidar, 10 p.

[Innolight 2004] Innolight, Hunnekuhl M. (2004), Aladin Airborne Demonstrator reference laser head (RLH) - Detailed design description. Report, INO-ADM-DDD-001, 26 p.

[ISMB 2007] ISMB GmbH Forster R. (2007), ALADIN Laser in flight vibration measurement. Testreport, 46 p., ISMB-2-072-7220.

[ISO 11146] Internationl Organization for Standardization ISO 11146 (1999), Lasers and laser-related equipment - Test methods for laser beam parameters - Beam widths, divergence angle and beam propagation factor. 26 p. (available from www.iso.org).

[Kane and Byer 1985] Kane T. J., Byer L. R. (1985), Monolithic, unidirectional single-mode Nd:YAG ring laser. *Opt. Letters*, Vol. 10, No. 2, p. 65 - 67.

[Kneubühl and Sigrist 2005] Kneubühl F. K., Sigrist M. W., 6. Auflage (2005), *Laser*. Teubner Studienbücher, Stuttgard, 413 p., ISBN 3-835-10032-7.

[Koechner 1988] Koechner W. (1988), *Solid-State Laser Engineering*. Springer, Berlin, 746 p., ISBN 3-540-18747-2.

[Kogelnik and Li 1966] Kogelnik H., Li T. (1966), Laser beams and resonators. *Appl. Opt.*, Vol. 5, No. 10, p. 1550 - 1567.

[Laser Components] Laser Components, Converging lens datasheet, (available from http://www.lasercomponents.com/de/599.html).

[McClung and Hellwarth 1962] McClung F. J., Hellwarth J. (1962), Giant optical pulsations from Ruby. *Journal of Appl. Physics*, Vol. 33, No. 3, p. 828 - 829.

[Measures 1984] Measures R. M. (1984), *Laser remote sensing: Fundamentals and applications*. Wiley, New York, 510 p., ISBN 0-471-08193-0.

[Nicklaus et al. 2007] Nicklaus K., Morasch V., Hoefer M., Luttmann J., Vierkötter M., Ostermeyer M., Höffner J., Lemmerz C., Hoffmann D. (2007), Frequency stabilisation of Q-switched Nd:YAG oscillators for airborne and spaceborne LIDAR systems. *Proc. SPIE*, Vol. 6451, 12 p.

[Paffrath 2006] Paffrath U. (2006), Performance assessment of the Aeolus Doppler wind lidar prototype. Dissertation Technische Universität München, Juni 2006, DLR Forschungsbericht 2006-12, ISSN 1434-8454, 137 p.

[Reitebuch and Fix 2006] Reitebuch O., Fix A. (2006), Lidar für Meteorologen, University of Innsbruck, SS 2006, lecture script.

[Reitebuch et al. 2003] Reitebuch O., Chinal E., Dabas A., Durand Y., Endemann M., Flamant P. H., Meynart R., Morancais D., Paffrath U., Poberaj G. (2003), Ground and airborne Doppler lidar campaigns for ADM, *Proc. 6th Int. Symp. Tropospheric Profiling*, Leipzig, p. 432 - 434.

[Reitebuch et al. 2004] Reitebuch O., Chinal E., Durand Y., Endemann M., Meynart R., Morancais D., Paffrath U. (2004), Development of an airborne demonstrator for ADM-Aeolus and campaign activities, *Proc. Int. Laser Radar Conf.*, Matera, p. 1007 - 1010.

[Roundy 1999] Roundy C. (1999), Beam-Profile Analysis: Propagation factor quantifies laser beam performance. *Laser Focus World*, Vol. 35, No. 12, 7 p.

[Roundy 2000] Roundy C. (2000), Current technology of laser beam profile measurements in *Laser beam shaping - Theory and techniques*, Dickey F. M. ed., p. 349 - 369, ISBN 08247039987.

[Sasnett 1989] Sasnett M.W. (1989), Propagation of multimode laser beams in *The M^2 factor - The physics and technology of laser resonators*. D. R. Hall and P. E. Jackson ed., p. 132 - 142, ISBN 0-85274-117-0.

[Schmitt and Rahn 1986] Schmitt R. L., Rahn L. A. (1986), Diode-laser-pumped Nd:YAG laser injection seeding system. *Appl. optics*, Vol. 25, No. 5, p. 629 - 633.

[Schröder et al. 2007] Schröder T., Lemmerz C., Reitebuch O., Wirth M., Wührer C., Treichel R. (2007), Frequency jitter and spectral width of an injection-seeded Q-switched Nd:YAG laser for a Doppler wind lidar. *Appl. Physics B - Lasers and Optics*, Vol. 87, No. 3, p. 437 - 444.

[Siegman 1986] Siegman A. E. (1986), *Lasers*. University Science Books, Mill Valley, California. 1283 p., ISBN 0-935702-11-5.

[Stoffelen et al. 2005] Stoffelen A., Pailleux J., Källen E., Vaughan J. M., Isaksen L., Flamant P., Wergen W., Andersson E., Schyberg H., Culoma A., Meynart R., Endemann M., Ingmann P. (2005), The atmospheric Dynamics Mission for global wind field measurement, *Bulletin of the American Meteorological Society*, Vol. 86, No. 1, p. 73 - 87.

[Walther et al. 2001] Walther T., Larser M. P., Fry E. S. (2001), Generation of Fourier-transform-limited 35 ns pulses with ramp-hold-fire seeding technique in a Ti:sapphire laser. *Appl. Opt.*, Vol. 40, No. 18, p. 3046 - 3050.

[Weitkamp 2005] Weitkamp C. (2005), *Lidar - range resolved optical remote sensing of the atmosphere*. Springer, New York, 455 p., ISBN 0-387-40075-3.

[Wright et al. 1992] Wright D., Greve P., Fleischer J., Austin L. (1992), Laser beam width, divergence and beam propagations factor - an international standardization approach. *Optical and Quantum Electronics*, Vol. 24., p. 993 - 1000.

[Yokogawa AQ 6319] Yokogawa AQ 6319 user manual, (available from http://www.yokogawa.com/tm/optfiber/aq6319/tm-aq6319-01.htm).

Acknowledgements

I would like to thank Professor Heilmann being my tutor and advisor during this research work. I am grateful to Professor Schumann, director of the "Institut für Physik der Atmosphere (DLR)", and to Dr. G. Ehret, head of the lidar group, for their encouragement, giving me the opportunity to carry out this research work.
I would like to express my deepest gratitude to my mentor Dr. Oliver Reitebuch for supporting my work during the study of this thesis, for giving me very helpful suggestions, and for giving me the feeling to be a member of the A2D team since the first day a started my research work.
A very special thanks goes to Christian Lemmerz who gave me the possibility to have a great deal of discussions for all intents and purposes. I would like to thank him for his tireless help explaining coherences in laser techniques and optics and for being the editor of this thesis.
I wish to thank Ulrike Paffrath, Engelbert Nagel, and Stephan Kox for being a very cooperative, uncomplicated, and helpful team for two months ground campaign work in Lindenberg (Berlin) and all the other time. I also want to thank the rest of the lidar team at DLR for the friendly support and the pre-eminently teamwork.
Special thanks go to my parents Dagmar and Klaus for giving me their love and their support in all respects and to my girlfriend Michaela who gave me motivation for this thesis, due to her love and her understanding of mental and physical absence for my part.